

İSTANBUL TECHNICAL UNIVERSITY ★ INSTITUTE OF SCIENCE AND TECHNOLOGY

**INVESTIGATION OF SURFACE PROPERTIES OF
A MICRO ARC OXIDIZED 7075 ALUMINIUM ALLOY**

**M.Sc. Thesis by
Samet Serkan BOZKUŞ**

Department : Metallurgical and Materials Eng.

Programme : Materials Engineering

JULY 2010

**INVESTIGATION OF SURFACE PROPERTIES OF
A MICRO ARC OXIDIZED 7075 ALUMINIUM ALLOY**

**M.Sc. Thesis by
Samet Serkan BOZKUŞ
(506071432)**

**Date of submission : 07 May 2010
Date of defence examination: 11 June 2010**

**Supervisor (Chairman) : Assoc. Prof. Dr. Murat BAYDOĞAN
(ITU)
Members of the Examining Committee : Prof. Dr. E. Sabri KAYALI (ITU)
Prof. Dr. Mehmet KOZ (MU)**

JULY 2010

İSTANBUL TEKNİK ÜNİVERSİTESİ ★ FEN BİLİMLERİ ENSTİTÜSÜ

**MİKRO ARK OKSİDASYON İŞLEMİ
UYGULANAN 7075 KALİTE ALUMİNYUM ALAŞIMININ
YÜZEY ÖZELLİKLERİNİN İNCELENMESİ**

**YÜKSEK LİSANS TEZİ
Samet Serkan BOZKUŞ
(506071432)**

Tezin Enstitüye Verildiği Tarih : 07 Mayıs 2010

Tezin Savunulduğu Tarih : 11 Haziran 2010

**Tez Danışmanı : Doç. Dr. Murat BAYDOĞAN (İTÜ)
Diğer Jüri Üyeleri : Prof. Dr. E. Sabri KAYALI (İTÜ)
Prof. Doç. Dr. Mehmet KOZ (MÜ)**

TEMMUZ 2010

FOREWORD

I wish to thank to my supervisor Assoc. Prof. Dr. Murat BAYDOĞAN for his invaluable guidance, suggestions and support during the course of my thesis and for being my mentor throughout my graduate studies. I would also thank to Prof. Dr. Hüseyin ÇİMENÖĞLU and Prof. Dr. Eyüp Sabri KAYALI for their precious guidance and elaborate critics on my study. I am indebted to Res. Assist. Mert GÜNYÜZ, Res. Assist. Onur MEYDANOĞLU, Res. Assist. Özgür ÇELİK for their valuable friendship and support.

I thank to TUBITAK (The Scientific and Technological Research Council of Turkey) for the scholarship, with which they supported me financially during my studies

I owe a special and a great deal of thanks to Zekiye Reyhan ARISOY who has encouraged me at all times.

Those I may have inadvertently missed have my sincere apologies.

And last but not least, thanks to my family, for backing me up and for their patience under any circumstances for all my life.

July 2010

Samet Serkan BOZKUŞ

Materials and Metallurgy

Engineer

ACKNOWLEDGEMENT

This study is a part of TUBITAK research project with the project number-107M038

TABLE OF CONTENTS

	<u>Page</u>
TABLE OF CONTENTS	vii
ABBREVIATIONS	ix
LIST OF TABLES	xi
LIST OF FIGURES	xiii
SUMMARY	ixx
ÖZET	xx1
1. INTRODUCTION	1
2. ALUMINUM AND ITS ALLOYS	3
2.1 Definitions for Aluminum and Aluminum Alloys	4
2.1.1 Commercially pure aluminum.....	4
2.1.2 Aluminum alloy.....	4
2.1.3 Strain-hardenable aluminum alloy	4
2.1.4 Heat treatable aluminum alloy	4
2.1.5 Wrought aluminum alloy	5
2.1.6 Cast aluminum alloy	5
2.2 Characteristics of Wrought Aluminum Alloys.....	5
2.2.1 Corrosion resistance	5
2.2.2 Thermal conductivity	7
2.2.3 Electrical conductivity.....	7
2.2.4 Strength/weight ratio	7
2.2.5 Fracture toughness and energy absorption capacity.....	7
2.2.6 Cryogenic toughness	7
2.2.7 Workability.....	8
2.2.8 Ease of joining.....	8
2.2.9 Recyclability.....	8
2.3 Aluminum Alloy and Temper Designation Systems.....	8
2.3.1 Aluminum alloy designation system.....	9
2.3.2 Aluminum alloy basic temper designation system.....	10
2.3.3 Subdivisions of the basic T temper	11
2.4 7xxx, Aluminum-Zinc Alloys	13
3. THE MICRO ARC OXIDATION PROCESS	15
3.1 History of Micro Arc Oxidation	15
3.2 Equipment.....	16
3.3 Mechanism of the Process	17
3.4 Application of the MAO process.....	20
3.5 Advantages and Disadvantages of the Process.....	21
3.6 Power Supplies	23
3.7 Electrolytes	25
4. MICRO ARC OXIDATION-OF ALUMINUM	29
4.1 Structural and Morphological Properties of the MAO Coatings	30

4.2 Wear Behavior.....	44
4.3 Corrosion Resistance Studies	46
4.4 Fatigue Properties of the MAO Coatings	49
4.5 Thermal Properties of the MAO Coatings	52
4.6 Other Studies	53
5. EXPERIMENTAL STUDIES.....	59
5.1 Sample Preparation	59
5.2 The MAO Process	59
5.3 Structural and Morphological Characterization	63
5.4 Hardness Tests.....	64
5.5 Wear Tests.....	64
5.4 Corrosion Tests	65
6. RESULTS AND DISCUSSION	66
6.1 The MAO Condition Parameters.....	66
6.1 The Effect of Pulse Durations	78
7. CONCLUSIONS	89
REFERENCES	91
APPENDICES	96
CURRICULUM VITAE.....	129

ABBREVIATIONS

AC	: Alternating Current
AlBeMet	: Beryllium and Aluminum Composite Material
DC	: Direct Current
GM	: General Motors
MAO	: Micro Arc Oxidation
MMC	: Metal Matrix Composite
PEC/N	: Plasma Electrolytic Carbonitriding
PED	: Plasma Electrolytic Deposition
PEO	: Plasma electrolytic Oxidation
PES	: Plasma Electrolytic Saturation
PVD	: Plasma Vapour Deposition
T6	: Temper designation of solution treated, then artificially aged aluminum alloy
USSR	: Union of Soviet Socialist Republics
UK	: United Kingdom

LIST OF TABLES

	<u>Page</u>
Table 2.1: Physical properties of aluminum	3
Table 2.2: Aluminum has good resistance toward these chemicals.....	6
Table 2.3: Aluminum cannot resist action of the following chemicals.....	6
Table 2.4: Main alloying elements in the wrought alloy designation system.....	10
Table 3.1: Applications and the characteristic properties in MAO techniques.....	22
Table 4.1: The MAO processing parameters	30
Table 4.2: Phase density data and estimated density of MAO coating	39
Table 4.3: Experimental data for measured skeletal densities of MAO coatings	40
Table 4.4: Results of the potentiodynamic corrosion tests	49
Table 5.1: Nominal chemical composition of 7075 aluminum alloy.....	59
Table 5.2: Processing conditions for the samples oxidized under voltage controlled mode	61
Table 5.3: Processing conditions for the samples oxidized under current controlled mode.....	62
Table 5.4: Processing conditions for the samples oxidized for different pulse durations.....	62
Table 6.1: Micro arc oxidation parameters selected to achieve maximum coating thickness.....	74

LIST OF FIGURES

	<u>Page</u>
Figure 3.1 : Typical arrangement of the equipment used for PED treatment. : (1) window, (2) mixer, (3) connecting wires, (4) exhaust/ventilation system, (5) grounded case, (6) power supply unit, (7) work piece, (8) cooling system, (9) bath, (10) insulating plate.....	17
Figure 3.2 : Electrode process in electrolysis of aqueous solutions.....	18
Figure 3.3 : Two kind of current-voltage diagram for the process of plasma electrolysis discharge (a) in the near-electrode area and (b) in the dielectric film on the electrode surface.....	19
Figure 3.4 : The function of $I=f(U)$ of various electrolytes tested for PEO treatment of aluminum: (1) fast metal (2) slow metal dissolution, (3) metal passivation in narrow voltage interval, (4) complex behavior with a wide interval of passivation, (5) slight passivation and (6) strong passivation of the metal.....	26
Figure 4.1 : Voltage-time responses for MAO coatings treated (a) in E1 electrolyte, (b) in E1 electrolyte, (c) first in E1 electrolyte then in E2, (d) first in E2 electrolyte then in E1.	31
Figure 4.2 : SEM micrographs for MAO coatings treated (a) in E1 electrolyte, (b) in E1 electrolyte, (c) first in E1 electrolyte then in E2, (d) first in E2 electrolyte then in E1.	32
Figure 4.3 : SEM micrographs of the cross-section of MAO coatings treated (a) in E1 electrolyte, (b) in E1 electrolyte, (c) first in E1 electrolyte then in E2, (d) first in E2 electrolyte then in E1.	33
Figure 4.4 : Voltage-time responses for anodizing aluminum (a) in processes 1 and 2, (b) in processes 3 and 4.....	34
Figure 4.5 : SEM images of surface of MAO coatings produced in: (a) process 1, (b) process (b), (c) process 3, (d) process 4.....	34
Figure 4.6 : The XRD spectra of the (a) coating surface, and inner layers at different distance from the interface (b) 120 μm , (c) 90 μm , (d) 60 μm	36
Figure 4.7 : The cross-sectional EPMA results of the MAO coating: (a) the back scattering electron image of the coating; (b) the change of element concentrations along coating thickness.....	37
Figure 4.8 : SEM image (secondary electron mode) of a polished section from a MAO coating.	37
Figure 4.9 : SEM image (back-scattered electron mode) of a polished section from a MAO coating.	38
Figure 4.10 : (a) low-magnification (b) high magnification SEM images (secondary electron mode) of MAO coating surfaces.....	39
Figure 4.11 : Change of layer thickness with treatment time for different current densities (a) 0,18 A/cm^2 (b) 0,38 A/cm^2 (c) 0,75 A/cm^2	41

Figure 4.12 : (a) SEM image and (b) EDS spectra of ceramic layer treated for 15 min.	42
Figure 4.13 : SEM images of the MAO coatings surfaces at 2000x magnification processed (a) pure Al ₂ O ₃ , (b) doped Al ₂ O ₃	43
Figure 4.14 : EDS analyses of the doped Al ₂ O ₃	43
Figure 4.15 : Surface morphology of (a) coating-0, (b) coating-1, (c) coating-2 and (d) coating-3.	44
Figure 4.16 : Friction coefficient of the coating with different concentrations of graphite (a) 0 g/l, (b) 2 g/l, (c) 4 g/l, (d) 8 g/l.	46
Figure 4.17 : Potentiodynamic polarization curves of the bare and MAO coated samples with different film thickness.	47
Figure 4.18 : Potentiodynamic polarization curves of aluminum substrate and the MAO coatings.	48
Figure 4.19 : Optical micrographs of MAO coatings on (a) as received and (b) shot-peened Al alloy substrates.	50
Figure 4.20 : Microhardness in as-received and shot-peened (a) aluminum substrate, (b) PEO coated specimens.	50
Figure 4.21 : Typical residual stress profile for shot-peened aluminum.	51
Figure 4.22 : Residual stress profiles for MAO coatings on (a) as-received, (b) shot-peened Al alloy substrates.	51
Figure 4.23 : S-N curves for four different surface conditions.	52
Figure 4.24 : (a) TG and (b) DSC curves of the MAO coatings. Heating rate 10 Kmin ⁻¹ , specimen mass 30mg.	53
Figure 4.25 : The thermal expansion of the MAO coatings.	53
Figure 4.26 : Dependence of anode currents on the distance between electrodes. ...	54
Figure 4.27 : Waveform of currents flowing through the front and back surfaces. ...	55
Figure 4.28 : Friction coefficient on the front and back surfaces.	55
Figure 4.29 : Potentiodynamic polarization curves obtained in 3,5% NaCl solution.	56
Figure 4.30 : The reflection rate of infrared wave from 780nm to 3000nm determined from the glass coated aluminum alloy and the MAO coatings having the thickness of (a) 14 μm, (b) 25 μm, (c) 38 μm, (d) 50 μm, (e) 66 μm.	57
Figure 5.1 : Micro arc oxidation apparatus.	59
Figure 5.2 : Applied voltage in square wave form.	60
Figure 5.3 : Schematic view of width and depth of the wear tracks.	63
Figure 6.1 : General view of the samples oxidized under constant voltage and constant current modes.	67
Figure 6.2 : Surface micrographs of the samples treated under voltage controlled and current controlled modes.	68
Figure 6.3 : X-Ray diffraction patterns of the sample V1.	69
Figure 6.4 : X-Ray diffraction patterns of the sample I1.	70
Figure 6.5 : Coating thickness of voltage controlled samples.	71
Figure 6.6 : Coating thickness of current controlled samples.	71
Figure 6.7 : Average surface roughness of the samples treated with constant voltage mode.	72
Figure 6.8 : Average surface roughness of the samples treated with constant current mode.	72
Figure 6.9 : The change of wear track area with positive and negative voltage.	73

Figure 6.10 : The change of wear track area with positive and negative current.	73
Figure 6.11 : Cross-sectional optical microscopy images of samples	75
Figure 6.12 : X-Ray diffraction patterns of the samples V150	76
Figure 6.13 : Coating thickness of the samples oxidized under voltage and current controlled modes.	77
Figure 6.14 : Average surface roughness of the samples oxidized under voltage and current controlled modes..	77
Figure 6.15 : Wear track area of the samples of the samples oxidized under voltage and current controlled modes.....	78
Figure 6.16 : General view of the MAO treated samples after pulse duration studies.	79
Figure 6.17 : Surface SEM micrographs of the samples oxidized for different pulse durations.....	80
Figure 6.18 : XRD patterns of the samples oxidized for different pulse durations. .	81
Figure 6.19 : Variation of coating thickness as a function of pulse durations.....	82
Figure 6.20 : Change of average surface roughness with different pulse durations	82
Figure 6.21 : Cross-sectional SEM analyses of MAO samples treated with different pulse duration time	84
Figure 6.22 : Micro-hardness values of MAO coatings treated with different pulse durations.....	85
Figure 6.23 : Relative wear rates of the bare alloy and MAO samples oxidized for different pulse durations.	86
Figure 6.24 : Specific corrosion loss of the samples as a function of immersion time.	87
Figure 6.25 : pH variation of the solution during immersion corrosion tests.	87
Figure A.1 : General view of the samples oxidized under constant voltage mode .	97
Figure A.2 : General view of the samples oxidized under constant current mode. .	98
Figure A.3 : General view of the samples oxidized to achieve maximum coating thickness.....	99
Figure A.4 : General view of the MAO treated samples after pulse duration studies.	100
Figure B.1 : Surface micrographs of the samples treated under voltage controlled mode.	101
Figure B.2 : Surface micrographs of the samples treated under current controlled.	102
Figure B.3 : Surface micrographs of the samples oxidized to achieve maximum coating thickness.....	103
Figure B.4 : Surface images of MAO treated samples treated with different pulse durations.	104
Figure C.1 : Cross-sectional optical microscope images of the samples treated with voltage controlled method.	105
Figure C.2 : Cross-sectional optical microscope images of the samples treated with current controlled method.....	106
Figure C.3 : Cross-sectional optical microscope images of samples treated with different pulse durations.	107
Figure D.1 : SEM surface images of samples treated to achieve maximum coating thickness.....	108
Figure E.1 : XRD pattern of the sample treated with the condition of V1.	109
Figure E.2 : XRD pattern of the sample treated with the condition of V2	109

Figure E.3 :	XRD pattern of the sample treated with the condition of V3	110
Figure E.4 :	XRD pattern of the sample treated with the condition of V4	110
Figure E.5 :	XRD pattern of the sample treated with the condition of V5	111
Figure E.6 :	XRD pattern of the sample treated with the condition of V6	111
Figure E.7 :	XRD pattern of the sample treated with the condition of I1	112
Figure E.8 :	XRD pattern of the sample treated with the condition of I2.....	112
Figure E.9 :	XRD pattern of the sample treated with the condition of I3.....	113
Figure E.10 :	XRD pattern of the sample treated with the condition of I4.....	113
Figure E.11 :	XRD pattern of the sample treated with the condition of I5.....	114
Figure E.12 :	XRD pattern of the sample treated with the condition of V100	115
Figure E.13 :	XRD pattern of the sample treated with the condition of V150	115
Figure E.14 :	XRD pattern of the sample treated with the condition of I410.....	116
Figure E.15 :	XRD pattern of the sample treated with the condition of I410.....	116
Figure F.1 :	Wear pattern of the sample treated with the condition of V1	117
Figure F.2 :	Wear pattern of the sample treated with the condition of V2	117
Figure F.3 :	Wear pattern of the sample treated with the condition of V3	118
Figure F.4 :	Wear pattern of the sample treated with the condition of V4	118
Figure F.5 :	Wear pattern of the sample treated with the condition of V5	119
Figure F.6 :	Wear pattern of the sample treated with the condition of V6	119
Figure F.7 :	Wear pattern of the sample treated with the condition of I1	120
Figure F.8 :	Wear pattern of the sample treated with the condition of I2.....	120
Figure F.9 :	Wear pattern of the sample treated with the condition of I3.....	121
Figure F.10 :	Wear pattern of the sample treated with the condition of I4.....	121
Figure F.11 :	Wear pattern of the sample treated with the condition of I5.....	122
Figure F.12 :	Wear pattern of the sample treated with the condition of I6.....	122
Figure F.13 :	Wear pattern of the sample treated with the condition of V100	123
Figure F.14 :	Wear pattern of the sample treated with the condition of V150	123
Figure F.15 :	Wear pattern of the sample treated with the condition of I410.....	124
Figure F.16 :	Wear pattern of the sample treated with the condition of I420.....	124
Figure F.17 :	Wear pattern of the sample treated with the condition of 521.	125
Figure F.18 :	Wear pattern of the sample treated with the condition of 522	125
Figure F.19 :	Wear pattern of the sample treated with the condition of 523	126
Figure F.20 :	Wear pattern of the sample treated with the condition of 524	126
Figure F.21 :	Wear pattern of the sample treated with the condition of 525.	127
Figure F.22 :	Wear pattern of the sample treated with the condition of 425	127
Figure F.23 :	Wear pattern of the sample treated with the condition of 325	128
Figure F.24 :	Wear pattern of 7075 bare aluminum sample.	128

INVESTIGATION OF SURFACE PROPERTIES OF A MICRO ARC OXIDIZED 7075 ALUMINIUM ALLOY

SUMMARY

Aluminum is a widely used material in industry since it's remarkable for its ability to resist corrosion due to the phenomenon of passivation and for the metal's low density ($2,7 \text{ g/cm}^3$). Unfortunately, aluminum suffers from its low hardness and low wear resistance furthermore its passive oxide layer is not able to protect itself in all kind of ambient like acidic, alkali and salt solutions.

One of the effective ways to improve hardness and wear resistance of aluminum is to produce thicker oxide layer on its surface, namely oxidizing aluminum surface. Microarc oxidation (MAO), also called as plasma electrolytic oxidation (PEO), is a novel technique to produce hard ceramic coatings on valve metals.

With the introduction of hard ceramic coatings by means of microarc oxidation, the wear resistance, corrosion resistance, mechanical strength, and electrical insulation of the valve metals and their alloys can be effectively increased.

Therefore, this novel coating technique, capable of depositing dense, hard ceramic composite coatings on aluminum and its alloys.

In this study, ceramic coatings were formed on 7075 aluminum alloy by micro arc oxidation in potassium hydroxide and sodium meta silicate solution, then appropriate process parameters for different applications were obtained by investigating the effect of the process parameters on the coating properties.

MIKRO ARK OKSİDASYON İŞLEMİ UYGULANAN 7075 KALİTE ALUMİNYUM ALAŞIMININ YÜZEY ÖZELLİKLERİNİN İNCELENMESİ

ÖZET

Alüminyum, düşük yoğunluklu bir metal oluşu ($2,7 \text{ g/cm}^3$) ve pasif oksit tabakası nedeniyle korozyona olan direnci dolayısıyla endüstride çok geniş kullanım alanları bulmuştur. Maalesef, alüminyum düşük sertliği ve düşük aşınma direncinden dolayı, bunların ilaveten üzerinde oluşan pasif oksit tabakası, asidik, bazik ve tuz çözeltileri gibi her ortamda kendisini koruyamaması ise, alüminyumun önemli dezavantajlarıdır.

Alüminyumun sertliğini ve aşınma direncini geliştirmenin bir yolu da, üzerinde kalın bir oksit tabakası oluşturmak yani yüzeyini oksitlemektir. Mikro Ark Oksidasyon (MAO), bir diğer deyişle plazma elektrolitik oksidasyon (PEO), “valve” malzemeler olarak adlandırılan malzeme grubunun yüzeyinde kalın sert kaplamalar elde etmeye yarayan yeni bir tekniktir.

Mikro ark oksidasyon yöntemiyle, sert seramik kaplamaların yüzeye tatbiki yoluyla, bu malzeme grubunun ve alaşımlarının aşınma direnci, korozyon direnci, mekanik dayanımı ve elektriksel yalıtımı etkili bir biçimde artırılabilir.

Bu çalışmada, mikro ark oksidasyon yöntemiyle, potasyum hidroksit ve sodyum metasilikat çözeltilerinde 7075 alüminyum alaşımı üzerine seramik kaplanmış ve sonrasında işlem parametrelerinin kaplama özellikleri üzerine etkisi incelenerek, farklı uygulamalarda kullanılmak üzere işlem parametreleri elde edilmiştir.

1. INTRODUCTION

Aluminum is a widely used material in industry since it is remarkable for its ability to resist corrosion due to the phenomenon of passivation and for the metal's low density ($2,7 \text{ g/cm}^3$). Unfortunately, aluminum suffers from its low hardness and low wear resistance furthermore its passive oxide layer is not able to protect itself in all kind of ambient like acidic, alkali and salt solutions.

One of the effective ways to improve hardness and wear resistance of aluminum is to produce thicker oxide layer on its surface, namely oxidizing aluminum surface. A number of techniques have been investigated to produce thicker ceramic coatings on aluminum components, which includes arc-discharge plasma and gas-flame spray, vacuum deposition methods and high temperature glass enameling. These techniques require a high substrate temperature to provide adequate coating adhesion at high contact loads [1].

Micro arc oxidation (MAO), also called as plasma electrolytic oxidation (PEO), is a novel technique to produce hard ceramic coatings on valve metals such as Al, Ti, Mg and their alloys, which is characterized by high temperature of 10^3 to 10^4 K and high local pressure of 102 to 103 MPa in the discharge channels [1].

The MAO process combines the electrochemical oxidation with a high voltage spark treatment in an aqueous electrolytic bath whose dissolved salt (e.g. silicates) can be decomposed to generate modifying elements to the alumina coating. With the introduction of hard ceramic coatings by means of Micro arc oxidation, the wear resistance, corrosion resistance, mechanical strength, and electrical insulation of the metals and their alloys can be effectively increased. This is especially true to Al and its alloys, which is imperative to extend the application fields of Al alloys in aerospace, automotive, textile engineering, etc. [1].

Therefore, this novel coating technique, capable of depositing dense, hard ceramic composite coatings on aluminum and its alloys, has the potential to replace conventional hazardous anodizing techniques [2].

In this study, ceramic coatings were formed on 7075 aluminum alloy by micro arc oxidation in potassium hydroxide and sodium meta silicate solution, then appropriate process parameters for different applications were obtained by investigating the effect of the process parameters on the coating properties.

2. ALUMINUM AND ITS ALLOYS

Aluminum's unique properties – its light weight, high strength, good ductility and resistance to corrosion – make it an ideal material for use in conventional and novel applications [3, 4]. Physical properties of aluminum are listed in Table 2.1.

Aluminum has become increasingly important in the production of automobiles and trucks, packaging of food and beverages, construction of buildings, transmission of electricity, development of transportation infrastructures, production of defense and aerospace equipment, manufacture of machinery and tools, and production of durable consumer products. As demand for more technologically complex and ecologically sustainable products increases, opportunities for aluminum will continue to expand.

Table 2.1: Physical properties of aluminum [4].

Property	Purity, %				
	99,999	99,99	99,8	99,5	99
Melting Point, °C		660,2	-	-	657
Boiling point, °C		2480	-	-	-
Latent heat of fission, cal/g		94,6	-	-	93
Specific heat at 100°C, cal/g		0,2226	-	-	0,2297
Density at 20°C, g/cm ³	2,7	2,7	2,71	2,71	
Electrical resistivity, μΩ-cm at 20°C	2,63	2,68	2,74	2,8	2,87
Temperature coefficient of resistivity		0,0042	0,0042	0,0041	0,004
Coefficient of thermal expansion x10 ⁶ (20-100°C)		23,86	23,5	23,5	23,5
Thermal conductivity, e.g. units at 100°C		0,57	0,56	0,55	0,54
Reflectivity (total), %		90	89	86	-
Modulus of elasticity lb/in ² x10 ⁻⁶		9,9	-	-	10

2.1 Definitions for Aluminum and Aluminum Alloys

Some widely used definitions for aluminum and aluminum alloys are given in the following sections [5].

2.1.1 Commercially pure aluminum

Commercially pure (CP) aluminum contains a minimum of 99% “pure” metal. Up to and including the “six nines” aluminum (i.e., 99.9999% pure aluminum) various specialty grades of higher purity exist for use in special applications [5].

2.1.2 Aluminum alloy

A material having metallic properties and composed of two or more elements of which at least one is an elemental metal. Most aluminum alloys contain 90 to 96% aluminum, with one or more other elements being added to give a specific combination of properties and characteristics. Generally imparting special fabrication or performance characteristics is achieved by using several minor alloying elements in addition to one or two major alloying elements [5].

2.1.3 Strain-hardenable aluminum alloy

A substance which the major and minor alloying elements do not provide any significant solid solution and precipitation strengthening during any type of thermal treatment. Therefore, these alloys must be strengthened principally by strain hardening (i.e., by cold rolling or drawing). The term of strain hardenable is used for these types of aluminum alloys [5].

2.1.4 Heat treatable aluminum alloy

This is the type of alloy for which the major and maybe some minor, alloying elements provide significant solid solution and precipitation strengthening during solution heat treatment and subsequent aging. The term of heat treatable is used for these types of aluminum alloys [5].

2.1.5 Wrought aluminum alloy

This term is used for alloys produced in ingot or billet form then subsequently worked by any of a number of metalworking processes such as drawing, rolling, extruding, forging, in order to produce semifinished products from which end-use products are subsequently made [5].

2.1.6 Cast aluminum alloy

This term is used to mean alloys that generally are used in parts cast to final or near-final shape and to the ingot from which such castings are made. Cast alloys are not generally used for subsequent rolling, extrusion, forging, or other metal shaping processes [5].

Since substance used in this study is 7075 aluminum alloy, it is appropriate at this stage to give some of the basic characteristics of wrought aluminum alloys that make them desirable candidates for a wide range of industrial applications [5].

2.2 Characteristics of Wrought Aluminum Alloys

2.2.1 Corrosion resistance

As a result of a naturally occurring tenacious surface oxide film, many aluminum alloys provide exceptional resistance to corrosion in many atmospheric and chemical environments. Alloys of the 1xxx, 3xxx, 5xxx, and 6xxx systems are especially favorable in this respect and are even used in applications where they are in direct contact with seawater and antiskid salts [5].

Aluminum has a resistance to corrosion in some common environments, including the ambient atmosphere. It has been associated with the presence a continuous oxide film on its surface. The standard electrode potential of aluminum is less than the majority of aluminum alloys. Therefore it protects aluminum by forming a protecting cathodic layer. In air at the room temperature, this film on a surface of aluminum will be formed in 10^{-4} sec. This film prevents further deterioration of the metal. Its thickness in usual conditions is 5-20 nm [4].

It can be seen in the following tables, Table 2.2 and Table 2.3 where there is considerable resistance to corrosion and where aluminum has poor corrosion resistance [4].

Table 2.2: Aluminum has good resistance toward these chemicals [4].

Acetic acid	Chlorides of sodium, potassium and magnesium	Milk products	Sulfides
Acetone	Detergents	Molasses	Sulfur
Acetylene	Emulsifier	Naphtha and naphthalene	Sulfur dioxide both dry and wet
Alum	Essential oils	Nitric acid strong	Tannic acid dilute
Ammonia	Fatty acids	Oxalic acid	Tartaric acid
Ammonium chloride	Fluorine	Phenol	Vegetable oils
Aniline and its compounds	Fruit juices	Seawater	Vinegar
Brine (saturated)	Glycerin	Silicic acid	Water
Calcium chloride	Hydrocyanic acid	Sodium silicate	Yeast
Carbon disulfide	Lactic acid	Starch	
Carbonic acid	Maleic acid	Sugar, syrups, etc.	
Chlorine (dry)	Meat juice	Sulfates of sodium, potassium and magnesium	

However, aluminum and its alloys are desirable in many fields because of its properties mentioned above, the poor wear-resistance of aluminum alloys in air and water decreases the service life of machine components [6].

Table 2.3: Aluminum cannot resist action of the following chemicals [4].

Calcium hypochlorite	Fluorine (wet)	Mercuric chloride	Sodium sulphite
Caustic soda	Hydrochloric acid	Nickel salts	Sulfur trioxide
Caustic potash	Hydrobromic acid	Nitric acid dilute	Sulfuric acid
Chlorine (wet)	Hydrofluoric acid	Phosphoric acid	Zinc chloride
Copper salts	Hydrogen peroxide	Sodium hypochlorite	

2.2.2 Thermal conductivity

Aluminum and its alloys are good conductors of heat though they have lower melting temperatures than steels, which is approximately 535 °C. Besides, in case of fire exposure they are slower than steel to reach very high temperatures [5].

2.2.3 Electrical conductivity

Pure aluminum and some of its alloys have outstanding high electrical conductivity (i.e., very low electrical resistivity), second after copper among common metals known as conductors [5].

2.2.4 Strength/Weight ratio

This specification of aluminum alloys gives an opportunity for replacement of heavier materials with no loss in load-carrying capacity. This characteristic, combined with excellent corrosion resistance and recyclability, made aluminum widely used in many industrial applications such as containers, aircraft, and automotive [5].

2.2.5 Fracture toughness and energy absorption capacity

Many aluminum alloys are exceptionally tough therefore they are excellent candidates for critical applications where resistance to brittle fracture and unstable crack growth are imperatives. Alloys of the 5xxx series, for example, are excellent candidates for storing liquefied natural gas. Besides, for critical bulkhead applications, special high toughness versions of aircraft alloys, such as 2124, 7050, and 7475, replace the standard versions of these alloys [5].

2.2.6 Cryogenic toughness

Aluminum alloys, especially of the 3xxx, 5xxx, and 6xxx series, are ideal where temperature of service conditions is very low because of the their ductility and toughness, as well as strength, are higher at subzero temperatures, even down to near absolute zero, than at room temperature [5].

2.2.7 Workability

A great variety of metalworking technologies can be applied on aluminum alloys readily. Aluminum alloys are especially amenable to extrusion. This characteristic enables aluminum to be produced in a remarkable variety of shapes [5].

2.2.8 Ease of joining

In addition to an unlimited variety of mechanical procedures aluminum alloys can be joined by a great variety of commercial methods, such as welding, brazing, soldering, riveting, bolting, and even nailing [5].

2.2.9 Recyclability

The easiest material to recycle among any structural materials is aluminum and aluminum alloys. They are recyclable in the truest sense, unlike materials that are reused in lower-quality products after recycling process; aluminum alloys may be recycled directly back into the same high-quality products, and still can be used in many components such as rigid containers, sheet, and automotive [5].

2.3 Aluminum Alloy and Temper Designation Systems

It is very useful for secondary fabricators and users of aluminum products and components to have a knowledge that provides a standard form for alloy identification. A great deal about the chemical composition and characteristics of the alloy can be easily understood by user. Similarly, the temper designation system enables the user to understand of the manner in which the material has been fabricated [5].

Aluminum industry adopted the alloy and temper designation system for wrought aluminum, that is in use today, at around 1955 and the system for the cast aluminum were developed in following years. The aluminum industry keeps creating and maintaining of these systems. The basic systems as defined and maintained by Aluminum Association will be described briefly in following parts [5].

2.3.1 Aluminum alloy designation system

Wrought Alloy Designation System maintained by Aluminum Association consists of four numerical digits, including sometimes alphabetic prefixes or suffixes.

The first digit indicates the major alloying class of the series [5].

The second one defines variations of basic alloy: it is always zero for the original composition, and one (1) defines the first variation, similarly a two (2) defines the second variation and so on. Depending on the quantity of the alloying elements, variations define the difference in one or more alloying elements of 0.15 to 0.50% or more [5].

The third and the fourth digits designate the alloying elements but they do not have special significance to the values of those digits and they do not have to be used in sequence [5].

According to first of the four digits, Table 2.4 shows the alloy family thereby associated main alloying ingredient(s) which are identified by that number with three exceptions [5].

- Members of the 1000 series family are commercially pure aluminum and unless is necessary for the application, they do not have any alloying elements intentionally added and except minor impurities.
- The 8000 series family is an “other elements” series having alloying elements such as iron, nickel etc.
- The 9000 series is unassigned [5].

Table 2.4: Main alloying elements in the wrought alloy designation system [7].

Alloy	Main alloying element
1xxx	Mostly pure aluminum; no major alloying additions
2xxx	Copper
3xxx	Manganese
4xxx	Silicon
5xxx	Magnesium
6xxx	Magnesium and Silicon
7xxx	Zinc
8xxx	Other elements (e.g. iron or tin)
9xxx	Unassigned

2.3.2 Aluminum alloy basic temper designation system

In the temper designation system, alloy designation is always followed by a hyphen (e.g., 2014-T6) [5].

The general class of the treatment applied on material is indicated by the first character in the temper designation. The designations are defined and described as follows:

- F, as fabricated: the designation “F” indicates that during the production process of wrought or cast aluminum there is no special control over thermal conditions or strain-hardening processes employed to achieve specific properties. Though for cast alloys there generally are mechanical property limits associated with this temper, there are no for wrought alloys.
- O, annealed: the designation “O” defines a wrought products that is annealed to obtain the lower strength temper, usually in order to increase subsequent workability. The O defines an annealing process to improve ductility and dimensional stability for cast products.
- H, strain hardened: The H indicates that the product has been hardened by strain hardening process. To gain some reduction in strength supplementary

thermal treatments may or may not be applied. Two or more digits always follow the H.

- W, solution heat treated: indicates only alloys that age spontaneously after solution heat treating process. This designation is used in combination with W to indicate the period of natural aging, for instance, W 1/2 h.
- T, The T shows that the alloy is thermally treated to produce stable tempers other than F, O, or H: During the treatment process supplementary strain hardening processes to produce stable tempers can be applied also. The T is always followed by one or more digits [5].

2.3.3 Subdivisions of the basic T temper

The specific combination of basic operations is indicated by the first number(s) following the letter T:

T1, indicates treatment that was cooled from elevated temperature shaping process then naturally aging to a substantially stable condition: Defines the products (a) that are not cold worked after cooling from an elevated temperature shaping process or (b) which the effect of cold work in flattening or straightening may not be recognized in mechanical property limits

T2, cooled from an elevated temperature shaping process, cold worked, then naturally aged to a substantially stable condition: Defines the products (a) that are cold worked to improve strength after cooling from an elevated temperature shaping process or (b) which the effect of cold work in flattening or straightening is reaches to mechanical property limits

T3, solution heat treated, cold worked, and naturally aged to a substantially stable condition: Applies to products (a) that are cold worked to improve strength after solution heat treatment or (b) for which the effect of cold work in flattening or straightening is recognized in mechanical property limits

T4, solution heat treated and naturally aged to a substantially stable condition: Applies to products (a) that are not cold worked after solution heat treatment or (b) for which the effect of cold work in flattening or straightening may not be recognized in mechanical property limits

T5, cooled from an elevated temperature shaping process, then artificially aged: Applies to products (a) that are not cold worked after cooling from elevated temperature shaping process or (b) for which the effect of cold work in flattening or straightening may not be recognized in mechanical property limits

T6, solution treated, then artificially aged: Applies to products (a) that are not cold worked after solution treatment or (b) for which the effect of cold work in flattening or straightening may not be recognized in mechanical property limits

T7, solution heat treated and overaged/stabilized: Applies to (a) wrought products that are artificially aged after solution heat treating to increase their strength beyond the maximum value achievable to provide control of some significant property or characteristic or (b) cast products that are artificially aged after solution treatment to provide stability in dimensions and in strength

T8, solution heat treated, cold worked, then artificially aged: Applies to products (a) that are cold worked to improve strength or (b) for which the effect of cold work in flattening and straightening is recognized in mechanical property limits

T9, solution heat treated, artificially aged, and then cold worked: Applies to products that are cold worked to improve strength

T10, cooled from an elevated temperature shaping process, cold worked, then artificially aged: Applies to products (a) that are cold worked to improve strength or (b) for which the effect of cold work in flattening or straightening is recognized in mechanical property limits [5].

Solution heat treatment is achieved by following three steps in all of the T-type temper definitions just described:

1. Heating cast or wrought shaped products to an appropriate temperature
2. Holding products at that temperature long enough to allow constituents to enter into solid solution
3. Cooling them necessarily enough to hold the constituents in solid solution to enable subsequent precipitation and the associated strengthening (i.e., precipitation hardening) [5].

2.4 7xxx, Aluminum-Zinc Alloys

As mentioned before the 7xxx alloys are heat treatable and when combined with copper and magnesium provide the highest strengths of all aluminum alloys. The 7xxx series are not considered weldable and are generally riveted in constructions. Unfortunately as a group, the 7xxx alloys possess relatively poorer atmospheric corrosion resistance compared with other aluminum alloys especially with 5xxx and 6xxx alloys. Hence they are usually used as coated or alclad in service conditions. Moreover, special heat treatments have been developed to enhance their resistance to exfoliation and SCC, namely T76 and T73 respectively. Besides their poorer atmospheric corrosion resistance, they possess less toughness and are more susceptible to stress-corrosion cracking under short-transverse stressing. Special treatments have been developed to overcome these drawbacks and these treatments are essential when the alloys would have subjected to high short-transverse stresses in service conditions [5].

The widest use of the 7xxx alloys has been in the aircraft industry since high toughness alloy development was always essential for fracture-critical design concept. There are several alloys produced for this purpose, notably 7150, 7175, 7475 providing a very good combination of strength and fracture toughness. Applications of 7xxx alloys also include critical aircraft wing structures of integrally stiffened aluminum extrusions, long-length drill pipe and premium forged aircraft part [5].

3. THE MICRO ARC OXIDATION PROCESS

The Micro arc Oxidation is a novel technique capable of depositing ultra-hard and corrosion resistant oxide ceramic coatings on valve materials such as Al, Ti, Mg and their alloys [2]. The process of MAO is similar to anodic oxidation. In this process electrochemical oxidation is combined with a high voltage plasma discharge treatment in a definite solution [8]. Essentially, the process stimulates the forming of a hard, dense, thick ceramic layer on substrate surface [8]. The coating is composed of substrate alloying elements and electrolyte additives [8].

In this section, micro arc oxidation process will be introduced by discussing its specifications.

3.1 History of the Micro Arc Oxidation

The discharge phenomena associated with electrolysis during the anodizing of metals were discovered by Sluginov in 1878. It was studied in detail and the first comprehensive study of these phenomena was published in the 1932 by Günterschultze and Betz. The practical benefits of discharge phenomena were first exploited only in the 1960s, when McNeill and Gruss used a spark anodizing to deposit cadmium niobate ($\text{Cd}_2\text{Nb}_2\text{O}_7$) onto a cadmium anode in an Nb-containing electrolyte. McNeill and Gruss took a wide-ranging patent for “anodic spark reaction processes and reactions”, granted in 1966. Oxide deposition on an aluminum anode an arc discharge condition was also developed and studied by Markov and coworkers in 1970s. The first USSR patent for a “method of coating metals using anodic discharges” was filed in 1974 by Gradovsky. Meanwhile the first study of “Mechanism of Anodic Spark Deposition” was published by Van et al. Later this technique was improved and termed “micro-arc oxidation”. In 1982, a patent for “AC and pulsed bipolar processes for the production of hard oxide ceramic coatings on Al” was filed by Markov et al. In the development of this process, the start of Russian research into the process as a competitor for hard anodizing was a major milestone. Eventually, its potential benefits had been recognized, and commercial

interests increased. During the 1980s the possibilities of utilizing surface discharges in oxide deposition onto various metals were studied in more detail in Russia by Snezhko and coworkers, Markov and coworkers, Fyedorov et al, Gordienko and coworkers and in the Germany by Kurze and coworkers, where early industrial applications were introduced. Owing to the relatively sparse information on process phenomenology and, sometimes, a lack of understanding, different (and not always physically correct) terminology has been used in much of the above studies for what is, essentially, the same technique: “micro-plasma oxidation”, anode spark electrolysis”, “plasma electrolytic anode treatment”, being typical examples of descriptions common to “plasma electrolytic oxidation” [9, 10].

The MAO process can be applied on materials which are known as valve metals such as Al, Mg, Ti, Ta, W, Zn, Zr and their alloys. These metals in their natural state protect themselves by an oxide films which are thin, tightly adherent, self-healing and resist the passage of current in the anodic direction [1, 2, 11, 12].

3.2. Equipment

Schematic view of a typical MAO treatment unit was given in Figure 3.1. The unit basically consists of an electrolyte cell and a high power electrical source. A container made of stainless steel which also serves as the counter electrode, is used as electrolytic cell. It is placed on a dielectric base and confined in a grounded steel frame. The electrolytic cell incorporates recycling, electrolyte mixing, gas exhausting arrangements and electrical interlocks. The safety of operating personnel can be provided by the earthed frame, interlocked door and ventilated exhaust [10].

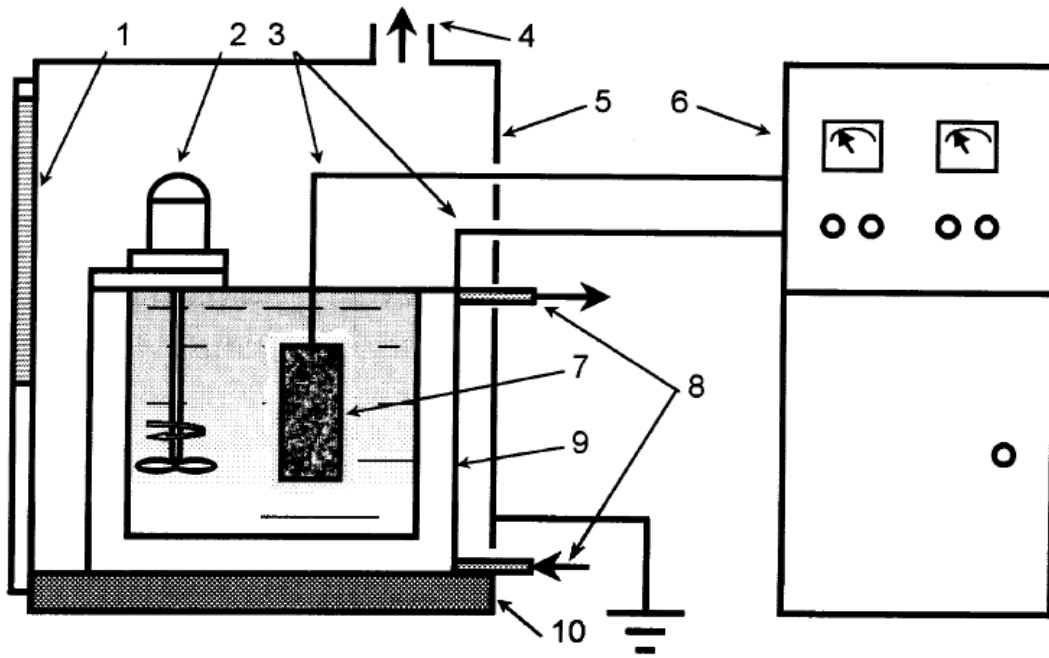


Figure 3.1: Typical arrangement of the equipment used for PED treatment: (1) window, (2) mixer, (3) connecting wires, (4) exhaust/ventilation system, (5) grounded case, (6) power supply unit, (7) work piece, (8) cooling system, (9) bath, (10) insulating plate [10].

3.3 Mechanism of the Process

A number of electrode processes are observed during the electrolysis of aqueous solution, Figure 3.2. Depending on the electrolyte chemical activity in respect to metal, the liberation of gaseous oxygen and/or metal oxidation, namely oxide film formation, can occur on the anodic surface. On the cathodic surface, it can result in liberation of gaseous hydrogen and/or cation reduction. A simplified model, two-phase system (i.e. metal–electrolyte or oxide–electrolyte couple) with a single phase boundary consisting of a double-charged layer that represents electrode–electrolyte interface is used for electrode processes when a conventional electrolytic process (e.g. electroplating, electrochemical machining, anodising, etc.) is studied. Product processes, such as gas liberation, can be taken into account using some correction factors, e.g. ‘current yield’ or ‘electrode shielding’ coefficients or neglected. Since the results are affected by the processes that occur in the gaseous environment surrounding the electrode and/or in its surface layers, this simplification is not always justifiable [10].

The characteristic current–voltage profile of the electrochemical system is affected by the above-mentioned processes as seen in Figure 3.3. In this process, current–voltage plot of metal–electrolyte pair can be represented by either a ‘type-a’ curve that represents system with underlying gas liberation on either the anode or cathode surface; or ‘type-b’ curve that represents a system where oxide film formation occurs. For both systems, the kinetics of the electrode processes at low voltages, conform to Faraday’s laws and the change of current–voltage is according to Ohm’s law. Therefore, a rise in the current needs a proportional increase in voltage (region ‘0- U_1 ’ in the type-a system and ‘0- U_4 ’ in the type-b system). But, the behavior of a particular system may change significantly beyond a critical voltage [10].

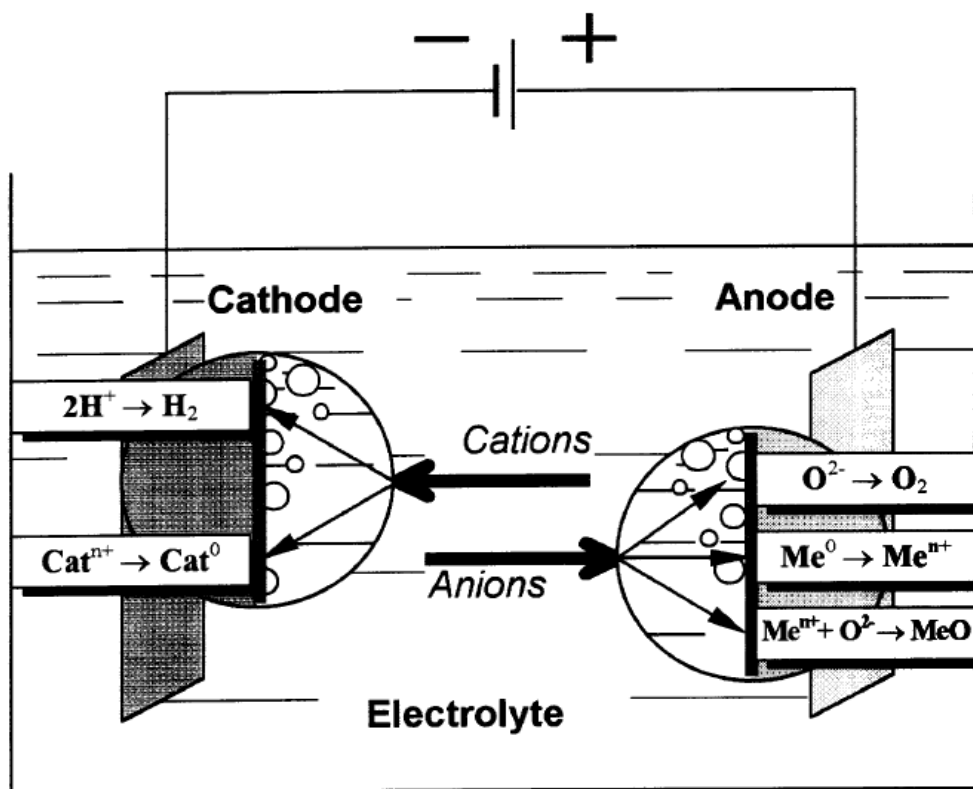


Figure 3.2: Electrode processes in electrolysis of aqueous solutions [10].

For a type-a system; a potential rise causes to current oscillation accompanied by luminescence in the region U_1 – U_2 . Partial shielding action of gaseous reaction products (O_2 or H_2) over the whole electrode surface limits current increase. Since the electrode is still in contact with the electrolyte, however, the current density continues to rise, causes local boiling of the electrolyte. Up to point U_2 , continuous gaseous vapor plasma envelope of low electrical conductivity enshrouds the electrode. Since in this thin region, where adjacent to electrode, almost all of the

voltage across the cell is now dropped, the electric field strength E reaches a value between 10^6 and 10^8 V/m. This value is sufficient for initiation of ionization processes the vapor envelope. The ionization phenomena which appear initially as a rapid sparking in scattered gaseous bubbles, becomes a uniform glow distributed throughout the envelope. In the region U_2 - U_3 , the current drops due to the hydrodynamic stabilization of the vapor envelope, and beyond this, the glow discharge transforms into intensive arcing accompanied by a characteristic low-frequency acoustic emission [10].

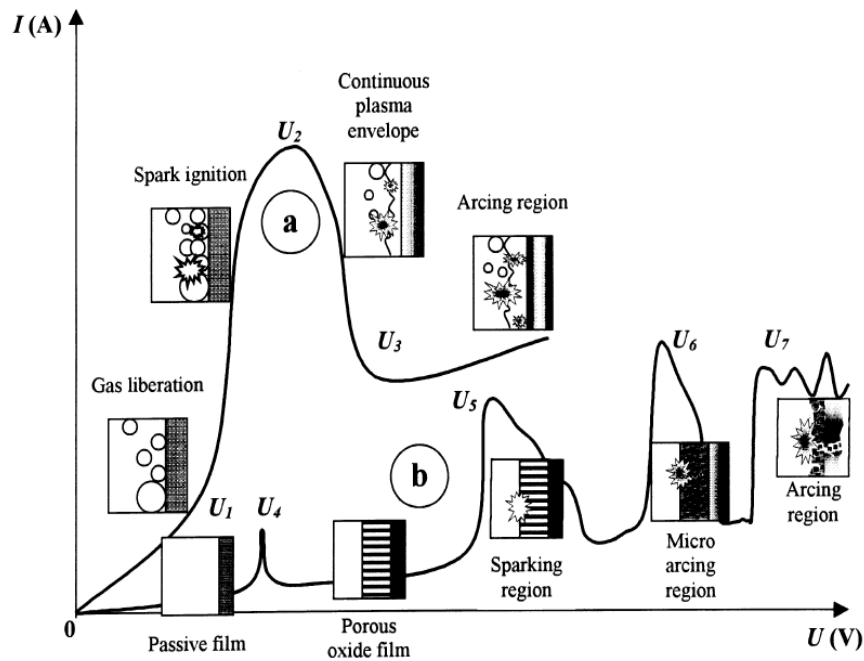


Figure 3.3: Two kinds of current-voltage diagram for the process of plasma electrolysis discharge (a) in the near-electrode area and (b) in the dielectric film on the electrode surface [10].

The behavior of type-b systems is more complicated. Firstly, the previously formed passive film starts to dissolve at a point, namely U_4 , which is defined as the corrosion potential of the material. Then, in the region, between U_4 - U_5 points, where most of the voltage drop occurs, a porous oxide film grows and repassivation occurs. At point U_5 , a critical value beyond which the film is broken through due to impact or tunneling ionization is reached by the electric field strength in the oxide film. Thus, small luminescent sparks, facilitating the film growth, are observed to move rapidly across the surface of the oxide film [10].

At point U_6 , the onset of thermal ionization supports the mechanism of impact ionization, and larger arc discharges arise. In the region U_6 and U_7 , negative charge built-up in the bulk of the thickening oxide film partially blocks thermal ionization. This results in discharge-decay shorting of the substrate. Low power and duration of the resultant arc discharges, i.e. micro discharges, which are termed misleadingly termed ‘micro-arcing’, are determined by this effect. The film is gradually fused and alloyed with elements contained in the electrolyte. Above the point U_7 , the micro discharges occurring throughout the film penetrate through the film. Micro-discharges transform into powerful arcs which may cause destructive effects such as thermal cracking of the film since negative charge blocking effects can no longer occur [10].

3.4 Application of the MAO process

Ceramic coatings showing the wear resistance, corrosion resistance, good adhesion to substrate, high temperature shock, electronic insulation etc with remarkable thickness can be obtained by means of the MAO. MAO coatings formed on aluminum alloy gives opportunity of wide use in many fields and a potential substitution of steel with aluminum alloys. Hence, to study the formation characteristics, mechanical and physical properties of the MAO coatings have technological importance in applications [13, 14].

The excellent mechanical, corrosion, electrical and thermal properties of these coatings are of particular interest to many application fields, such as automobile, aerospace, medicine and textile engineering, water purification, chemical industry, biomedical devices, oil extraction, refining machinery, etc [10, 14-18].

The MAO coatings are known to be applied for strengthening the components of the internal combustion engine components, to cycle components (wheel rims, spokes, frames), to golf club products (a patent covers this application), and used in Formula One Racing manufacturing (piston crowns, con-rods), and other major automotive manufacturing, such as GM [19, 20].

The data in Table 3.1 shows that the MAO coatings can successfully compete with anodizing and thermal oxidation techniques as well as provide above mentioned properties in a wide range of industries [10].

3.5 Advantages and Disadvantages of the Process

The MAO process does not need additional operations, such as etching or surface activation. Before the operation, necessary pretreatments are only cleaning and degreasing. The MAO process can compare favorably on cost with vacuum deposition and electroplating techniques owing to simplicity of operation [10]. The MAO is a non line of sight process and it has atmospheric working environment [21].

The MAO is basically an electrochemical oxidation with a high voltage spark treatment [18]. So, the process of MAO can be also defined as “hard anodizing” but unlike hard anodizing, all known aluminum alloys, including AlBeMet (beryllium containing) and MMCs, can be coated by means of the MAO process [2,18]. The coatings obtained by the MAO process are thicker and denser and they exhibit better mechanical properties superior to anodic oxide coatings [3, 8, 18].

The coating process is characterized by high productivity, economic efficiency, ecological friendliness, heat resistance up to 870°C, corrosion resistance, high temperature shock, electronic insulation, high hardness, good wear resistance, excellent bonding strength with the substrate [13, 22, 23].

Another advantage of this process is being able to modify electrolytes. Additives entered into electrolyte are contained in the compositions of these MAO coatings. Hence, depending on purpose, by changing the composition of electrolyte composition of MAO coatings can be modified [24].

Samples, synthesized through the MAO process, can maintain its original size by grinding loose layer on it. Thus, sample dimension can be controlled after the MAO treatment [25].

Compared to vacuum based plasma processes, the MAO process is a non line of sight process [21].

The high expense in terms of necessary power setup is the only disadvantage of this process [26].

Table 3.1: Applications and the characteristic properties in the MAO techniques [10].

Field of application		Material/treatment to be substituted	Advanced material/treatment		Characteristics of effectiveness	
Industry/unit	Component		Substrate	Coating	Technical	Economical
Textile machine building/Spinning & winding frames, looms, pattern cutting machines	Rotors, needle casing elements	High strength Al-alloy/deep anodizing	High strength Al-alloy/PEO	α -Al ₂ O ₃ , 100-150 μ m, 15-18 Gpa	200-300% increased lifetime, reduced thread fluffiness	60-80% reduced production cost
	Winding drums, rolls Shuttle cases	Steel/Cr electroplating				
	Cutting knives	Tool steel/hardening	Medium carbon steel/PEB	B ₄ C, 100-150 μ m, 4-5 Gpa	200-300% increased lifetime, 100-200% reduced friction	Production time & cost reduced by 80% and 20-30%, respectively
Gas- and oil- industry/ gear-, rotary-, immersed-pumps; locking fittings and valves	Operating wheels, sealing rings	Stainless steel, cast iron	Al-Mg alloy/PEO	γ -Al ₂ O ₃ , 60-120 μ m, 10-14 Gpa	150-200% increased lifetime, weight and inertial force reduction	50-60% reduced production costs
	Locking disks and spheres	Sintered ceramics			10-20% increased lifetime, absence of cracking	70% reduced production costs
Engine industry/diesel-, gasoline- & electric engines	Cases	Al-alloy/colored anodizing	Al-Mg alloy/PEO	γ -Al ₂ O ₃ , 60-120 μ m, 10-14 Gpa	Improved heat exchange	60% reduced production cost
	Pistons	Al-Si alloys/ depth anodising				
	Cylinder liners	High strength cast iron	Al-Si alloy/PEO	Mullite, 100-150 μ m, 6-10 Gpa	160-250% increased lifetime, reduction of fuel consumption	Up to 80% reduced production cost
Electrical engineering & electronics/electrolytic capacitors, heat sinks	Electrode foils	Al/anodizing	Al/PEO	γ -Al ₂ O ₃ , 30-50 μ m	20-50% increased capacity	Up to 80% reduced oxidation time
	Heat sinks	Al-alloy/colored anodizing	Al-alloys/PEO		Improved heat exchange	Up to 60% reduced production cost

Table 3.1 (Continued)

Field of application		Material/treatment to be substituted	Advanced material/treatment		Characteristics of effectiveness	
Industry/unit	Component		Substrate	Coating	Technical	Economical
Biomedical industry/ Mixers, prostheses	Blades	Stainless steel	High strength Al-alloy/PEO	α -Al ₂ O ₃ , 120-160 μ m, 14-18 Gpa	160-250% increased lifetime	Up to 70% reduced production cost
	Implants, endoprosthese	Ti	Ti/PEO	TiO ₂ 4-10 μ m	Improved biocompatibility	N.A.
Vacuum engineering/Turbo molecular pumps, evaporators	Rotors, stators, wheels	Stainless steel	High strength Al-alloy/PEO	γ -Al ₂ O ₃ , 50 μ m, 14 GPa	200% increased lifetime, reduced vibration	About 80% reduced production cost
	Boats	W, Mo, C, B, Ta	Al, Ti, C/PEO	α -Al ₂ O ₃ , 160-200 μ m, SiO ₂ , 400-600 μ m	50-300% increased lifetime	Reduced production cost
Air & space industry/gears, optical-devices	Gears, wheels	Stainless steel	High strength Al-alloy/PEO	γ -Al ₂ O ₃ , 60-120 μ m, 10-14 GPa	Up to 100% increased lifetime, weight reduction	60% reduced production cost
	Cases	Ti/thermal oxidation	Ti/PEO	TiO ₂ 4-10 μ m	Higher heat absorbency, and emission	N.A.
Vessel building industry/vessel pipework and devices	Pipes, fittings, device cases		Ti/PEO	TiO ₂ 4-10 μ m	Increased corrosion resistance	Up to 90% reduced production time
	Screw			Al ₂ TiO ₅ 50-100 μ m, 4-6 GPa	20-30% reduced friction	
Tool industry/cutting & pressing tools	Cutting tools, drills, mills	High speed steel/hardening	High speed steel/PEB	α -WB, W ₂ B ₅ , B ₄ C 100-150 μ m, 4-5GPa	50-150% increased lifetime	Production time & cost reduced by %70 & 20-30% respectively
	Pressing moulds	Tool steel/carbonizing/hardening	Tool steel/PEC/N	ϵ -Fe ₃ (CN), γ , (γ' + α), 300-450 μ m, 4-5 GPa	50-150% increased lifetime	60% reduced production cost

3.6 Power Supplies

Various types of power sources can be used to perform the MAO process. They can be divided into the following groups according to the electrical regime [10].

DC Sources are normally based on a bridge circuit and allow the application of galvanostatic or potentiostatic regimes of direct current. Difficulty in regulating the surface discharge characteristics limits the possibility for controlling the MAO process. Therefore, those power sources are used only for thin coatings and simple-shape components [10].

Another group of power supplies is *Pulsed DC Sources*. Controlled interruption of the process (i.e. arc duration) and various pulse forms can be provided by the application of Pulsed DC sources. The heat condition, coating composition and structure of the film can be controlled by means of pulsed current. However, the pulsed current can cause an additional polarization of the electrode surface due to the creation of a charged double layer. In this case, desired current density can be reached at higher voltage levels (up to 1000V). Pulsed current is widely used for the applications which a relatively low voltage (typically less than 450V) is required [10].

Unbalanced AC Sources Additional polarization of the electrode can be avoided by using AC sources, while the possibility of improved process control by means of arc interruption is retained. Moreover, the application of unbalanced AC makes it possible to extend the controlled range of coating deposition. The controlled capacitor-based multiplier is the simplest circuit of this type of power source. In this circuit, electrical energy is redistributed by high voltage capacitors according to the total resistance of the cell in the positive and negative half-cycles. The ratio of amplitudes of positive and negative current can be independently adjusted by varying the capacitance of the source in both half-cycles. The limitations in the power (typically 10 kW) and current frequency (mains frequency only) are the principal disadvantages [10].

Sources of heteropolar pulsed current can be used to supply higher power and/or a range of frequencies. These sources are based on thyristor- or transistor-reversible converters. Thyristor based circuits allow the production of rectangular or truncated

sinusoidal pulse shapes while transistors have added flexibility in programmed pulse shapes, amplitudes and durations [10].

3.7 Electrolytes

In the MAO process, appropriate metal-electrolyte combination must be selected depending on purposes. For this selection, polarization test data which are used for metal passivation, can be used [18]. Although, generally alkaline electrolytes containing silicates, aluminates, polyphosphates, carbonates, borate, etc., are used for the MAO treatment, MAO coatings are mainly composed of aluminum oxide [27, 28]. According to anodic polarization behavior of additives, they can be divided into following six groups;

1. Solutions of salts that provide fast dissolution of aluminum, such as NaCl, NaClO₃, NaOH, HCl, NaNO₃;
2. Electrolytes providing slow metal dissolution, such as H₂SO₄, (NH₄)₂S₂O₈, Na₂SO₄;
3. Electrolytes providing metal passivation in a close range of voltages, such as sodium acetate or phosphoric acid;
4. Fluoride electrolytes, which are characterized by complex behavior, such as KF, NaF;
5. Electrolytes promoting slight passivation of the metal;
6. Electrolytes promoting strong metal passivation, such as. boric acids and salts of carbonic and phosphoric acids, inorganic polymers (e.g. silicates, aluminates, tungstates, molybdates) and phosphates of alkaline metals (which can form polymer anions).

The function $I=f(U)$ of various electrolytes tested for PEO treatment of aluminum can be seen in Figure. 3.4.

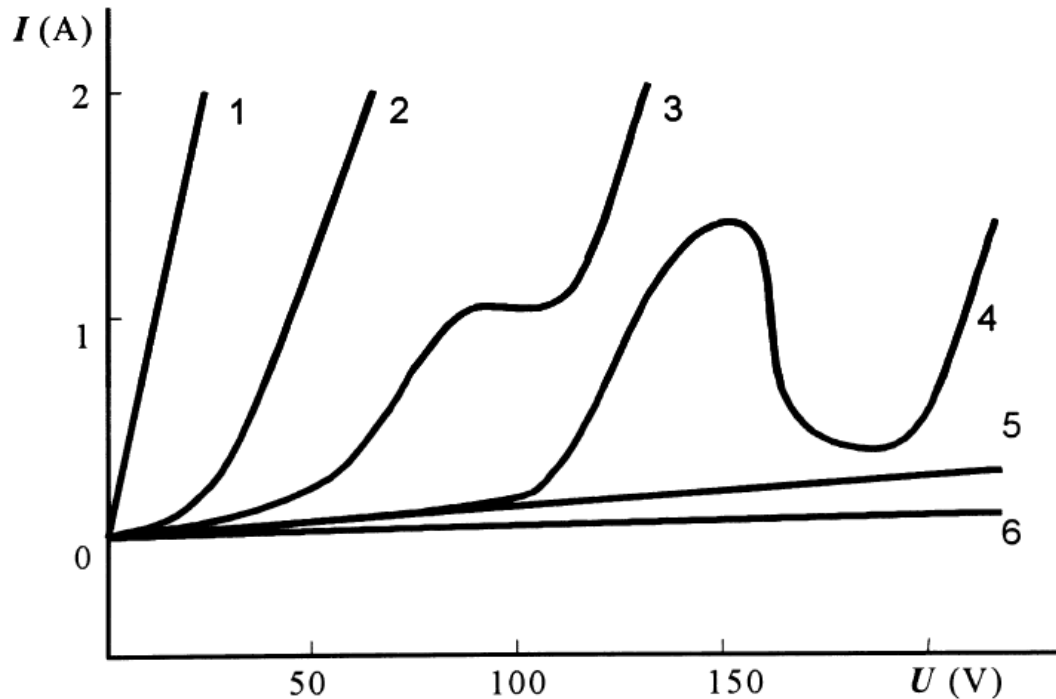


Figure 3.4: The function $I=f(U)$ of various electrolytes tested for PEO treatment of aluminum. Anodic polarization can lead to: (1) fast metal (2) slow metal dissolution, (3) metal passivation in narrow voltage interval, (4) complex behavior with a wide interval of passivation, (5) slight passivation and (6) strong passivation of the metal [10].

One important issue for the MAO process that the microstructure, composition and property of formed ceramic layer can be changed by small quantity of some additives in solution [27]. For instance;

- Adding oxalate, fluoride, cyanide, etc. into solution promotes formation of layers with diverse chemical composition [27];
- increase in hardness of MAO coatings obtained by Adding Na_3AlF_6 and $\text{C}_4\text{H}_4\text{O}_6\text{K}_2$ [27];
- adding sodium tungsten into solution increases wear resistance of ceramic layer [27];
- the growth rate of MAO coatings can be increased by increasing the Si content in solution. But an increase in the Si content also provides softer alumina silicate phase (Al-Si-O), therefore reduces the hardness [18];

- an increase the ratio of the thickness of internal dense layer to the total thickness is obtained by adding inorganic salt ($\text{Na}_2\text{WO}_4 \cdot 2\text{H}_2\text{O}$), thereby reducing the deposition rate; on contrary, adding SiC into electrolyte reduces the ratio of dense layer thickness to the total MAO ceramic coating thickness [18];
- Butyagin et al. [19], obtained highly resistant and thermostable MAO coating by adding KOH, Al_2O_3 (ultra-dispersible powders) and compounds of transition metals into electrolyte;
- Yerokhin et al [27], formed black ceramic layers by adding NH_4VO_3 into electrolyte.

4. THE MICRO ARC OXIDATION OF ALUMINUM

Weight-saving materials have a strategical and structural importance for modern technologies, especially in automotive and aerospace industries. Since aluminum alloys possess high strength-to-weight ratio, good ductility, great workability and corrosion resisted, it is commonly used in these fields. Engineers would like to make more extensive use of light metals such as aluminum, titanium, magnesium and their alloys, however they exhibit poor wear resistance, low hardness thereby decreasing the service life of machine components. Therefore, these drawbacks make aluminum surface treatment necessary for some industrial applications [29, 30].

Conventional surface treatment applications such as hard anodizing, thermal spraying, PVD, etc., reduce the durability and they exhibit limited performance in service conditions. For instance, hard anodizing and thermal spraying suffer from low load support and insufficient adhesion. Moreover, PVD coatings under mechanical loading, exhibit limited performance [1, 3].

As mentioned in previous chapters, Al_2O_3 coatings treated by means of the MAO process are potentially very effective in developing hard, wear resistant, corrosion resistant, etc. Moreover by using the MAO in different electrolytes, the properties of ceramic coating can be considerably increased depending on the purpose of study [3, 30].

There are lots of studies in literature related with the MAO treatment in order to form MAO coatings with different properties. This section is focused not only on these treatments but also on the MAO process parameters affecting the mechanical, performance and structural and chemical properties of the coatings. In this section, different MAO coatings performed in the open literature, according to their purpose or studied properties, are covered.

4.1 Structural and Morphological Properties of the MAO Coatings

There are a lot of factor that define quality of the MAO coatings such as current mode, the composition of electrolytes, the temperature of electrolyte and sample composition as well. Since electrolyte species incorporate into the anodic substance during the oxidation, among all these parameters the composition of electrolytes act as the most important one. Gu et al. [17], studied morphology of the MAO coatings using two widely used electrolyte, i.e. silicate and phosphate.

The MAO coatings were performed these two electrolytes as seen in Table 4.1. The recorded voltage and time responses for the MAO in the individual silicate and phosphate electrolytes showed similar initial voltage rises as seen in Figure 4.1 (a). Upon resumption of the MAO process following transfer of specimen from the phosphate electrolyte to the silicate electrolyte, the applied voltage fallen from 459V to 441V. On the contrary, upon resumption of the MAO process following transfer of specimen from the silicate electrolyte to the phosphate electrolyte, the applied voltage increased from 428V to 446V. The time-voltage behaviors can be seen in Figure 4.1 (b), (c) [17].

Table 4.1: The MAO processing parameters [17].

Sample	Process procedure
1	Individual in E1 for 30 min
2	Individual in E2 for 30 min
3	First in E2 for 30 min and then in E1 for 30 min
4	First in E1 for 30 min and then in E2 for 30 min

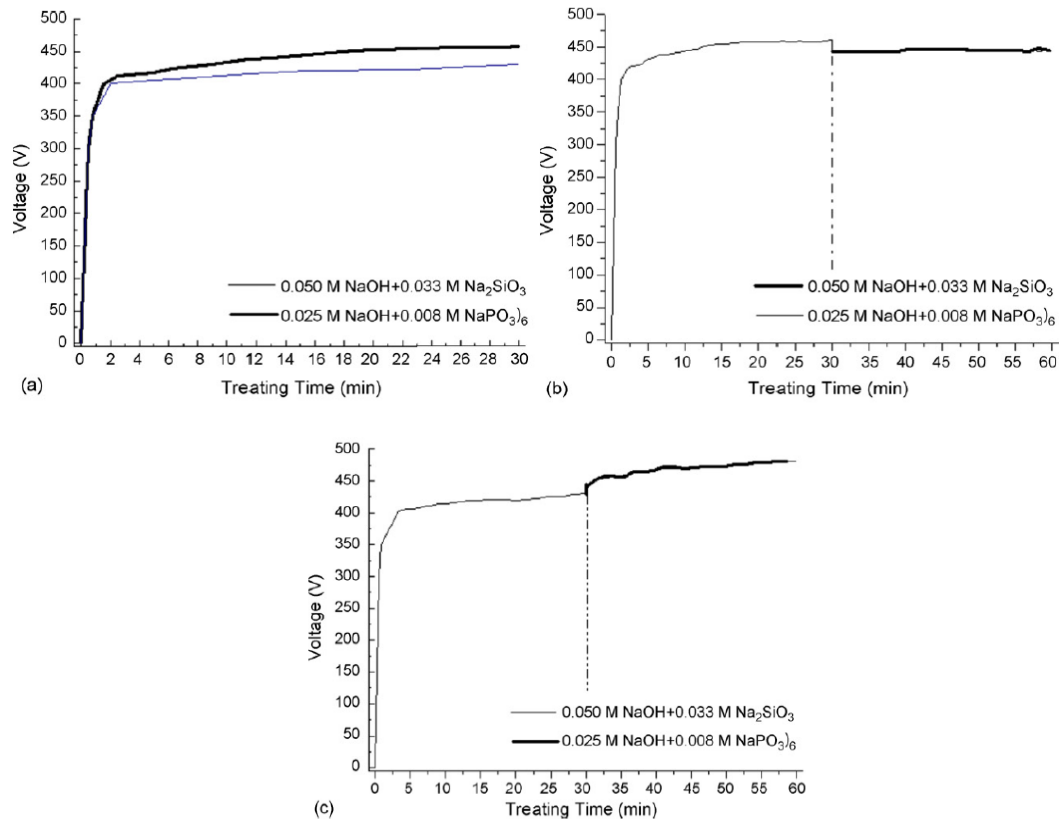


Figure 4.1: Voltage-time responses for MAO coatings treated (a) in E1 electrolyte, (b) in E1 electrolyte, (c) first in E1 electrolyte then in E2, (d) first in E2 electrolyte then in E1 [17].

Surface morphologies of the oxide coatings treated with those conditions being presented in Figure 4.2 reveal typical features of dielectric breakdown, with pores of micro and submicrometer sizes. It is obvious the change of surface morphology with the change of electrolytes. The coating deposited in silicate electrolyte reveals relatively uniform surface morphology as seen in Figure 4.2 (a). Many micro pores are to be existing having sizes in the range from 1 to 3 μm while in the phosphate electrolyte the average diameter of the micro pores is more than 8 μm . Besides, pan-like structures can be seen in Figure 4.2 (b) which belongs to the MAO coating formed in phosphate electrolyte. Morphology of the ceramic coating formed in phosphate electrolyte indicates the presence of violent discharging and concentrated sintering. Moreover, the presence of cracks near pan-like structure can be seen. These micro pores formed in the phosphate electrolyte change into smaller ones having an average diameter of 5 μm after sequential treating in the silicate electrolyte and some of the cracks disappear on the surface. Furthermore, the surface in Figure 4.2 (c) is more homogeneous as compared with that of Figure 4.2 (b) and (d). Many

micro pores including some long continuous ones, are found to be existing in the coating formed first in the silicate and then in phosphate electrolyte as seen in Figure 4.2 (d) [17].

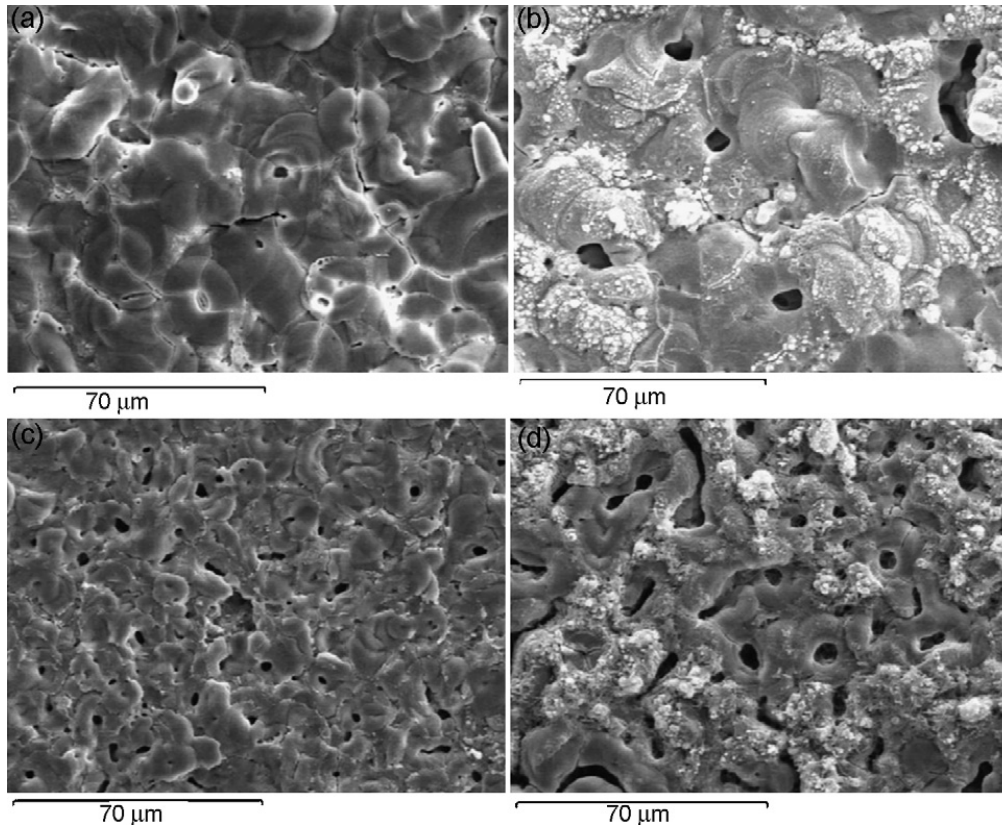


Figure 4.2: SEM micrographs for the MAO coatings treated (a) in E1 electrolyte, (b) in E1 electrolyte, (c) first in E1 electrolyte then in E2, (d) first in E2 electrolyte then in E1 [17].

The SEM images of cross-section of the MAO coating treated in the phosphate electrolyte are found to be having more porous structure and many large cracks which are consisted with its relatively coarse surface as presented in Figure 4.2 (b). As shown in Figure 4.3 (c), the cross-section of the MAO coating treated in phosphate electrolyte became a little dense after a sequential treatment in silicate electrolyte. Although, big defects can still be seen at the interface region of the substrate and the ceramic coating. Consequently, samples 1 and 4 have relatively denser structure as compared with that of samples 2 and 3 [17].

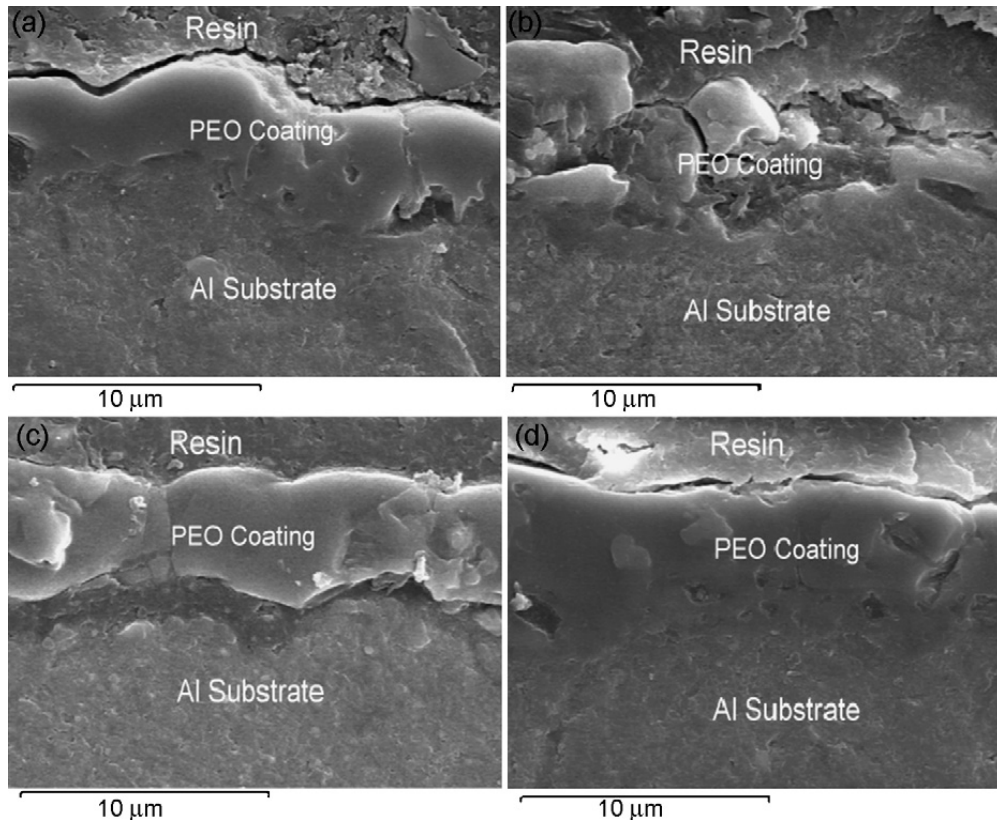


Figure 4.3: SEM micrographs of the cross-section of the MAO coatings treated (a) in E1 electrolyte, (b) in E1 electrolyte, (c) first in E1 electrolyte then in E2, (d) first in E2 electrolyte then in E1 [17].

As for the phosphate solution systems, more energy and time are needed to open the bonds between molecules since sodium hexametaphosphate is a kind of cyclic polymer. Therefore, for the phosphate solutions system the voltage is higher than that of silicate solution system. High and concentrative energy input resulting in violent discharges causes forming of more microcracks found in phosphate system. High and concentrative energy input also results in more and bigger discharge channels on the surface of the ceramic coatings formed in phosphate solution system [17].

Lv et al. [31], studied the MAO process in four different electrolytes in order to understand growth mechanism of the MAO coatings. Pure aluminum specimens were oxidized two kind of electrolytes which containing 0,005 M NaOH, 0,033 M Na_2SiO_3 and 0,025 M NaOH, 0,008 M $(\text{NaPO}_3)_6$. Voltage-time behaviors were recorded, as seen in Figure 4.4. In the first stage of the study the samples were oxidized in above mentioned electrolytes for 30 minutes, then in the second stage another two samples treated sequentially in the other solutions for another 30 minutes.

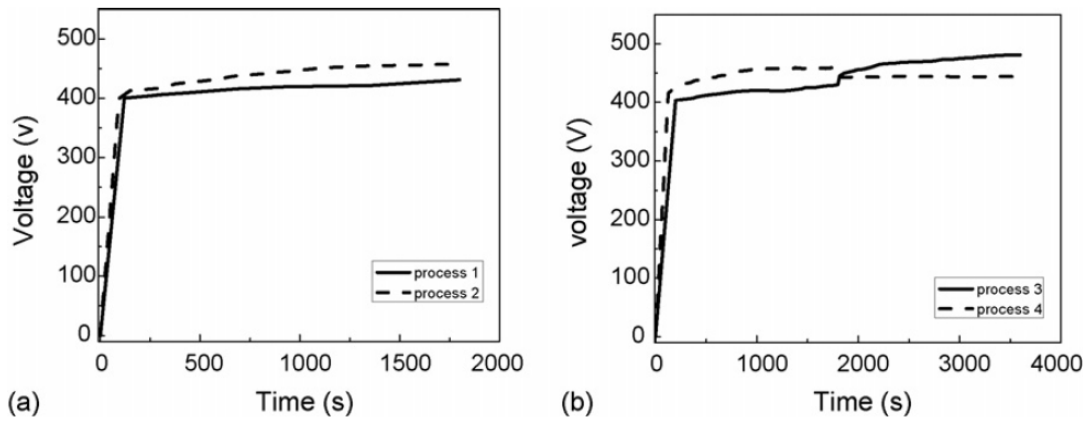


Figure 4.4: Voltage-time responses for anodizing aluminum (a) in processes 1 and 2, (b) in processes 3 and 4 [31].

Voltage-time responses of samples as exhibited in Figure 4.4, indicate that discharging voltage in phosphate electrolyte is higher than that in silicate electrolyte system [31].

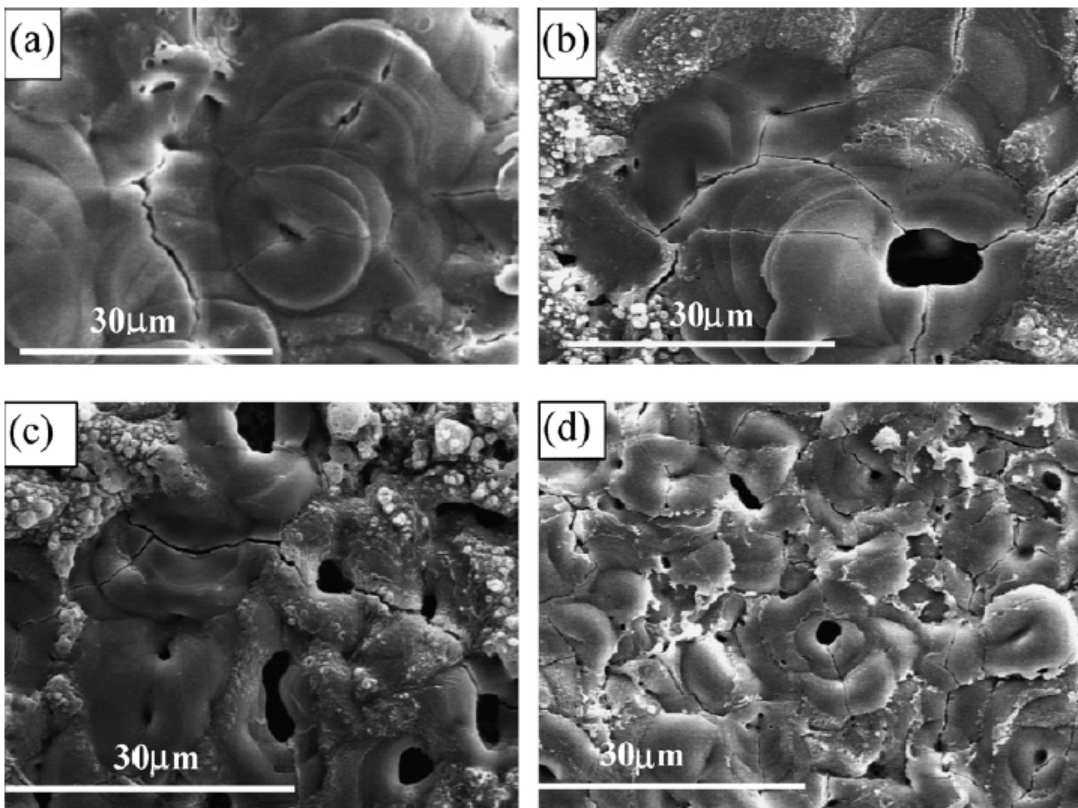
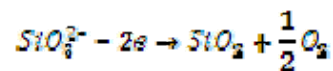


Figure 4.5: SEM images of surface of the MAO coatings produced in: (a) process 1, (b) process (b), (c) process 3, (d) process 4 [31].

Surface morphology of the MAO treated samples are presented in Figure 4.5. As indicated in Figure 4.5, the discharging voltage is higher in phosphate system than in silicate system. Therefore the number of discharges is larger and a large amount of melted materials sputtered out to form larger pores and pan-like structures. In a similar way, pores formed in the process 1, were enlarged after oxidized in phosphate system for another 30 minutes, on the contrary those treated in process 2 were diminished after oxidizing in silicate solution [31].

The phase of Mullite ($3\text{Al}_2\text{O}_3 \cdot 2\text{SiO}_2$) is a ceramic material having good thermal and chemical stability. The melting point of Mullite is 1810°C and has an orthorhombic crystal lattice. Besides, the incorporation of SiO_3^{2-} ions into the ceramic structures enhances the growth rate and improves tribological characteristics of the MAO coatings. Using an electrolyte containing Na_2SiO_3 , silicon oxide can be incorporated into formed MAO structure [8, 18]. Xin et al. [8], performed the MAO coatings in $20 \text{ gl}^{-1} \text{ Na}_2\text{SiO}_3$ and $2 \text{ gl}^{-1} \text{ KOH}$ solution then examined the incorporation and formation of silicon ions in oxide coatings during the process. Figure 4.6 indicates the XRD spectra of the coating surface and inner layer at different distance from the coating-substrate interface. Figure 4.6, indicates us the silicate ions in electrolyte take part in the formation of the coating. In addition, the peaks belonging to the Mullite indicates us that the content of the Mullite phase decreases continually along the coating thickness. Nevertheless, the Mullite phase disappears at $60 \mu\text{m}$ depth from the interface. Moreover, the content of amorphous structure decreases and the content of $\alpha\text{-Al}_2\text{O}_3$ increases along the coating thickness. The silicon element in Mullite phase comes from electrolyte containing the additive of Na_2SiO_3 . During the MAO process, on the surface of specimen following reaction, which SiO_3 anions take part, occurs;



According to XRD tests performed at different depths, it can be inferred that SiO_3^{2-} anion could not enter into interior of the discharge channel. . The formation of Mullite is quite complex, plasma thermochemical and electrochemical reactions occur during discharge process to form Mullite. Silicate ions move towards coating surface then by means of electrochemical reactions silicon oxide forms on surface. The high temperature due to plasma discharge generation can form Mullite phase by making silicon oxide diffuse into metastable $\gamma\text{-Al}_2\text{O}_3$ in the melting condition [8].

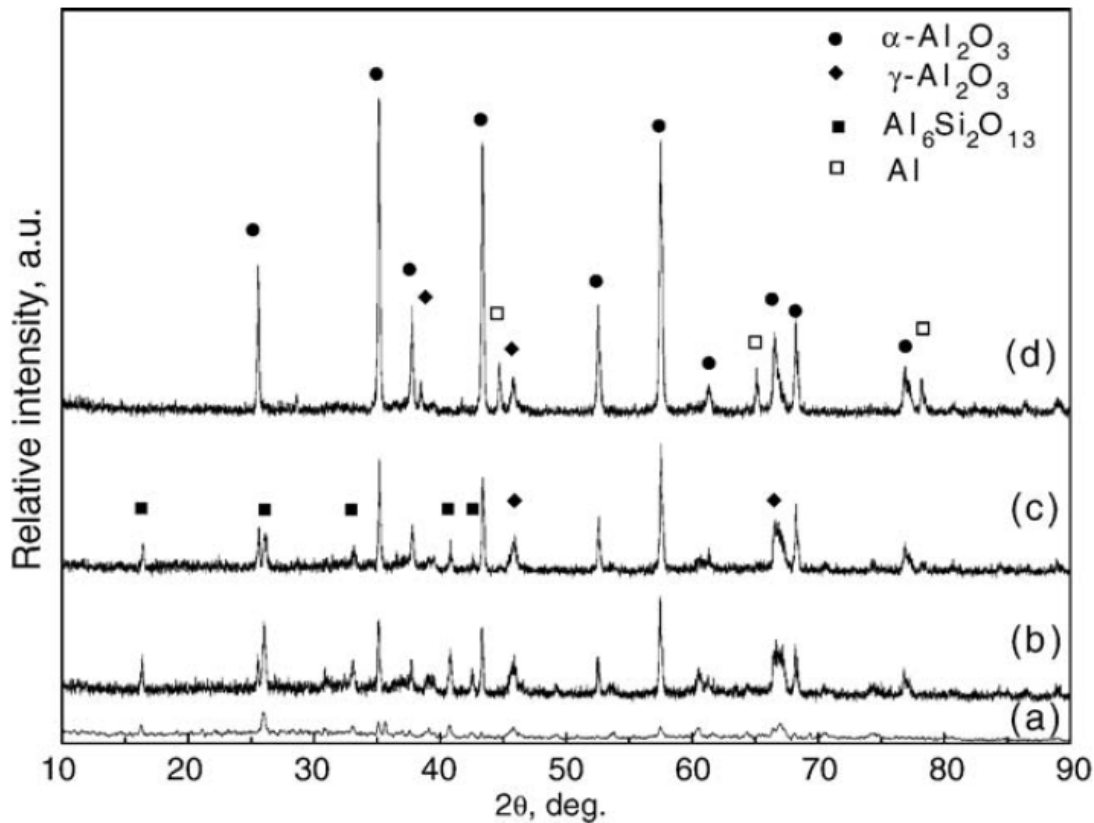


Figure 4.6: The XRD spectra of the (a) coating surface, and inner layers at different distance from the interface (b) 120 μm , (c) 90 μm , (d) 60 μm [8].

The diffusion process of SiO_3^{2-} anions can be also proved by EPMA results performed on cross-section of coating as seen in Figure 4.7 [8].

The results of the cross-sectional EPMA of the coatings show element silicon in inner layer of the coating is very little and is rich in outer layer of the coating. The Mullite phase forms mainly in the outer layer of the coating. Additionally, it must be noted that the content of the element silicon strongly depends on presence of the pores of the outer layer corresponding to the peaks in line scan profile of element silicon [8].

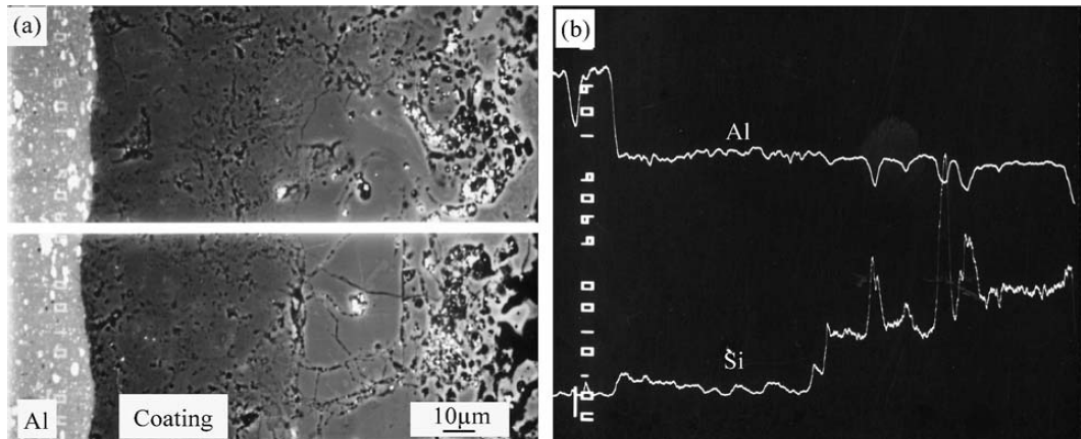


Figure 4.7: The cross-sectional EPMA results of the MAO coating: (a) the back scattering electron image of the coating; (b) the change of element concentrations along coating thickness [8].

Oxide layers obtained by processing of aluminum have excellent mechanical properties such as high hardness, well adhering to substrate, wear-resistance, high thickness and so forth [32, 33]. These properties are closely related to the phase composition and microstructure of the MAO coatings. In term of microstructure, the porosity of the MAO coatings is very important [34]. Curran et al. [35], studied porosity and pore architecture of exhibited by the MAO coatings. They investigated systemically the pore content, architecture and scale of the MAO coatings formed on 6082 aluminum alloy.

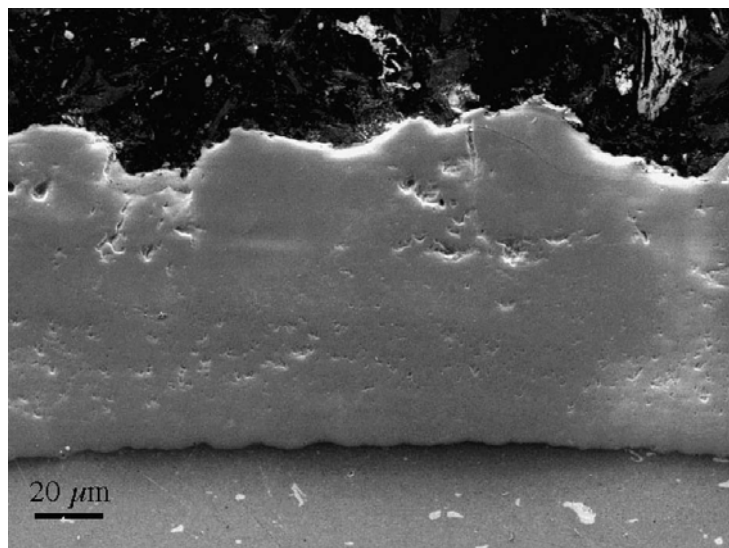


Figure 4.8: SEM image (secondary electron mode) of a polished section from a MAO coating [35].

Figure 4.8 shows a cross-section of a polished section from a MAO coating. Image analysis of such sections revealed that the porosity contents of such polished sections are below 3%. In Figure 4.9, pipe-like structures attributed to residual cores left by electrical discharges can be revealed better since back scattered electrons are able to show sub-surfaces thereby making it hard to be seen polishing artifacts. The fine network of channels created by discharges can be seen also in Figure 4.9. Nevertheless, the overall porosity still seems to be 5% [35].

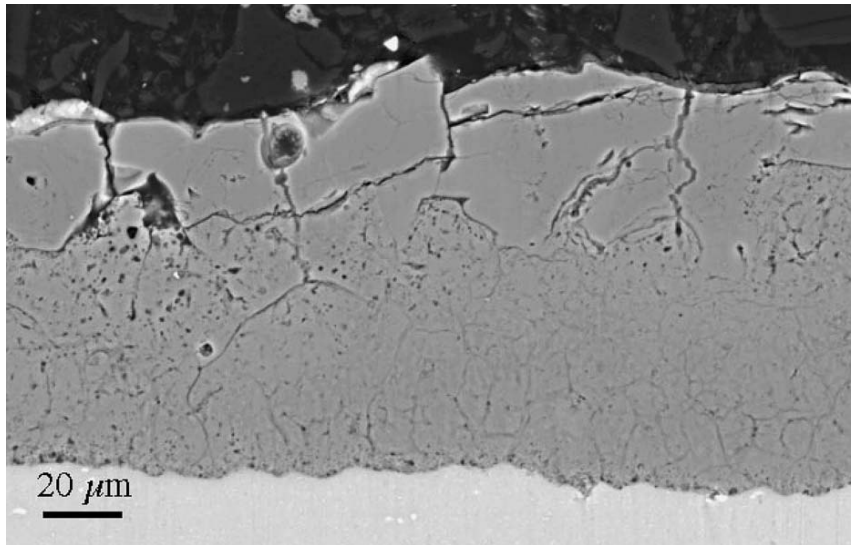


Figure 4.9: SEM image (back-scattered electron mode) of a polished section from a MAO coating [35].

However, examination of coating surface using a field emission gun at high magnification in Figure 4.10 shows the presence of extensive, interconnected, fine-scale porosity. Low-magnification image shows a network of fine, surface-connected pores. High-magnification image shows fine pore structures which cannot be seen in polished sections since it is very easy to deform or fill them during preparation [35].

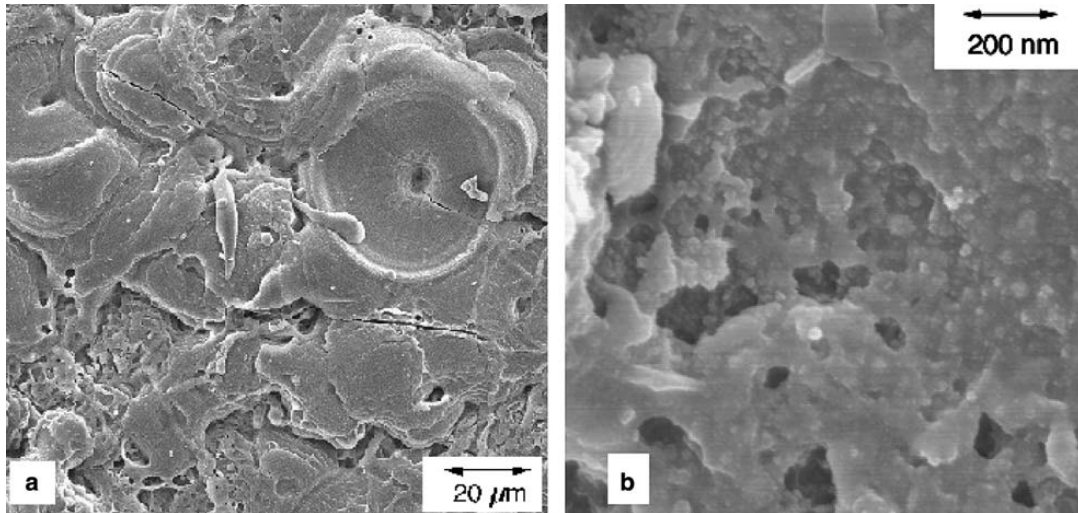


Figure 4.10: (a) low-magnification (b) high magnification SEM images (secondary electron mode) of the MAO coating surfaces [35].

The theoretical density of the MAO coatings was calculated from the proportion of the phases present and their densities. Measurements of the phase proportion obtained by means of X-ray diffraction. Calculated density data are presented in Table 4.2 and the densities were taken from previous publications. Theoretical density of the MAO coating was estimated as $3,63 \text{ g.cm}^{-3}$ [35].

Table 4.2: Phase density data and estimated density of the MAO coating [35].

Phase	Density (g cm^{-3})	Estimated phase fraction in coating (vol.%)	Calculated density (g cm^{-3})
$\alpha\text{-Al}_2\text{O}_3$	$3,987 \pm 0,024$	35 ± 10	-
$\gamma\text{-Al}_2\text{O}_3$	$3,72 \pm 0,1$	35 ± 10	-
Amorphous Al_2O_3	$3,1 \pm 0,1$	30 ± 10	-
PEO coating	-	-	$3,63 \pm 0,2$

Skeletal densities of the MAO coatings were also measured using penetrating fluids: C11F20 liquid in the case of Archimedian density measurements, helium gas in the case of pycnometry and mercury liquid under high pressure in the case of porosimetry. The results of these measurements were summarized in Table 4.3 [35].

Table 4.3: Experimental data for measured skeletal densities of the MAO coatings [35].

Method	Measured density (g cm ⁻³)
Archimedian weighing	3,73±0,02
Helium pycnometry	3,498±0,004
Mercury porosimetry	3,609±0,004

It is reported that at the early beginning of the MAO treatment, the MAO process works as a conventional electrolysis. As far as the aluminum oxide layer grows, the layer becomes more and more insulating. When the amplitude of the applied voltage is high enough, it will break down the growing oxide film leading to spark formation distributed randomly all over the aluminum surface [26, 36]. During the MAO treatment, the plasma color and brightness develop as a result of changes in the plasma characteristics (in particular temperature and density) and in the plasma composition. To study in detail these plasma characteristics can allow a better understanding of the process and growth process. Henrion et al. [37], studied growth mechanisms of the discharges during the MAO process for different current densities by means of electron microscope (SEM). The MAO process was performed in KOH and Na₂SiO₃ solution at 100 Hz, on 2214-T6 alloy.

Change of layer thickness with treatment time for different current densities is presented in Figure 4.11. The coating thickness of oxide coatings follows a linear kinetics for short treatment times while for longer treatment times departs from the linear behavior. The duration of the linear regime decreases with increasing the applied current density. Due to the oxide layer breakdown, discharge channel are created then molten aluminum gets oxidized when flowing out through these discharge channels. By this way, formed alumina contributes to the coating getting thicker by being ejected out from the channels and rapidly cooled at the surface-electrolyte interface. Therefore it can be inferred that the growth rate remains at a constant value as long as the spark channels reach the metal surface, in other words as long as the layer formation is an interface controlled process. For short oxidation times, the oxide layers exhibits inhomogeneous structure, rather thin, discontinuous structure with some porosities or empty holes can be observed by means of SEM.

Nevertheless, thick, dense, homogeneous and fairly smooth metal-oxide interface was observed for longer treatment times [37].

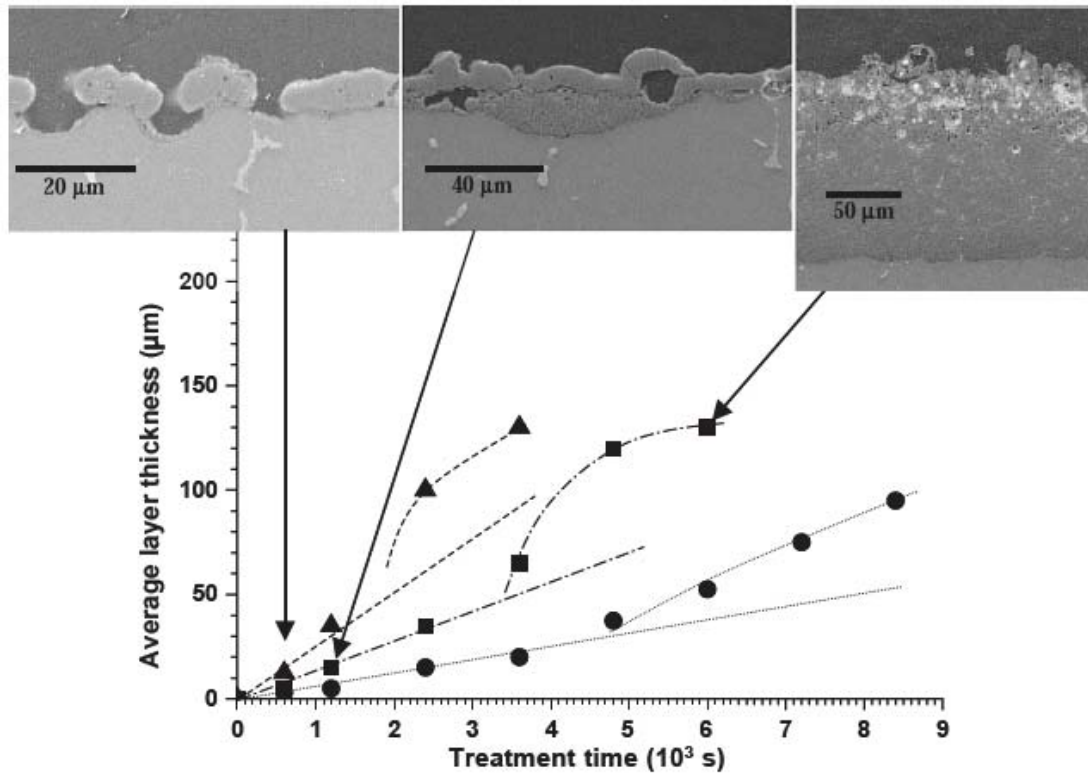
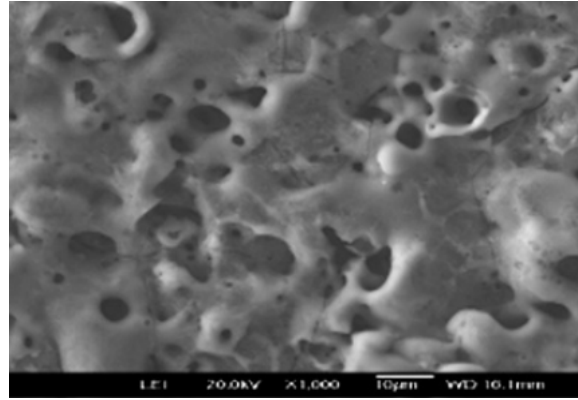


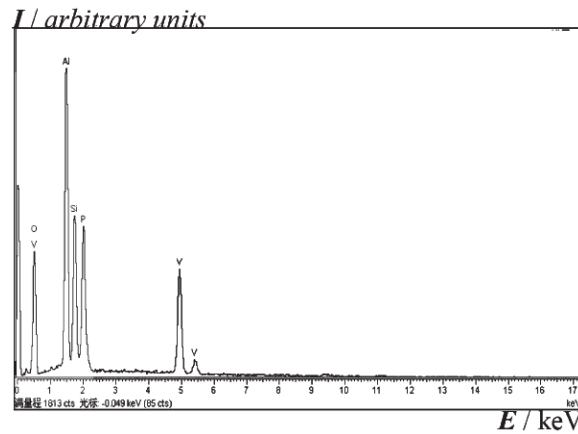
Figure 4.11: Change of layer thickness with treatment time for different current densities (a) 0,18 A/cm² (b) 0,38 A/cm² (c) 0,75 A/cm² [37].

Aluminum alloys can be micro arc oxidized in many kinds of solutions such as phosphate, silicate, carbonate, aluminate, borate etc. Though oxide layer obtained mainly composed of oxide layer, the microstructure, composition and property of this ceramic layer can be modified by adding small quantity of additives into the solution [27].

Li et al. [27], obtained black ceramic layers on aluminum alloy surface by introducing 6g/L ammonium metavanadate (NH₄VO₃) into NaPO₃ and Na₂SiO₃ solution.



(a)



(b)

Figure 4.12: (a) SEM image and (b) EDS spectra of ceramic layer treated for 15 min [27].

As seen from the Figure 4.12, a typical porous and rough MAO surface morphology obtained by means of the MAO. Moreover EDS analyses proved the absence of V in the MAO oxidized ceramic structure. Therefore, black ceramic layer obtained through the MAO process by adding 6g/L ammonium metavanadate (NH_4VO_3) into NaPO_3 and Na_2SiO_3 solution [27].

The surface properties of aluminum such as the wear resistance, corrosion resistance, high temperature shock, electronic insulation, etc. can be improved by means of the MAO. However, coatings obtained through the MAO process have higher friction coefficient sliding against steel or ceramic counterpart and lead to severe wear of the counterpart. Graphite, which is one of the allotropes of carbon element, has excellent wear reducing and lubricating properties. Thus, introducing of graphite into solution thereby entrapping them in the coating can improve the wear properties of the MAO

coatings. Wu et al. [38], studied self-lubricative coating on aluminum alloys in the solution of sodium aluminate and different concentrations of graphite.

From the SEM images which was observed in secondary electron mode in Figure 4.13, reveal that the density of the discharge channels decreases and the diameter of the discharge channels reduces remarkably as well with graphite additions [38].

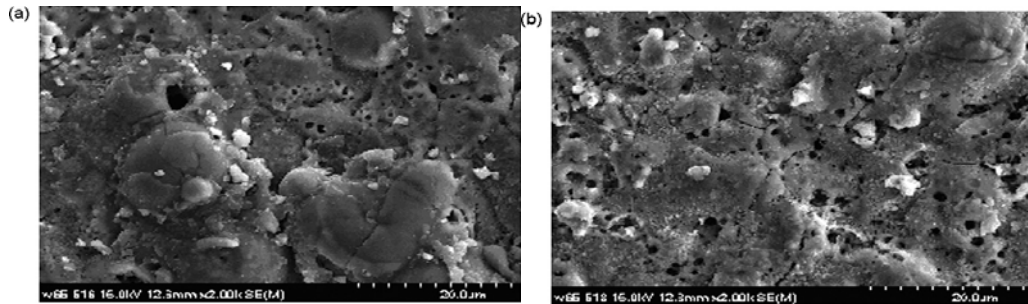


Figure 4.13: SEM images of the MAO coatings surfaces at 2000x magnification processed (a) pure Al_2O_3 , (b) doped Al_2O_3 [38].

EDS analysis as seen in Figure 4.14 indicates the presence of carbon element in the ceramic coating [38].

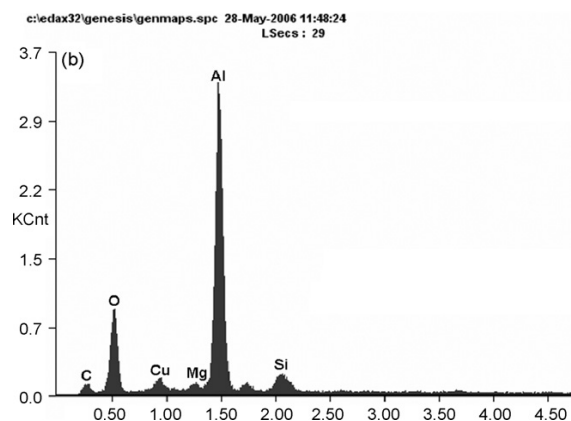


Figure 4.14: EDS analyses of the doped Al_2O_3 [38].

The surface properties of the MAO coatings influence mechanical properties of the MAO coatings such as tribological and corrosion resistance. The porous structure of the MAO coatings is a disadvantage for corresponding mechanical properties. Thus it is great interest to reduce porosity so as to improve surface properties. Lv et al. [39], studied corrosion and morphology of the MAO coatings treated in a solution consisting of Na_2SiO_3 , NaOH and graphite with different size of grains at a density of 5 g/l.

Four different solutions without and with different size of graphite grains (70 μm , 30 μm , 10 μm), respectively denoted as C1, C2, C3, were prepared and the coatings treated in those solutions were named coating-0, coating-1, coating-2, coating-3. Figure 4.15 shows SEM images of the MAO coatings with and without graphite additives. Closer examination revealed that the porosity decrease with decreasing of average size of graphite grains. Moreover, coating-3 seem the densest. Therefore, it is clear that the size of graphite grains has an effect on the morphology of the MAO coatings. It can be explained by being easier to diffuse for finer graphite grains into the coatings [39].

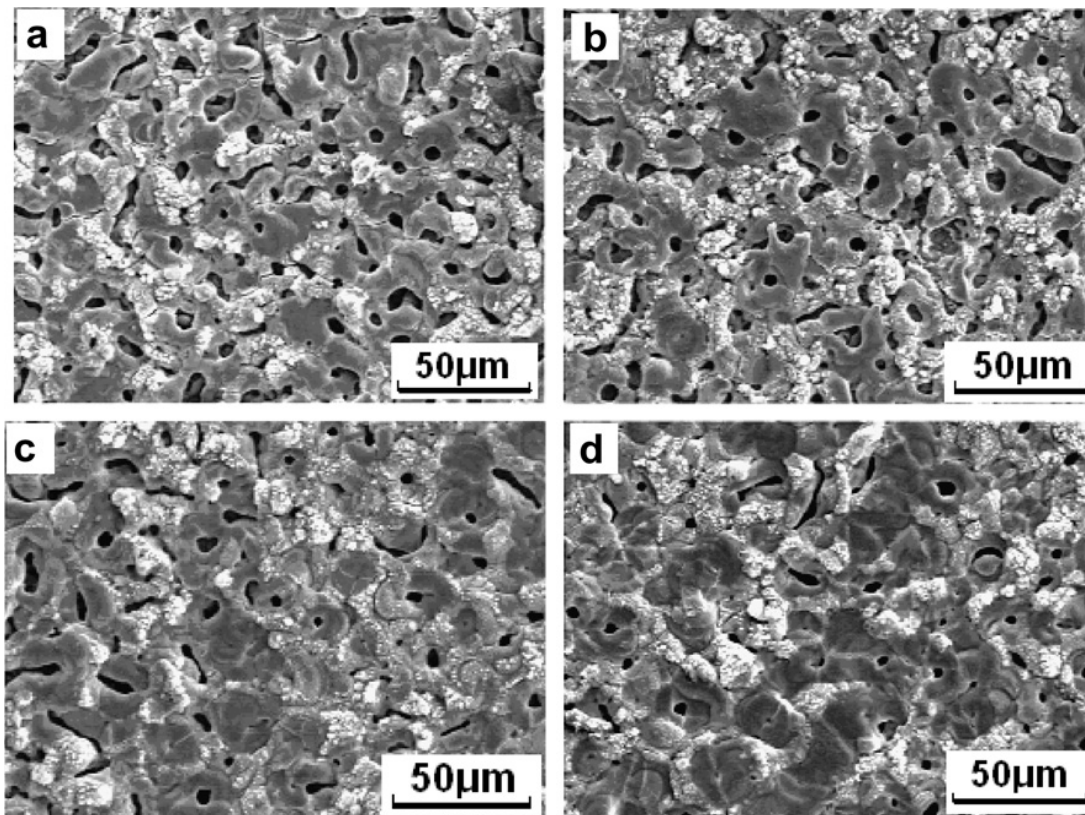


Figure 4.15: Surface morphology of (a) coating-0, (b) coating-1, (c) coating-2 and (d) coating-3 [39].

4.2 Wear Behavior

The MAO process is generally compared to hard anodizing. Hard anodizing is a technique which is capable of improving surface properties such as corrosion resistance, abrasion, thermal and dielectric properties and so on by forming an oxide structure on substrate material. Sundararajan et al. [40], studied tribological behavior of the MAO coatings formed on 6061 alloy by comparing to hard anodized ones.

Tribological performances of the samples were evaluated by conducting a dry-sand rubber wheel abrasive wear test at different normal loads. It was obtained that at lower normal loads like 1N, the wear rate of the MAO coatings is a factor of 12 lower than that of 6061 alloy, while the wear rate of hard anodized coating is lower by a factor 2 as compared to 6061 alloy. On the other hand, at higher normal loads, for instance at 50N, the abrasive wear rate of the MAO coatings is a factor 30 lower than that of 6061 alloy while hard-anodized coatings cannot stand such higher loads [40].

Wei et al. [1], performed wear tests of 2024 Al alloys on ring-on-block tester under both dry- and oil- lubricated conditions using steel ring and aluminum ring covered with the MAO coating as the counter parts. Excellent wear resistance and load-carrying capacity of the MAO coatings was observed. The friction coefficient and the wear rate of the MAO coatings under oil-lubricated conditions were reduced by one order and three orders of magnitude respectively compared to those of under dry conditions. Moreover, oxide coating could endure a sliding distance above 18,7 km under oil-lubricated condition against both the steel and ceramic rings at a load of 1400N [1].

Lots of machine parts, are not used in dry condition. Since the MAO coatings has surface connected and sub-micrometer porosity, it is beneficial to obtain low friction and good wear resistance on the MAO coated materials under lubrication condition. Zhou et al. [3], studied the influence of ambient environment on the wear mechanism of the MAO Al_2O_3 coatings using ball-on-flat apparatus imposed in the range of 5-10N in water and oil lubricated conditions as well as dry condition against Si_3N_4 ball. In dry condition, abrasive wear mechanism was observed as Si_2N_4 ball peeled off outer layer via ploughing the outer layer and microfracturing the internal hard layer. But in water lubricated condition, forming of lubrication gels such as $\text{Al}(\text{OH})_3$ or $\text{Si}(\text{OH})_4$ between tribo-pairs that reduces friction coefficient was reported. Thus, the wear mechanism was mix wear of mechanical and tribomechanical wear under water lubricated condition. The presence of porosity on coating surface served either as a micro-hydrodynamic bearing, a micro-reservoir for lubricant, or a micro trap for wear debris during wear process. Thus lower friction and wear in oil were obtained and the mechanism was microploughing wear in oil [3].

As mentioned in the previous chapter, additives have influence on wear resistance of the MAO coatings. The study of the Wu et al [38] showed that the friction coefficient of the MAO coatings decreased when the graphite is added to solution. Figure 4.16 shows the friction coefficient change of the coatings with different concentrations of graphite. During the sliding against the Si_3N_4 ball, friction coefficient maintains a constant value of 0,009. The friction coefficient reaches its minimum value when the concentration of the graphite is 4 g/l and then contrarily increases with the increase of graphite concentration [38].

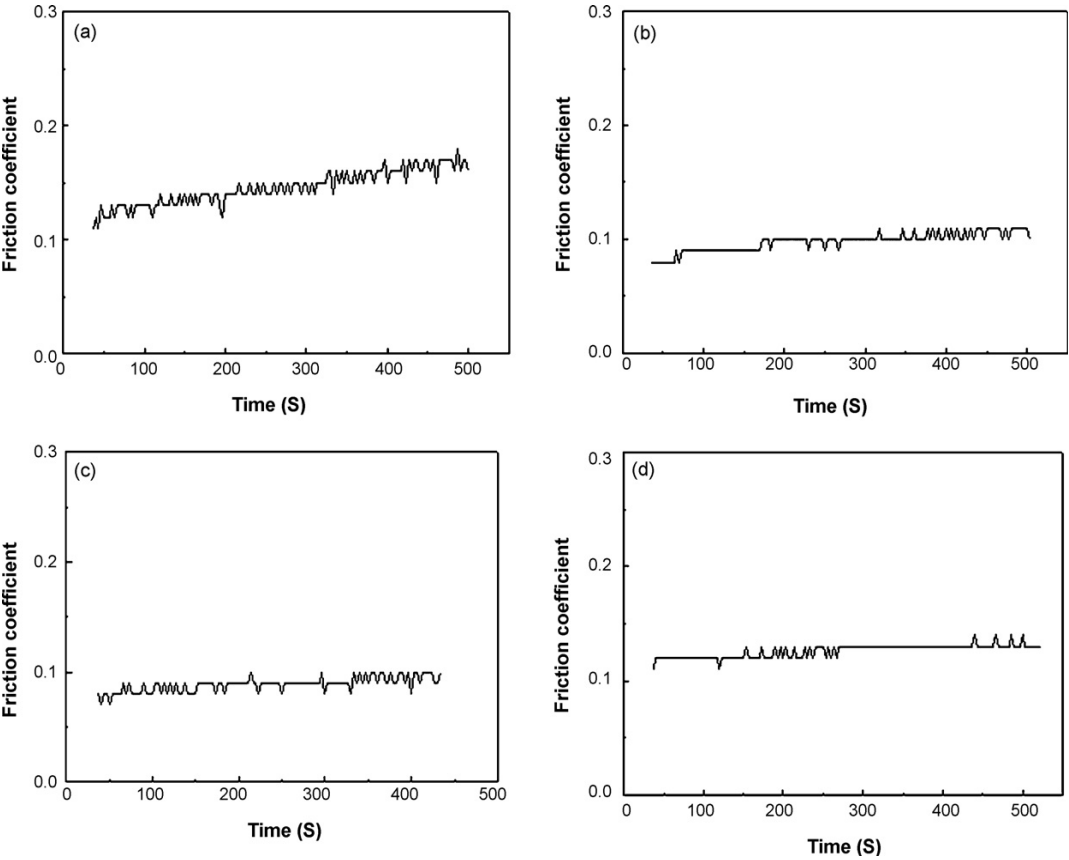


Figure 4.16: Friction coefficient of the coating with different concentrations of graphite (a) 0 g/l, (b) 2 g/l, (c) 4 g/l, (d) 8 g/l [38].

4.3 Corrosion Resistance Studies

Copper containing and zinc containing aluminum alloys are widely used in aerospace, automotive, textile engineering, etc. But the strengthening phases such as MgZn_2 , $\text{Al}_2\text{Mg}_3\text{Zn}_3$, Al_3CuMg , makes Al-Zn-Mg-Cu alloys susceptible to localized corrosion. Xue et al. [18], studied corrosion behaviors of the MAO films on Al-Zn-Mg-Cy alloy, namely hot rolled and age treated LC4 alloy. The polarization

measurements were performed in 3,5 wt.% NaCl solution at room temperature using saturated calomel electrode (SCE) as the reference electrode and platinum coil as the counter electrode. As shown in Figure 4.17, after the MAO treatment of LC4 alloy, corrosion potential increased and corrosion current density decreased significantly. Hence by means of the MAO process, corrosion resistance of LC4 aluminum alloy can be improved. As coating thickness increased, corrosion potentials of the micro arc oxidized samples, E_{corr} , moved to a more positive potential. This is mainly caused by the film thickness. The inner layer of the MAO film plays critical role on corrosion potential of LC4 alloy. Although corrosion potential of the MAO coatings move to a more positive potential with increasing the thickness, the corrosion current density i_{corr} , of the oxide films do not exhibit the same behavior. The worse corrosion resistance of the thicker oxide coatings may be related to influence of microcracks on the surface of the MAO film. During the spark formation, a few microcracks on the film surface will be generated due to thermal stress via rapid solidification of melt erupted from discharge channel. Hence, thicker coatings formed on LC4 alloy may lead worse corrosion resistance [18].

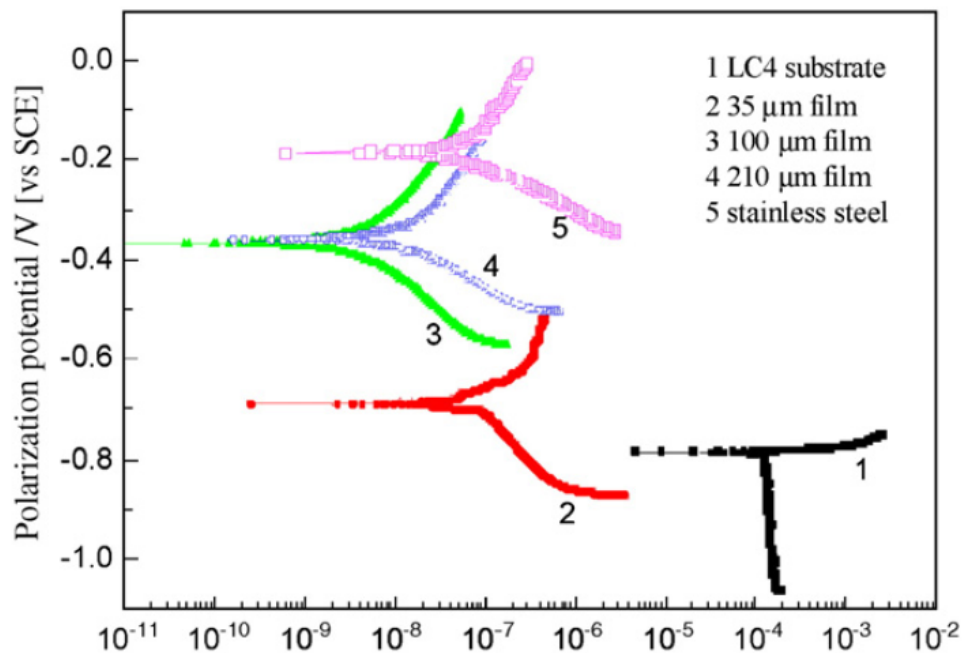


Figure 4.17: Potentiodynamic polarization curves of the bare and MAO coated samples with different film thickness [18].

As given the detail of the study of Lv et al. [39] previously, Since the graphite additives reduce the porosity, it is expected to enhance corrosion resistance of the

coatings. Polarization tests were performed in 3,5 wt% NaCl solutions. Figure 4.18 presents the potentiodynamic polarization plots for coatings. The polarization resistance determined from Stern-Geary equation based on the approximately linear polarization behavior near open-circuit potential. Table 4.4, summarizes the potentiodynamic polarization parameters. Especially in the anodic branch of the potentiodynamic polarization curves, different behaviors were observed. Coating-3 exhibited relatively higher Tafel slope than Coating-0 and Coating-1. Hence, one can say that coating-3 has less micro-defect and more compact structure which are benefit for suppressing the transfer of Cl^- ions during the corrosion. Corrosion current density (i_{corr}) is an important parameter to define capability of resisting to corrosion. Materials which have lower corrosion current density are more resistant to corrosion. The coating-3 has the lowest corrosion current density and the highest polarization resistance. This behavior of coating-3 which is also interpreted by Figure 4.15, can be attributed to corresponding surface morphology thereby smaller pore size and denser structure [39].

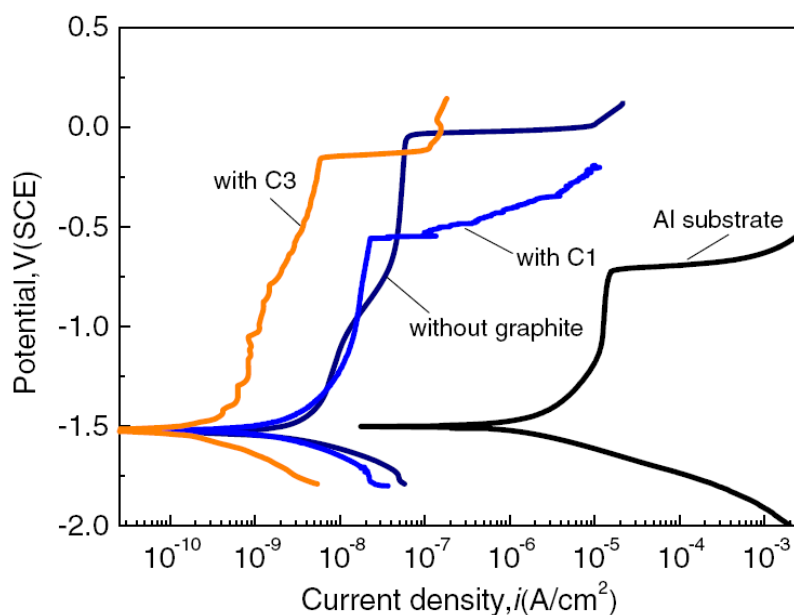


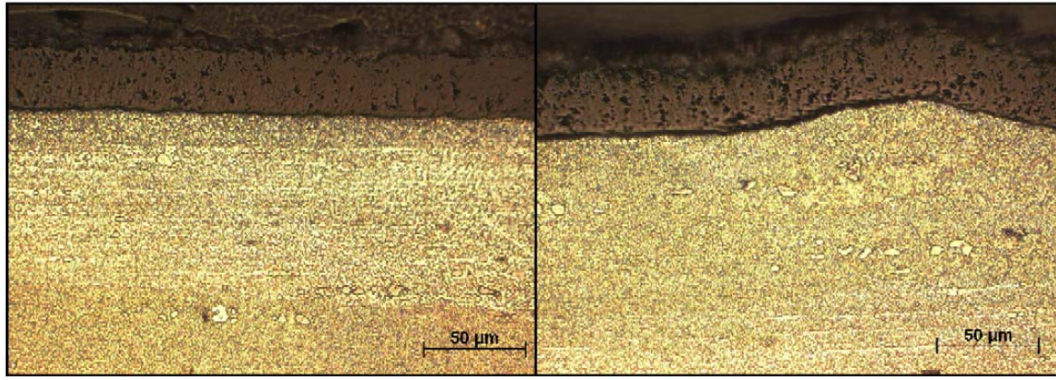
Figure 4.18: Potentiodynamic polarization curves of aluminum substrate and the MAO coatings [39].

Table 4.4: Results of the potentiodynamic corrosion tests [39].

Samples	b_a (mV)	b_c (mV)	E_{corr} (V)	R_p (Ωcm^2)	i_{corr} (A/cm^2)
Al substrate	296,3	136,26	-1,5016	23171	1,6226E-6
Coating-0	447,74	137,05	-15326	1,2565E7	3,2469E-9
Coating-1	391,9	201,07	-1,5203	1,068E7	5,0687E-9
Coating-3	396,81	207,65	-1,5192	1,8117E8	2,9618E-10

4.4 Fatigue Properties of the MAO Coatings

In some industrial areas, such as automotive and aerospace, materials are treated with cold working process, owing to being loaded repetitively during the service condition, in order to enhance their fatigue performance. In case of aluminum, they are shot-peened so as to increase these specifications. The shot-peening process inhibits short crack propagation and increase surface roughness which can be detrimental to fatigue performance. Though, the MAO process enhances surface properties fairly, such as wear performance, hardness, etc., fatigue strength deficit still remains [41, 42]. Therefore, using a combination of cold-working and hard coatings can provide improved fatigue performance as well as excellent surface properties. Asquith et al. [42], examined the change on fatigue performance of the MAO treated samples with shot peening process. The MAO process was performed on 2024-T351 aluminum alloys in Na_2SiO_3 and $\text{Na}_3\text{P}_2\text{O}_7$ solution. For the fatigue tests, they were evaluated in a configuration of four-point bending with a gauge volume length of 40 mm. Constant amplitude loading was applied with a stress ratio $R=0,1$ and the maximum stress values were between 250 and 400 MPa. Figure 4.19 (a), (b) show cross-sectional images of MAO coating on as received and shot-peened 2024 alloy which were mounted in the long-transverse orientation and etched in Keller's reagent to show microstructure. Besides, Figure 4.19, indicates the shot-peening induced plastic deformation which can be seen as a deviation of the copper rich regions from the straight formation. It also demonstrates that the dense layer on a shot-peened substrate has more porosity than that of an as-received substrate [42].

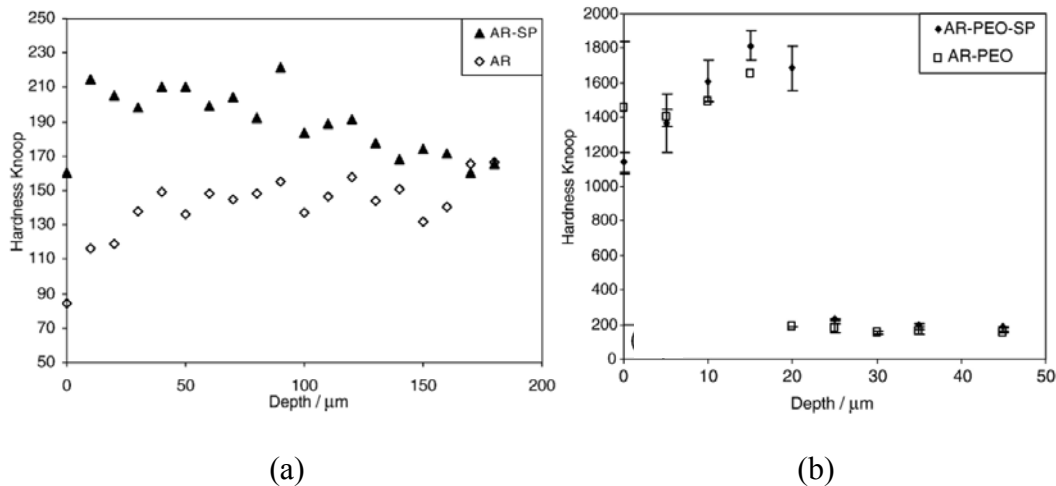


(a)

(b)

Figure 4.19: Optical micrographs of the MAO coatings on (a) as received and (b) shot-peened Al alloy substrates [42].

In Figure 4.20, the microhardness is plotted for the as-received and shot-peened samples showing enhancement of hardness by means of shot-peening process which could contribute to smoother hardness transition from the MAO coating to substrate. Figure 4.20, presents Knoop hardness of the MAO coated samples to show effect of shot-peening process across the MAO coatings. In comparison with unpeened specimen the transition through the coating-substrate interface for peened specimen is less abrupt and is harder due to initial hardening results from shot-peening [42].



(a)

(b)

Figure 4.20: Microhardness in as-received and shot-peened (a) aluminum substrate, (b) PEO coated specimens [42].

In Figure 4.21, a typical in-plane stress profile measured with synchrotron in shot-peened aluminum is presented. Results of stress measurements indicate that shot-peening process induces a maximum of 300 MPa compressive stress at the depth of around 150 μm from the free surface. Figure 4.22 presents stress profiles in PEO coatings on as-received and shot-peened specimens. Stress profiles take zero depth as

the interface region and progress towards the surface. Unfortunately the resolution of this technique is not better than ± 50 MPa; however the signs and magnitudes are a reasonable representation of the actual stress state present. The larger scatter in data presented in Figure 4.22, arises when examined volume contains porosity, inclusions or other features. Though this large scatter in the data, the stress profiles in PEO coating on as-received and shot-peened Al alloy substrate are fairly different. According to residual stress profiles, interface has a tensile stress and in the middle region a compression stress with maximum stress of 160 MPa was observed while the coating on shot-peened substrate has a compressive stress at the interface and tensile in the middle. This behavior is due to shot-peened aluminum has a region of compressive stress at the near surface as seen in Figure 4.21. The presence of residual stress might be responsible for fatigue benefits [42].

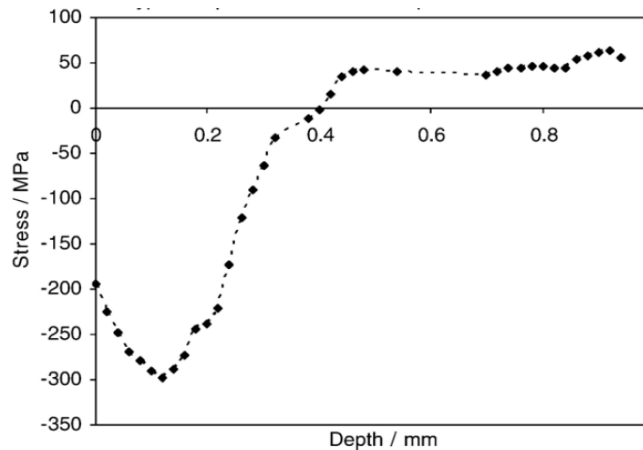


Figure 4.21: Typical residual stress profile for shot-peened aluminum [42].

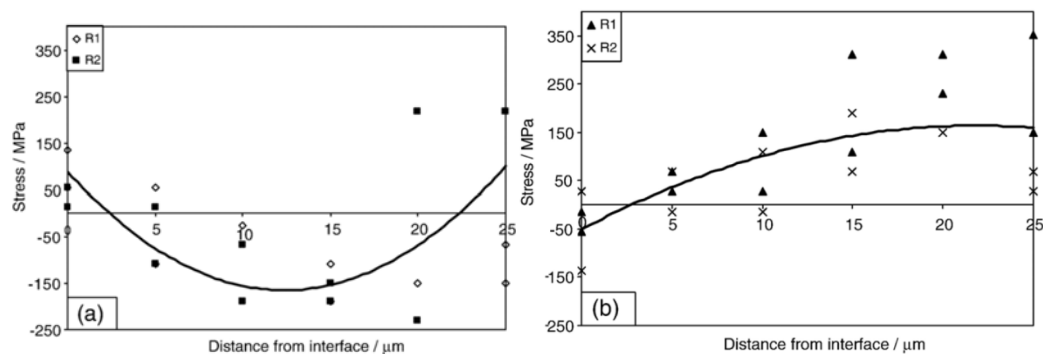


Figure 4.22: Residual stress profiles for the MAO coatings on (a) as-received, (b) shot-peened Al alloy substrates [42].

Stress vs. life curves (S-N curves) for the four different specimen types are presented in Figure 4.23. The curve for the MAO treated specimens is the lowest and the tensile residual stresses formed at coating-substrate interface due to coating process can explain this behavior as seen in Figure 4.22. Tensile residual stress regions are the most likely regions for crack initiation hence they will facilitate cracks to propagate and accelerate failure. Better service life can be attributed to residual stress at interface which can facilitate crack tip closure and slow growth rates thereby increasing the fatigue life. Moreover, decreasing the service life of shot-peened and coated samples can be explained with reduced interfacial compressive stress induced heterogeneity near the surface that acts as a surface defect allowing earlier crack initiation [42].

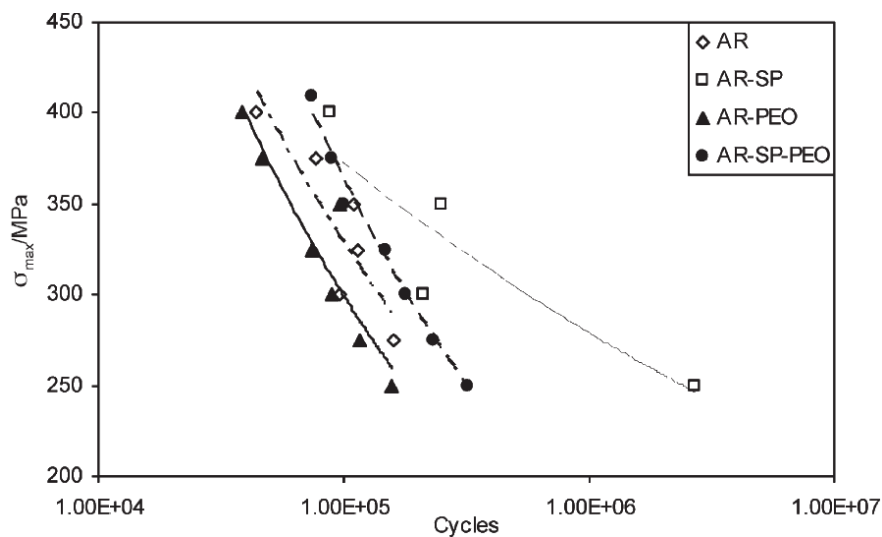


Figure 4.23: S-N curves for four different surface conditions [42].

4.5 Thermal Properties of the MAO coatings

Xin et al. [8], performed the MAO coatings in 20 gl^{-1} Na_2SiO_3 and 2 gl^{-1} KOH solution then performed thermal analysis of the MAO coating. Thermogravimetric plot and the DSC curve of the MAO coating are presented in Figure 4.24. The thermogravimetric plot indicates that there is only 1,5% mass loss in the temperature range from 50 to 1200°C. The DSC curve indicates that there is a weak exothermic peak at around 815°C which is the crystallization temperature of SiO_2 [8].

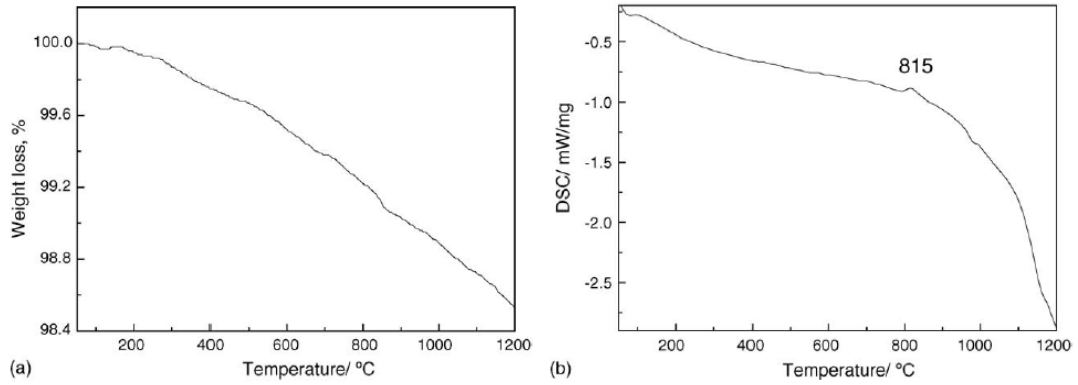


Figure 4.24: (a) TG and (b) DSC curves of the MAO coatings. Heating rate 10 Kmin^{-1} , specimen mass 30mg [8].

The measured thermal expansion of the MAO coating as a function of temperature from 50°C to 600°C is presented in Figure 4.25. the thermal expansion coefficient of the MAO coatings between these temperatures is $6,6 \times 10^{-6} \text{ K}^{-1}$ which is quite larger than that of Aluminum $24 \times 10^{-6} \text{ K}^{-1}$ and smaller than that of $\alpha\text{-Al}_2\text{O}_3$ $7,8 \times 10^{-6} \text{ K}^{-1}$. This is caused by forming of thermal stress between the substrate and coating during the thermal treatment [8].

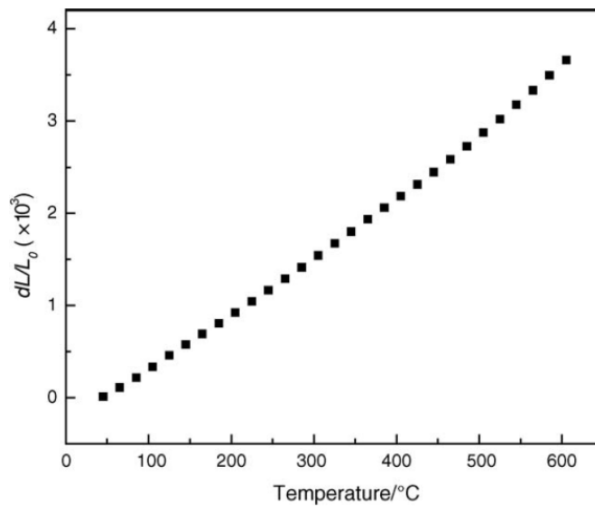


Figure 4.25: The thermal expansion of the MAO coatings [8].

4.6 Other properties of the MAO coatings

The properties and characteristic of the MAO coatings are mainly determined by the process parameters and the properties of the bulk materials, such as composition of the solution, current-voltage and current density behavior, solution temperature and

so forth. The net oxidation kinetics is probably determined by charges passing through the oxidized surface. Therefore, the current density which is related to the total charge passes through a unit sample surface area has an important role in the formation of the MAO coatings. Besides, the distribution of the anode current in the whole surface has a decisive effect on surface properties and the uniformity of the coating thickness. Tian et al. [21], studied anode current effects on wear and corrosion properties of the MAO coatings formed on Al by changing the distance between the electrodes and measuring the current passed through the both back and front surfaces. Figure 4.26, is an evidence that shows the anode current is influenced by the electrode location. Since the solution has a resistance, R_{sol} , as the distance between anode and cathode increases, the magnitude of R_{sol} increases thereby decreasing correspondingly anode current [21].

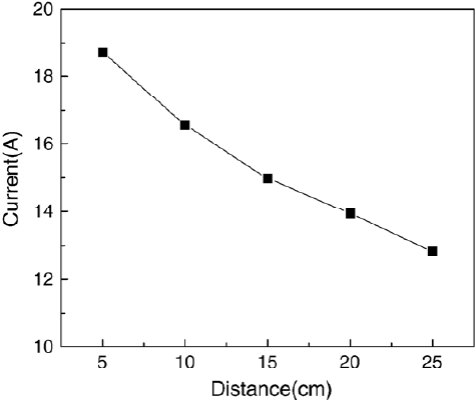


Figure 4.26: Dependence of anode currents on the distance between electrodes [21].

Measured waveforms of currents flowing through the front and back surfaces, depicted in Figure 4.27, revealed that the current flowing through the front surface is higher than that of back surface. This event called “shelter effect” of the front surface. This difference causes from flowing of anode current preferentially straight away while front surface directly sees cathode [21].

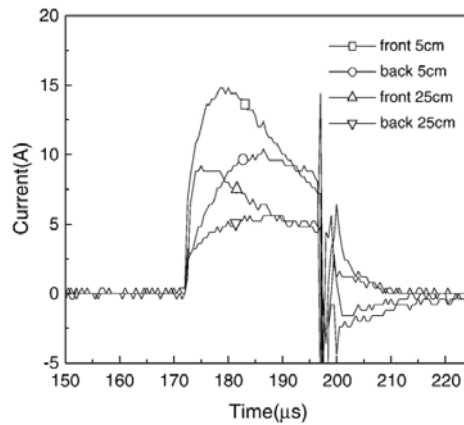


Figure 4.27: Waveform of currents flowing through the front and back surfaces [21]. Performed wear and corrosion tests also revealed the “shelter effect” of the front surfaces. As presented in Figure 4.28, the wear test results showed that breakthrough of oxide coating on the front surface could endure 2700s, which is about four times longer than that of back surface. This difference may be related to thicker coating formed on front surface and different phase composition due to large current density [21].

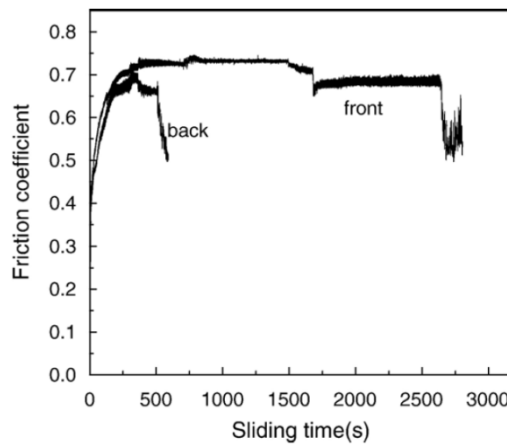


Figure 4.28: Friction coefficient on the front and back surfaces [21].

Figure 4.29 indicates the results of corrosion tests performed in 3,5% NaCl solution. Corrosion resistance of the untreated sample was considerably improved by means of the MAO process. The reason of front surfaces for having better corrosion resistance may be attributed to thicker coating formed at higher current density [21].

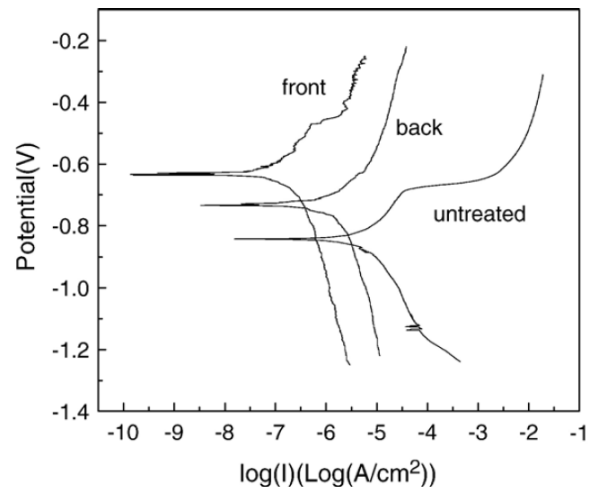


Figure 4.29: Potentiodynamic polarization curves obtained in 3,5% NaCl solution [21].

With the development of infrared detecting technologies the use of infrared adsorbers to confine active and passive infrared waves has become practical interest. Theoretical investigations have shown that a random rough surface can mitigate surface reflection. Thus, a material which has low emittance and rough surface topography may fulfill the requirements for the concealment of active and passive infrared waves. Jin et al. [43], studied the infrared reflection properties of the MAO coatings on aluminum substrates.

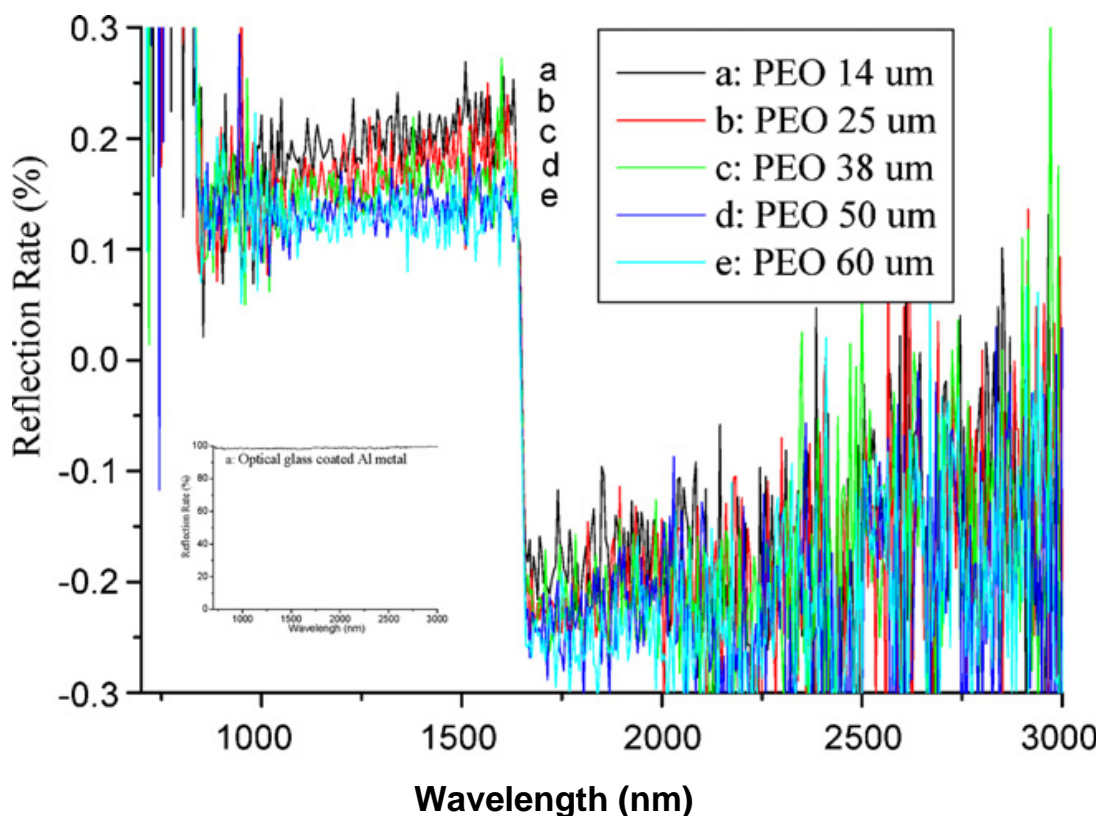


Figure 4.30: The reflection rate of infrared wave from 780nm to 3000nm determined from the glass coated aluminum alloy and the MAO coatings having the thickness of (a) 14 μm , (b) 25 μm , (c) 38 μm , (d) 50 μm , (e) 66 μm [43].

The reflection rates determined from the MAO coatings are shown in Figure 4.30. The reflection rate of glass coated aluminum was also given for comparison. The infrared reflection rates determined from 1650 nm to 3000 nm are almost the same for different MAO coatings while from 780 nm to 1650 nm the infrared reflection rates decrease with coating thickness. So, the MAO process provides a convenient porous and rough surface that bodes well for infrared adsorbers [43].

5. EXPERIMENTAL STUDIES

In this study, the micro arc oxidation process was performed on 7075 aluminum alloy in an aqueous solution of potassium hydroxide and sodium metasilicate and then the effect of the process parameters on the coating properties was investigated.

In the experiments, variation of mechanical properties of the coatings with various process parameters such as diverse currents, voltages and frequencies were studied. According to the results, appropriate process parameters for different applications were obtained. The following sections summarize details of the tests performed.

5.1 Sample Preparation

The rectangular specimens of 40mm x 10mm x 10 mm were cut from an ingot which was fabricated from 7075 Al alloy in T6 condition having a nominal composition as seen in Table 5.1. Then they were grounded up to 1200 grits with SiC papers gradually. Afterwards, they were cleaned with acetone and distilled water sequentially before the treatment process.

Table 5.1: Nominal chemical composition of 7075 aluminum alloy [44].

Alloying Element	Zn	Mg	Cu	Fe	Si	Mn	Ti	Al
Composition, wt%	5,1	2,1	1,2	0,5	0,4	0,3	0,2	rem.
	6,1	2,9	2,0					

5.2 The MAO Process

The MAO experiments were carried out using 30 kW MAO equipment which is able to adjust potential, current and frequency of power supply. The machine utilized for coating is presented in Figure 5.1. The Al alloy specimen and the wall of the stainless steel container were used as the anode and the cathode, respectively. The equipment

also consists of a ventilation system and a cooling unit which is employed for keeping the solution temperature below 35°C. The MAO equipment is capable of applying voltage or current in a square wave form as well as their durations as schematically seen in Figure 5.2.



Figure 5.1: Micro-arc oxidation apparatus

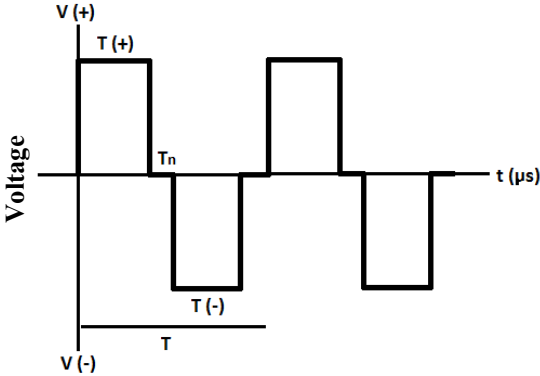


Figure 5.2: Applied voltage in square wave form

Samples were treated in an alkaline solution, containing 1g/l KOH and 3 g/l Na₂SiO₃. After the treatment, samples were rinsed with distilled water then dried with hot air. KOH added to solution in order to adjust the pH value to 12 [45]. Na₂SiO₃.is added to provide conductivity of the solution to necessary value, namely 9 mS/cm, for our contrivance.

The purpose of the study was to select appropriate way firstly, then to change pulse durations of the process parameters. In the first step of the study, two different methods, namely “constant voltage” and “constant current”, have been chosen in order to see the best way to proceed. For the constant voltage and constant current methods, samples were treated only for ten minutes. Six different voltages were used by keeping the voltages constant during the experiment for the method of “constant voltage”. Studied conditions for this method are summarized in Table 5.2.

Table 5.2: Processing conditions for the samples oxidized under voltage controlled mode.

Sample Code	Applied Voltage (V)		Applied Current (A)		Pulse Duration (µs)		
	Positive	Negative	Positive	Negative	Positive	Neutral	Negative
V1	500	100	Variable	Variable			
V2	500	200	Variable	Variable			
V3	400	100	Variable	Variable	5000	200	5000
V4	400	200	Variable	Variable			
V5	300	100	Variable	Variable			
V6	300	200	Variable	Variable			

For the method of “constant current”, six different constant current couples were studied by starting from 4 positive amperes and increasing up to 10 amperes. Studied properties and labels of specimens are summarized in Table 5.3.

In the second step of the study, the aim was to change pulse duration parameters of applied voltage. Therefore, according to results of both methods, “constant voltage”

way was chosen with the aim of choosing the best way. 500 positive and 150 negative voltages were applied to samples to study pulse duration effect on the MAO coating process.

In the MAO process, both negative and positive voltages were applied to samples in square form as seen in Figure 5.2. Hence, by changing the pulse durations of each applied voltages, the frequency of the process could be adjusted.

To study pulse duration effect on the MAO process, nine different pulse durations were chosen. Firstly, coating process got started from minimum negative voltage time, and then increased 1000 μ s for each sample. The same process was also applied for positive voltage time. The applied conditions are presented in Table 5.4.

Table 5.3: Processing conditions for the samples oxidized under current controlled mode.

Sample Code	Applied Voltage (V)		Applied Current (A)		Pulse Duration (μ s)		
	Positive	Negative	Positive	Negative	Positive	Neutral	Negative
I1	Variable	Variable	4	1			
I2	Variable	Variable	4	2			
I3	Variable	Variable	6	1			
I4	Variable	Variable	6	2	5000	200	5000
I5	Variable	Variable	10	1			
I6	Variable	Variable	10	2			

Table 5.4: Processing conditions for the samples oxidized for different pulse durations.

Sample Code	Applied Voltage (V)		Applied Current (A)		Pulse Duration (μ s)		
	Positive	Negative	Positive	Negative	Positive	Neutral	Negative
512	500	150	Variable	Variable	5000	200	1000
522	500	150	Variable	Variable	5000	200	2000
532	500	150	Variable	Variable	5000	200	3000
542	500	150	Variable	Variable	5000	200	4000
552	500	150	Variable	Variable	5000	200	5000
452	500	150	Variable	Variable	4000	200	5000
352	500	150	Variable	Variable	3000	200	5000

Characterization of the samples were carried out by macroscopic and microscopic examinations via optical microscope and scanning electron microscope (SEM), X-ray diffraction analysis, surface roughness measurements, wear experiments, and contact angle measurements.

5.3 Structural and Morphological Characterization

The surface morphologies of the coatings were examined by an SEM at different magnifications. The composition of the surface layer was analyzed with an energy dispersive spectroscope (EDS) attached in the SEM. Cross-sectional micrographs were examined by using a Leica optical microscope and the thicknesses of the coating layer was measured and eddy current thickness gauge. Qualitative phase analysis was made by an X-ray diffractometer (XRD, GBC-MMA) using $\text{CuK}\alpha$ radiation with a scan range between 20-100° at a step of 0.020°.

5.4 Hardness Tests

The micro hardness tests were performed using CSM or Shimadzu micro hardness tester from the cross-sections of the coatings under an indentation load of 50 g.

5.5 Wear Tests

The tribological performances of specimens, bare 7075 alloy and oxidized coatings, were evaluated by reciprocating type Tribotechnic tester using a 6 mm diameter alumina ball under a normal load of 5N, sliding speed of 5 mm/s. The stroke of the movement was 5 mm stroke and the total sliding distance was 45000 mm. The wear tests were evaluated in dry condition and at room temperature. The average surface roughness (Ra) and the depth and width of the wear tracks were measured by a Veeco Dectac 6M surface profilometer. Schematic representation of the depth and width of the wear tracks was given in Figure 5.3. The area of the wear tracks were calculated according to the Eq. 5.1.

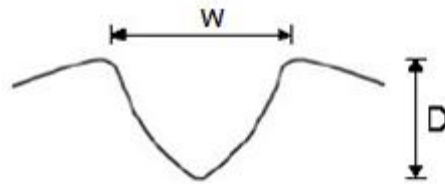


Figure 5.3: Schematic view of width and depth of the wear tracks

$$V = \frac{\pi}{4} L.W.D \quad (5.1)$$

V: Volume of the wear track

L: Length of the wear track (5 mm)

W: Width of the wear track

D: Depth of the wear track

5.6 Corrosion Tests

Bare 7075 alloy and eight of the MAO coated specimens were immersed in solution, consisting of 30g/l NaCl and 0,01M HCl, for 300 hours at room temperature. Samples were removed from the corrosive solution at every twenty four hours. They were weighed and the solution pH was measured and they were immersed again in the corrosive solution to continue the test.

6. RESULTS AND DISCUSSION

This section will be covered by dividing into two categories in order to analyze the first and the second part of the study separately.

6.1 The MAO Condition Parameters

General view of the samples treated under the conditions of “V1, V6, I1, and I6” are presented as the examples in Figure 6.1, the others are also submitted in “Appendix A”. As can be seen in Figure 6.1, higher voltages (V1) and lower current (I1) values produce darker surface appearance.

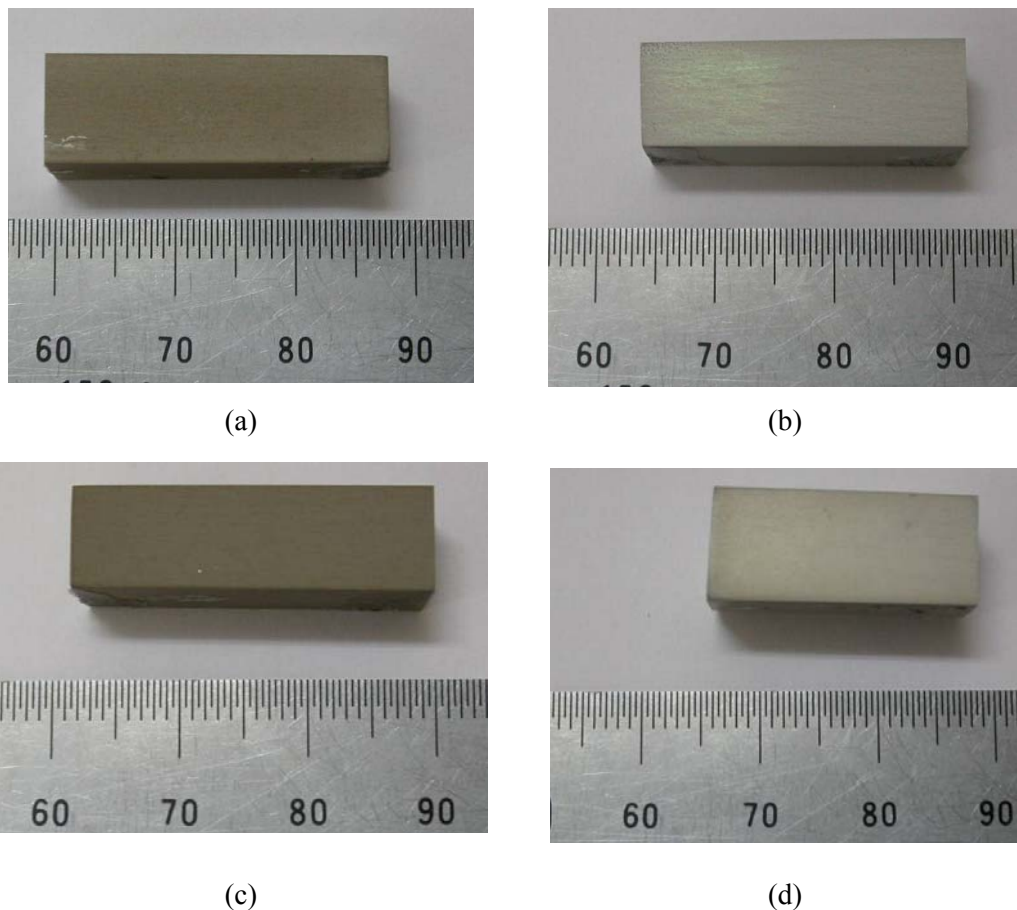


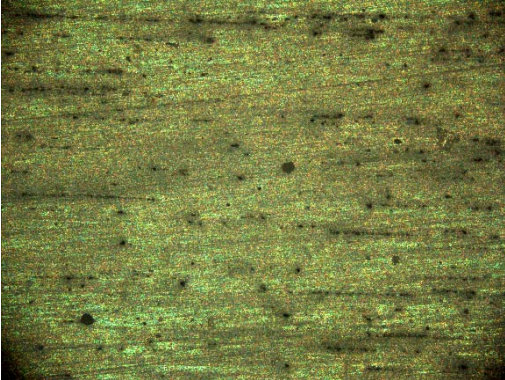
Figure 6.1: General view of the samples oxidized under constant voltage and constant current modes. (a) V1, (b) V6, (c) I1, (d) I6

Surface micrographs of the samples were presented in Figure 6.2. Surface appearance was uniform when the voltage level is higher (V1) as can be seen in Figure 6.2a, whereas, there are some marks coming from the grinding stages of the sample preparation and small isolated islands on the surface when the voltage level decreased. This indicates that voltage level (V2) is insufficient to produce a uniform coating layer at the surface (Figure 6.2b).

Surface micrographs of the samples oxidized in the current controlled mode were also consistent with macro photographs of the samples given in Figure 6.1. It can be stated that current controlled MAO process produces more uniform surface appearance regardless of the applied current level. The other surface and cross sectional micrographs are given in Appendix B and Appendix C respectively.



(a)



(b)



(c)



(d)

Figure 6.2: Surface micrographs of the samples treated under voltage controlled and current controlled modes (a) V1, (b) V6, (c) I1, (d) I6.

In Figure 6.3 and Figure 6.4, the bulk XRD patterns of the samples V1 and I1 are presented, respectively. Both XRD patterns revealed that surfaces comprise mostly gamma form of alumina with less amount of alpha form of alumina. It is also evident that there are some aluminum peaks coming from the substrate. Other XRD patterns are presented in Appendix E.

In the process of the MAO, the aluminum substrate is directly oxidized to become α and γ phases due to a high temperature sintering in the Micro arc zone. Alpha alumina, is the stable phase of aluminum oxide with a melting point of 2050°C and is characterized by a high hardness, second after diamond in Mohs hardness scale. Gamma is the metastable phase which can be transform into alpha by heating in the temperature range from 800°C to 1200°C [30].

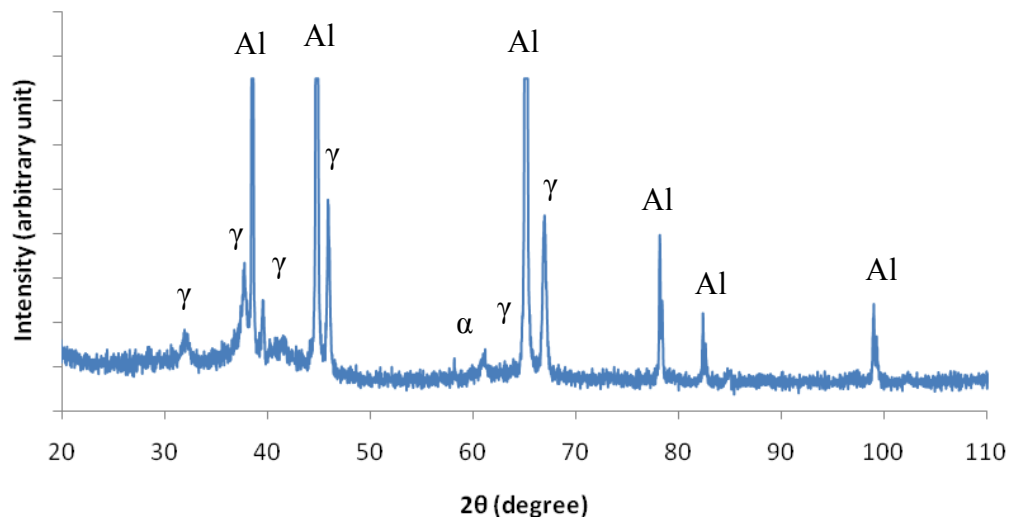


Figure 6.3: X-Ray diffraction patterns of the sample V1

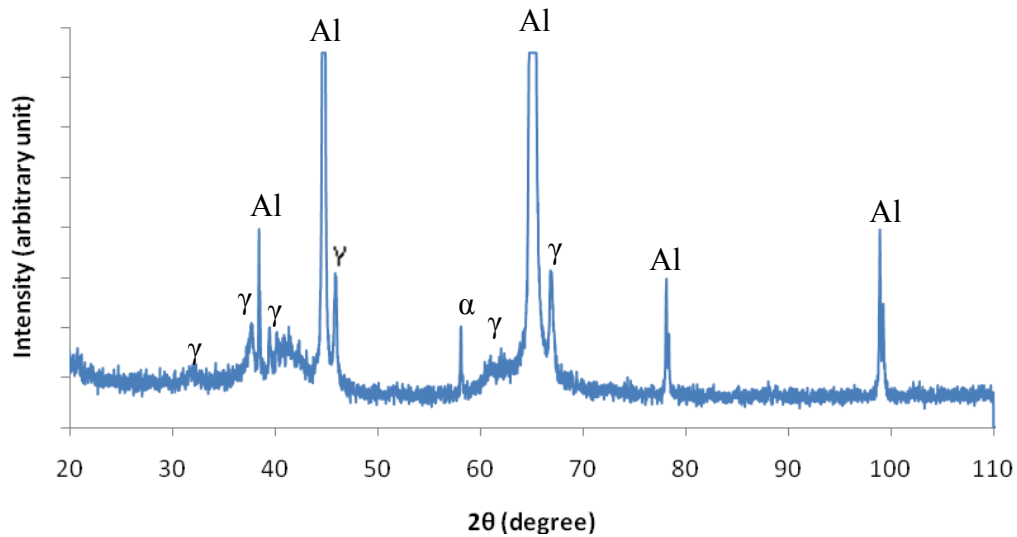


Figure 6.4: X-Ray diffraction patterns of the sample I1

Variation of thickness with applied voltage and current is presented in Figure 6.5 and Figure 6.6, respectively. As the applied voltage decrease, it was observed that coating thickness of the samples treated under constant voltage condition generally decreased. The thickest oxide coating with a thickness of 14,6 μm , belongs to the sample treated with V^+ : 500 V/ V^- : 200 V. One important issue in coating process under constant voltage mode was that the thickness of the samples treated with 200 V of negative voltage were slightly higher than those of treated with 100 V of negative voltage. Thickness of the coatings obtained under constant current mode is ranged between 1 - 6 μm .

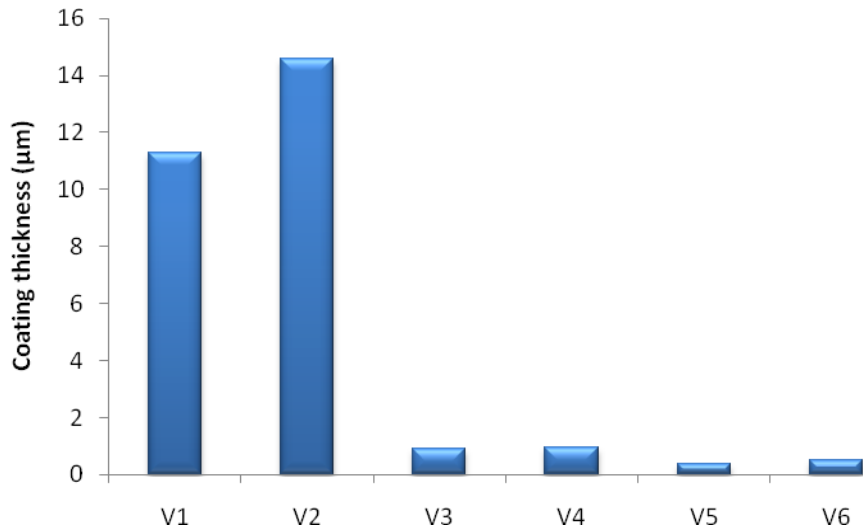


Figure 6.5: Coating thickness of voltage controlled samples

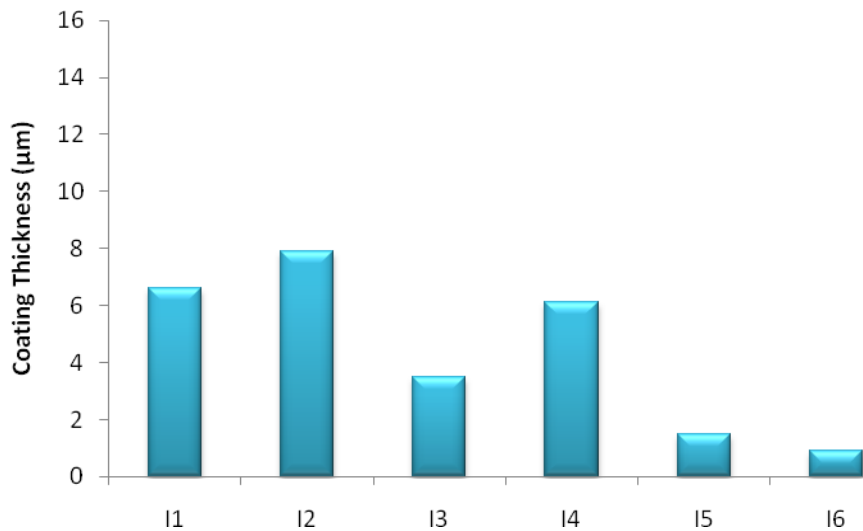


Figure 6.6: Coating thickness of current controlled samples

Average surface roughness of the oxide films is presented in Figure 6.7 and Figure 6.8 for constant voltage and constant current modes, respectively. Average surface roughness of the oxide films was closely consistent with coating thickness results, and surface roughness increases as the coating thickness increases. From the comparison of coating thickness results with average surface roughness of the MAO films, relationship between the surface roughness and coating thickness of the oxide films can be observed.

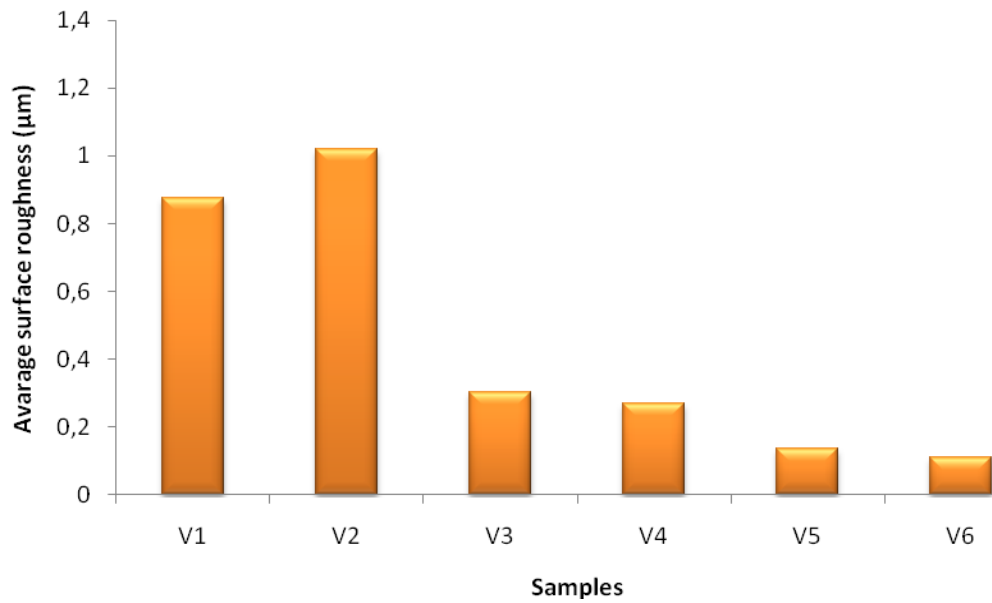


Figure 6.7: Average surface roughness of the samples treated with constant voltage mode

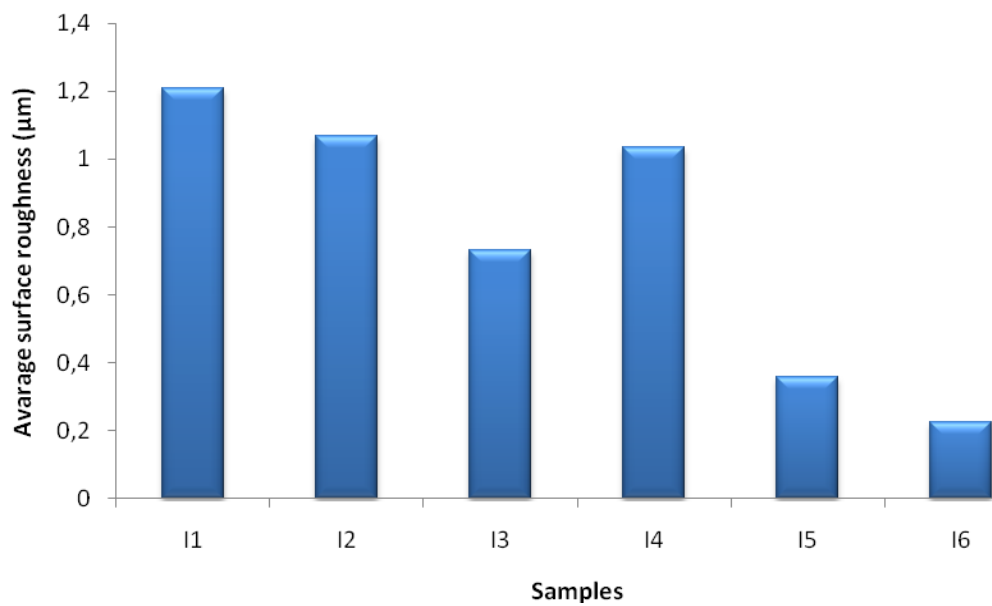


Figure 6.8: Average surface roughness of the samples treated with constant current mode

The wear track areas of the samples treated with voltage controlled and current controlled modes are presented in Figure 6.9 and Figure 6.10, respectively. In voltage controlled oxidation studies, the wear track area first increased (wear resistance decreased) with the applied voltage and then decreased, and the best wear

resistance was obtained from the sample oxidized with V^+ : 500 V/ V^- : 200 V. In current controlled oxidation studies, on the other hand, the wear track area continuously increased with increasing current values. It should also be mentioned that negative voltage and negative current values also have a significant effect on wear resistance, and wear resistance increased as the negative voltage or negative current increased. During the wear test, sliding distance was also recorded as a function of sliding distance, and presented in Appendix F. It is shown that friction coefficient of the samples for both voltage controlled and current controlled studies varied in the range of 0.4-0.6.

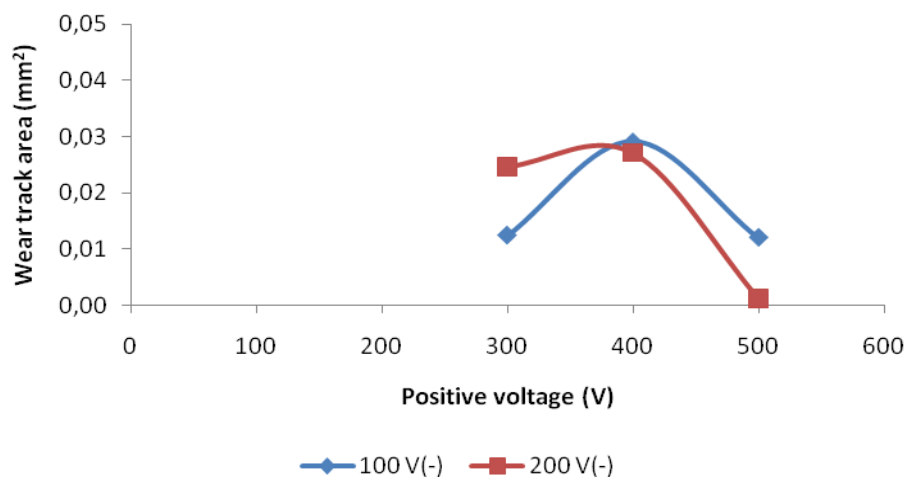


Figure 6.9: The change of wear track area with positive and negative voltage

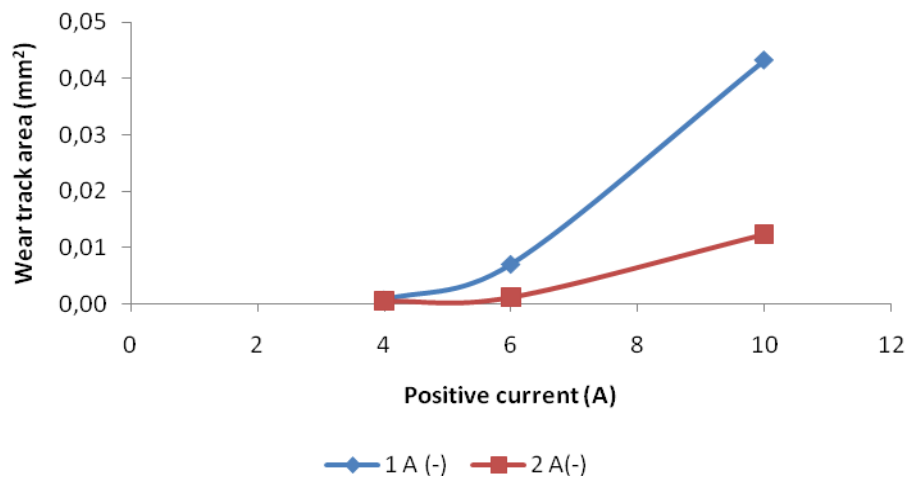


Figure 6.10: The change of wear track area with positive and negative current

Based on the experimental results obtained from the samples oxidized, whose results are presented in Figure 6.1 to Figure. 6.10, two samples were selected from both voltage controlled and current controlled oxidation studies. Further oxidation studies were performed on those samples to achieve the maximum possible coating thickness. For this purpose, voltage controlled oxidation studies were progressed until the current reaches almost zero level, and current controlled oxidation studies were progressed until the voltage level reaches the upper limit of the equipment. However, in the voltage controlled oxidation studies, it was impossible to perform oxidation at V^+ :500, V^- :200 V for longer durations to achieve thicker coatings than presented in Figure 6.5 because there was excessive gas evolution during oxidation at those voltage levels. To overcome this drawback, negative voltage level was reduced to 150 V and the oxidation could be progressed until the current reaches to zero level. On the other hand, current controlled oxidation studies could be progressed until the limit of the equipment was achieved. Table 6.1 lists the processing parameters of the MAO process held to achieve maximum coating thickness.

Table 6.1: Micro arc oxidation parameters selected to achieve maximum coating thickness.

Sample Code	Applied Voltage (V)		Applied Current (A)		Pulse Duration (μ s)		
	Positive	Negative	Positive	Negative	Positive	Neutral	Negative
V100	500	100	Variable	Variable			
V150	500	150	Variable	Variable	5000	200	5000
I410	Variable	Variable	4	1			
I420	variable	Variable	4	2			

In Figure 6.11 cross-sectional optical micrographs of those samples were presented. The sample V150, which was oxidized for 60 min, exhibited the maximum coating

thickness as 234 μm . The samples treated using current controlled mode have significantly thinner coatings since they could only be treated for 15 minutes.

XRD pattern of the sample V150 is presented in Figure 6.12. When it is compared to Figure 6.4 showing XRD pattern of the sample oxidized for shorter duration, it is clearly seen that, several alpha alumina peaks beside gamma alumina peaks appeared, and the aluminum peaks coming from the substrate were disappeared after oxidation for 60 min.

General view, surface optical micrographs, surface SEM micrographs and XRD patterns of these samples can be found in Appendix A, Appendix B and Appendix C. and Appendix E.

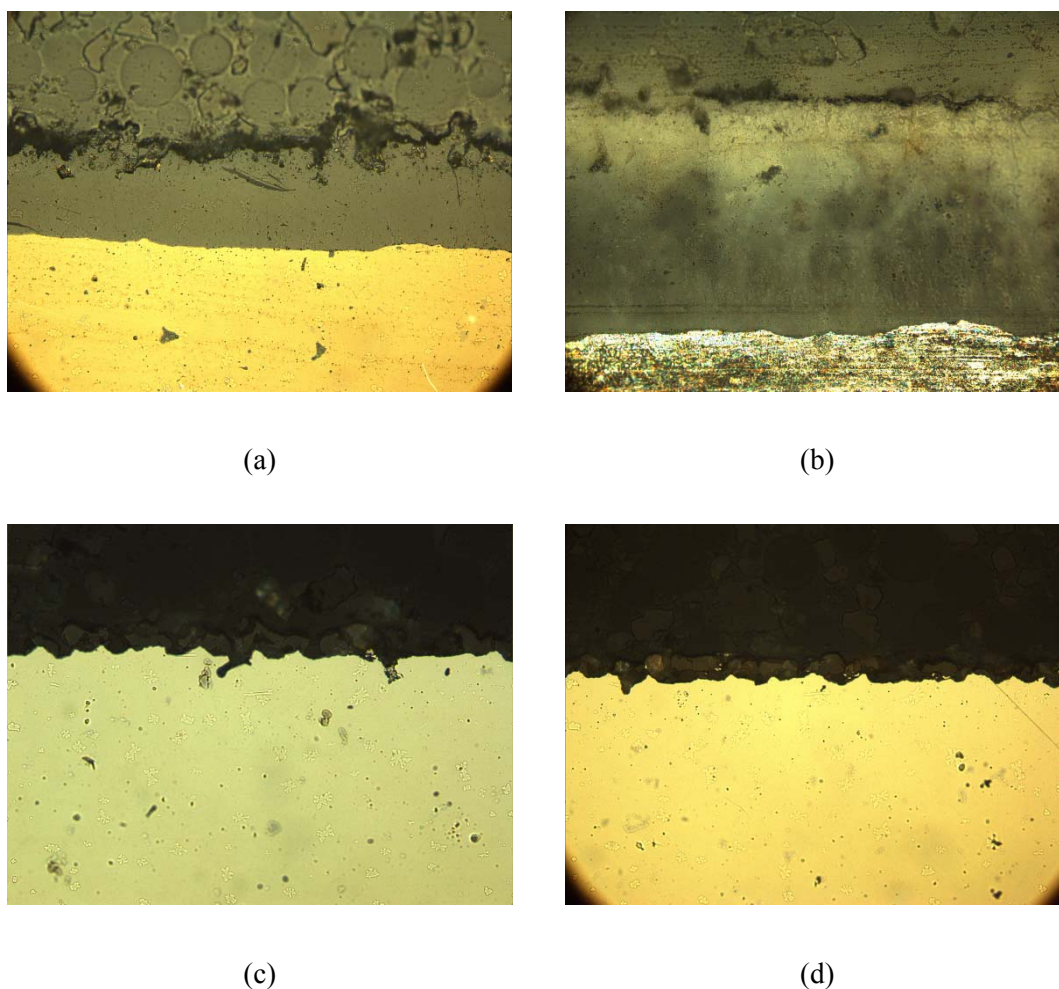


Figure 6.11: Cross-sectional optical microscopy images of samples, (a) V100, (b) V150, (c) I410, (d) I420, 500x

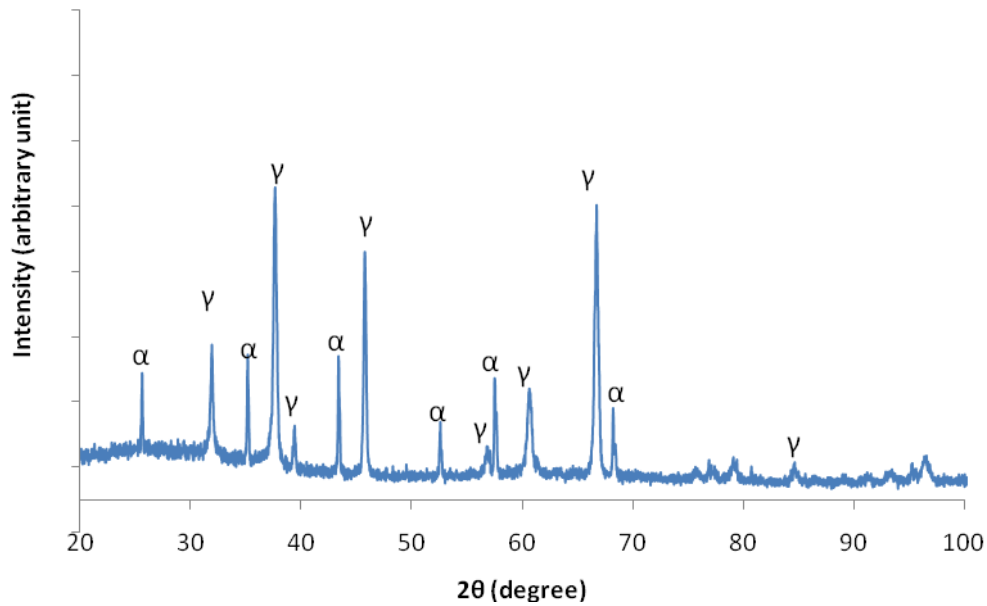


Figure 6.12: X-Ray diffraction patterns of the samples V150

The coating thicknesses of the samples are presented in Figure 6.13. There is a substantial difference between the thickness of the samples oxidized under constant voltage and constant current modes. The coating thickness of the samples V100 and V150 are 87 and 234 μm , respectively, while the coating thicknesses of the samples I410 and I420 are 10,5 and 11,1 μm , respectively. The difference of coating thickness between the sample V100 and V150 indicates the importance of the negative voltage applied to samples. It is clear to obtain almost three times thicker coatings by selecting the proper negative voltage.

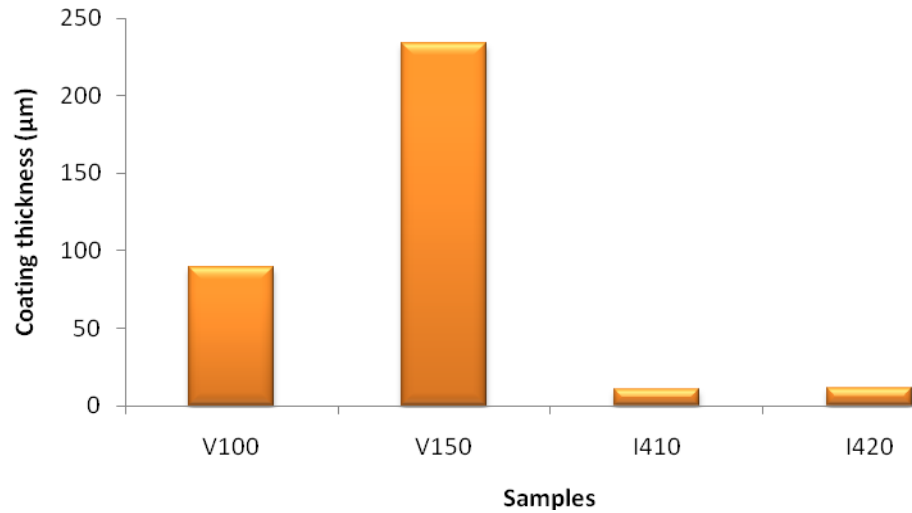


Figure 6.13: Coating thickness of the samples oxidized under voltage and current controlled modes.

The average surface roughness of the samples is presented in Figure 6.14. It is clear that surface roughness is well accompanied with the coating thickness in that the roughest surface belongs to the thickest sample. It is well known that surface roughness of the micro arc oxidized samples is related to spark formation during oxidation, which also contributes to increase thickness [18, 47].

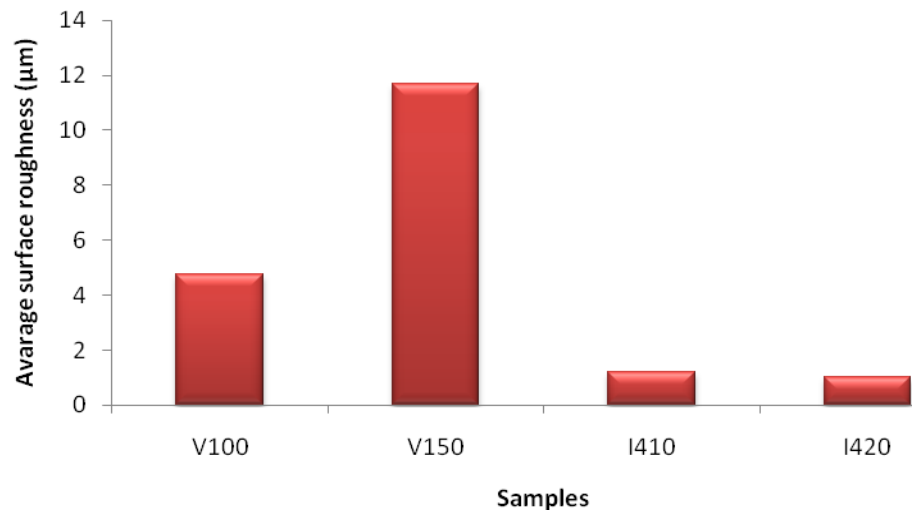


Figure 6.14: Average surface roughness of the samples oxidized under voltage and current controlled modes.

After achieving the maximum coating thickness on aluminum samples, wear tests were also performed on the surface of these four samples in order to see the effect of coating thickness on the wear resistance. Results of wear test are presented in Figure 6.15. The data of friction coefficient and friction force as a function of sliding distance obtained through wear tests are presented in Appendix F. Even though the sample V150 has the largest coating thickness, its wear resistance was the worst among the four samples. This behavior must be attributed to higher amount of porosity of a thicker MAO coating or increased surface roughness.

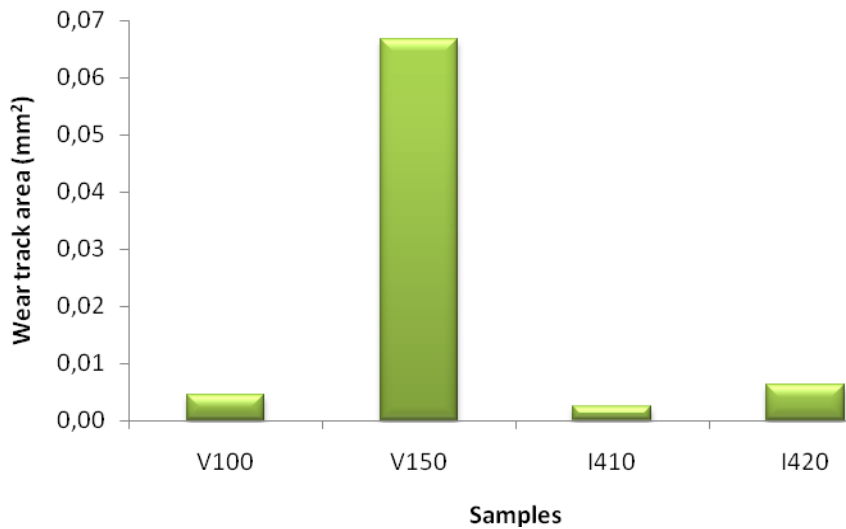
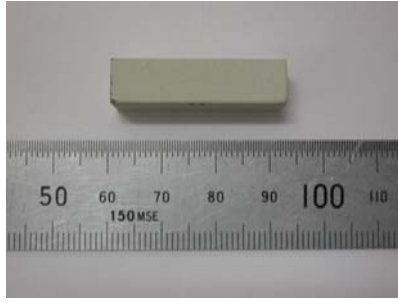


Figure 6.15: Wear track area of the samples of the samples oxidized under voltage and current controlled modes.

6.2 The Effect of Pulse Durations

As mentioned in Section 5.2, the power supply used in this thesis was capable of adjusting the pulse durations of voltage or current. In order to investigate the effect of pulse duration, the sample V150, which has the thickest coating, was selected and several different pulse durations as given in Table 5.4 were applied.

General view of some representative samples oxidized for different pulse durations are presented in Figure 6.16 and in Appendix A. There was no delamination or peeling from the coating. The colors of the coatings were also similar to each other, except the sample 521 (t^+ :5000 μ s, $t^{n\ddot{o}tr}$:200 μ s, t^- : 1000 μ s).



(a)



(b)

Figure 6.16: General view of the MAO treated samples after pulse duration studies (a) 325, (b) 521

The surfaces of oxide ceramic coatings were also examined by means of SEM as given in Figure 6.17. Optical surface and cross-sectional optical micrographs can be found in Appendix B and Appendix D, respectively. Since the melted materials are ejected out of the channel and cooled rapidly due to their immediate contact with the electrolyte, they lead to leave a pancake and rough structure behind and overall increase in the coating thickness. Therefore, a rough surface is a typical morphology of the micro arc oxidized sample as a result of the discharge channels formed on the surface. As can be seen from presented SEM images it should be noted that it is obvious even from surface micrographs, the sample 425 exhibits maximum surface roughness. Some micro cracks are also appeared on the surface as can be seen in Figure 6.17f, which could be initiated by the thermal stress attributed to the rapid solidification of the alumina melted in the discharge tunnel. In the discharge channel, instantaneous temperatures can reach up to 10000°K to make the coating melt near the channel. When the melted alumina is in contact to the electrolyte as already mentioned, the cooling rate can reach up to 10^8K/s . Therefore, the appearance of cracks is inevitable [1].

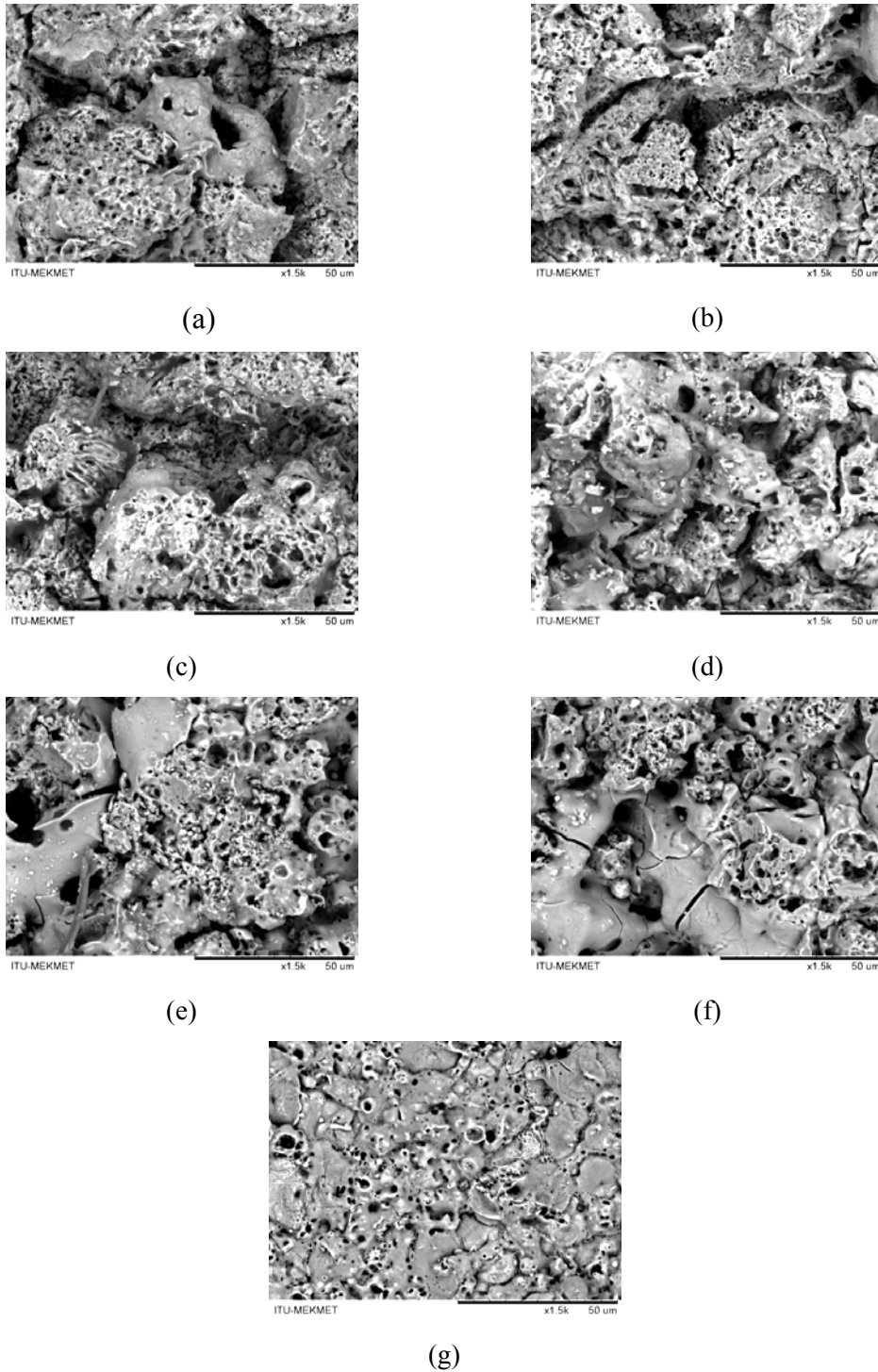


Figure 6.17: Surface SEM micrographs of the samples oxidized for different pulse durations (a) 325, (b) 425, (c) 525, (d) 524, (e) , 523 (f) 522,(g) 521.

Figure 6.18 shows the XRD patterns of the sample oxidized for different pulse durations. As can be seen in the corresponding XRD patterns, (113) and (400) peaks with strong diffraction intensities are identified as the characteristic diffraction peaks of α - Al_2O_3 and γ - Al_2O_3 , at 42° and 45° , respectively. So the relative contents of α -

Al_2O_3 and $\gamma\text{-Al}_2\text{O}_3$ (C_α and C_γ) can be seen on the basis of the integrated diffraction intensities of (113) and (400) peaks [46]. By comparing the characteristic diffraction peaks, XRD analysis revealed that the sample 525 has the maximum amount of alpha alumina.

In the MAO process, the aluminum substrate is directly oxidized to become α and γ phases due to a high temperature sintering in the micro arc zone. Alpha alumina is the stable phase of aluminum oxide with a melting point of 2050°C and is characterized by a high hardness, second after diamond in Mohs hardness scale. gamma is the metastable phase which can be transformed into alpha by heating in the temperature range from 800°C to 1200°C [30].

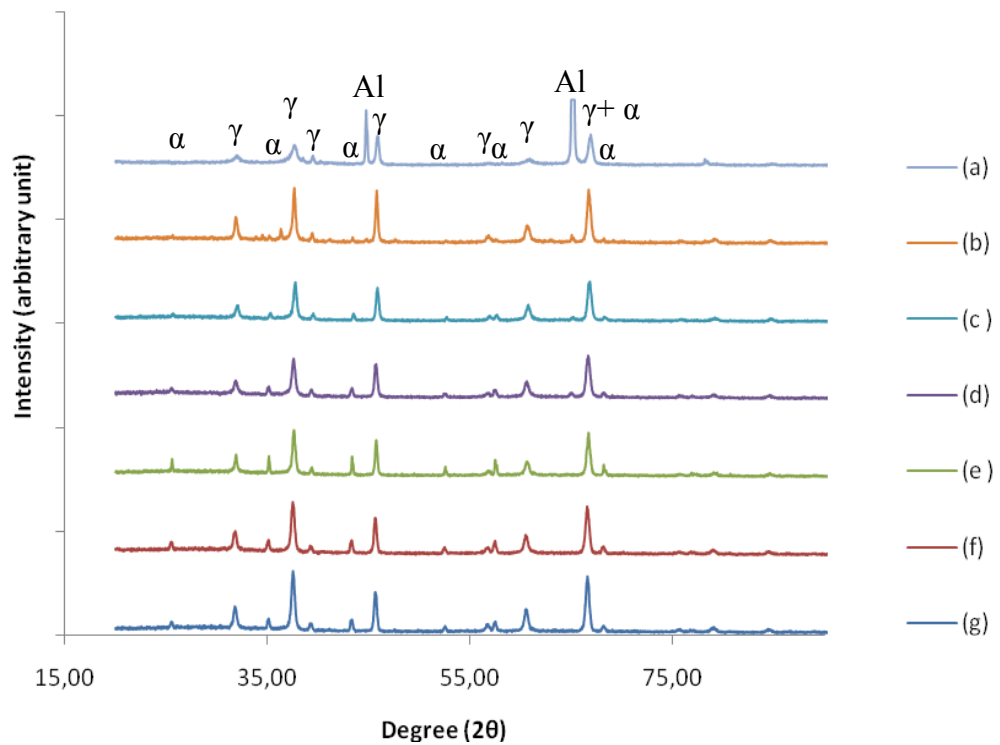


Figure 6.18: XRD patterns of the samples oxidized for different pulse durations (a) 521, (b) 522, (c) 523, (d) 524, (e) , 525 (f) 425,(g) 325.

The coating thickness of the samples oxidized for different pulse durations are presented in Figure 6.19. It shows an increasing trend as the positive voltage durations increases with a constant negative pulse duration, and the thickness decreases as the negative pulse durations decrease.

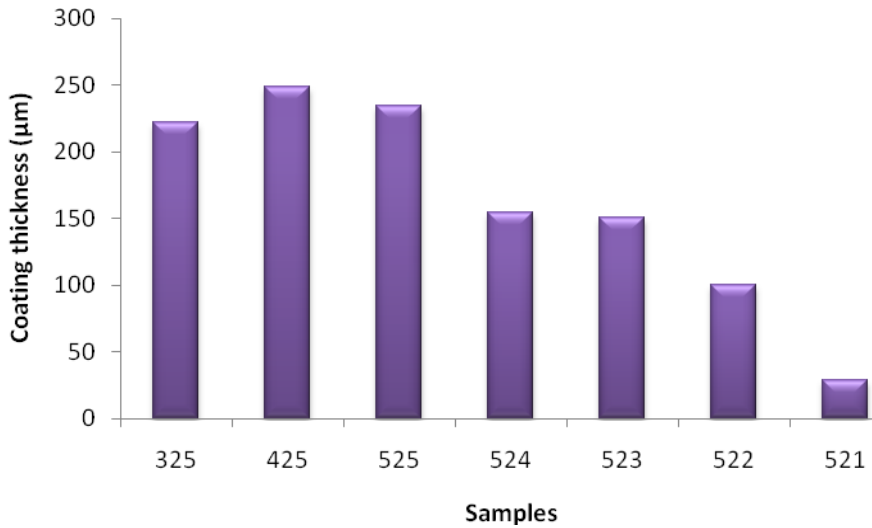


Figure 6.19: Variation of coating thickness as a function of pulse durations.

The average surface roughness of the samples oxidized for different pulse durations are presented in Figure 6.20. As can be seen from Figure 6.20, variation of surface follows a similar trend as the thickness variation. Increment in positive pulse durations has generally an increasing effect of surface roughness, while shorter negative pulse durations decrease the average surface roughness.

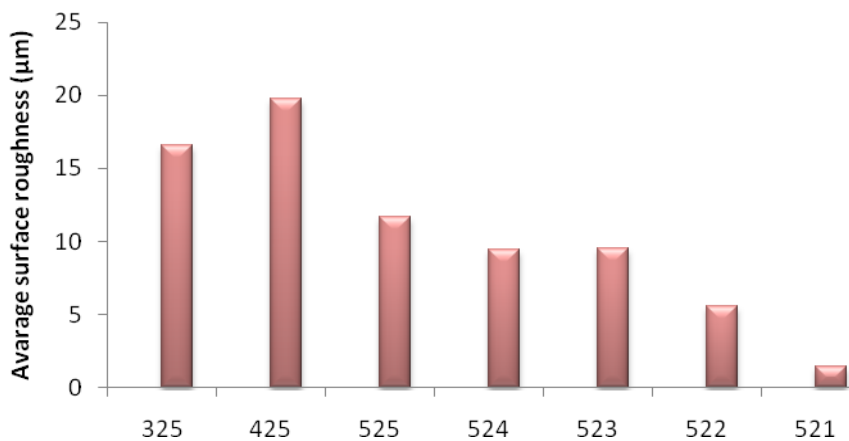


Figure 6.20: Change of average surface roughness with different pulse durations

Cross-sectional SEM images of oxide layers oxidized for different pulse durations are presented in Figure 6.21. It seems that all the samples investigated had a uniform coating distribution over the entire surface. Adhesion between oxide layer and substrate is continuous as well, there is no gap, no delamination, no porosity between the substrate and the oxide layer. SEM observations also confirmed that the sample 425 has the thickest coating layer.

One of the characteristic features of the MAO coating is to consist of two different layers, namely outer and inner layer. The outer layer that covers the MAO coatings is loose and porous; on the contrary the inner layer is denser. From the cross sectional SEM micrographs given in Figure 6.21, it can easily be distinguished loose and dense layer of the coatings. Generally, through the coating, porosity decrease and for some samples (Figure 6.21e and f) there is almost no porosity close to the interface. The sample 521 seems to have the highest porosity content among the samples investigated.

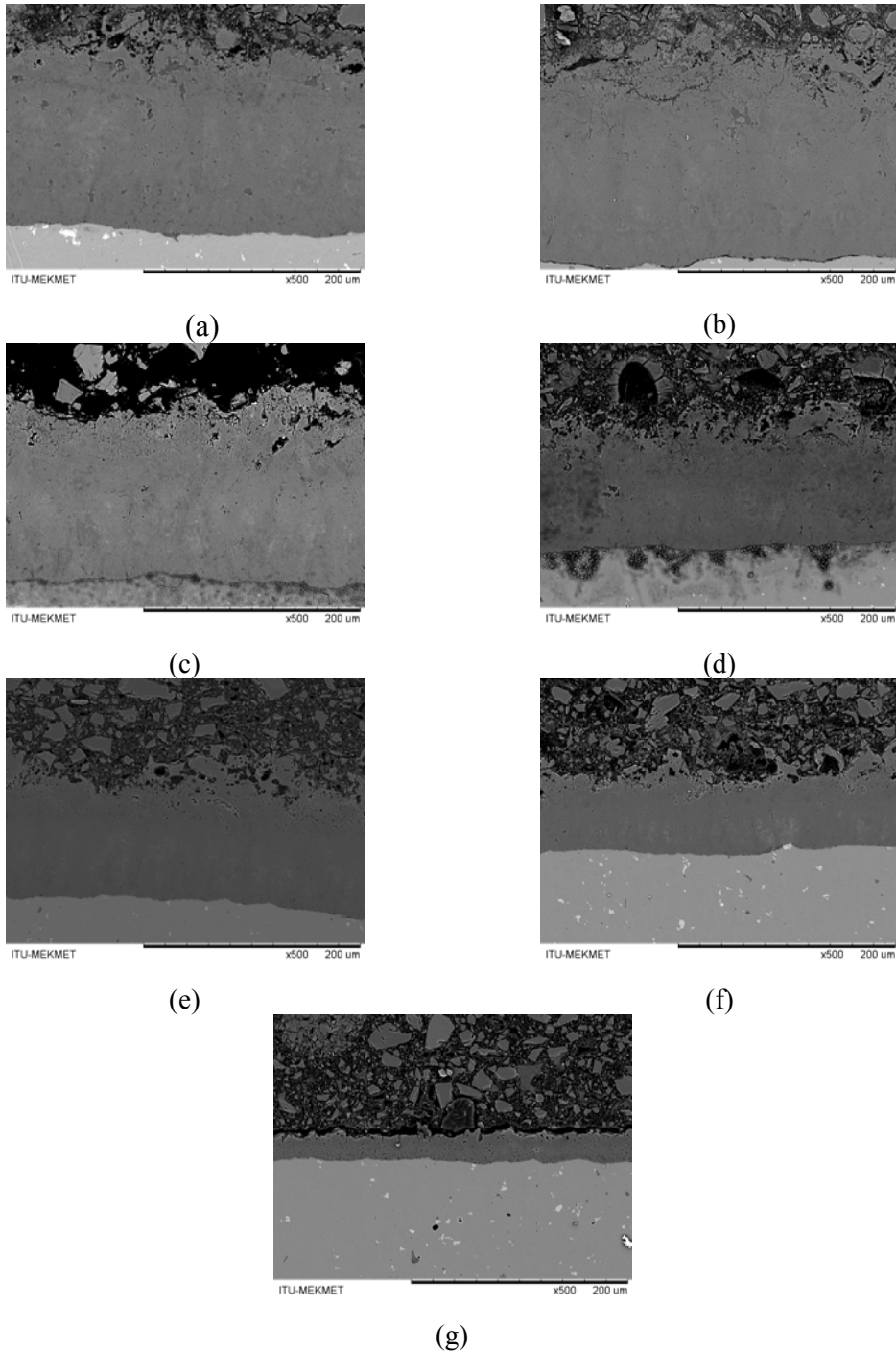


Figure 6.21: Cross-sectional SEM analyses of MAO samples treated with different pulse duration time (a) 325, (b) 425, (c) 525, (d) 524, (e) , 523 (f) 522,(g) 521

Hardness of the coating layer measured from the cross sections of the sample are given in Figure 6.22 as a function of the applied pulse durations. Hardness of the samples investigated are almost the same except the sample 522 and 521 which have the highest and lowest hardness, respectively. The results suggest that there was not a direct and simple relationship between pulse duration and hardness. It has been

reported in the open literature [1] that with the increased thickness, amount of alpha alumina increases. But it should also be considered that the porosity content within the coating has also an effect of hardness obtained.

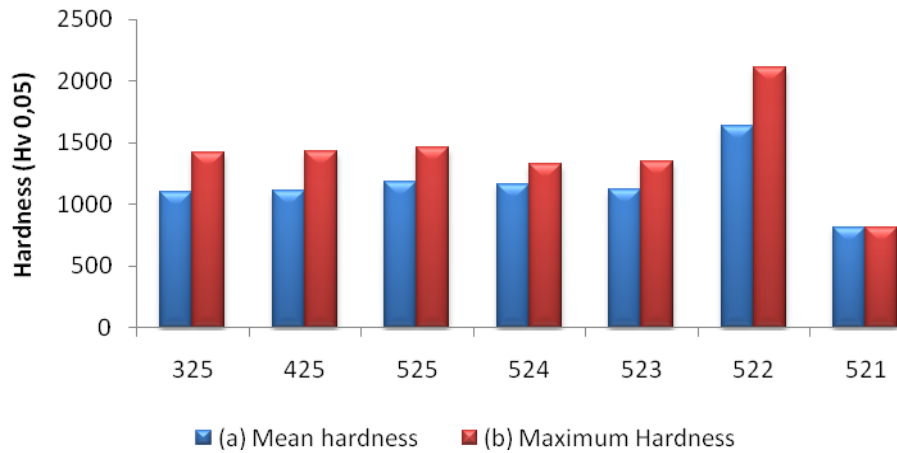


Figure 6.22: Micro-hardness values of MAO coatings treated with different pulse durations a) Mean hardness values, b) Maximum hardness values of samples

Relative wear rate of the samples oxidized for different pulse durations are given in Figure 6.23 in comparison to that of bare 7075 alloy. The relative wear rates of the coatings were calculated by dividing the wear rate of each sample to that of 7075 bare aluminum alloy then multiplied by 100. The wear rate of the bare alloy can be reduced by about a four orders of magnitude upon the micro arc oxidation process. On the other hand, there is no systematic variation among the wear rates of the micro arc oxidized samples. The porous structure of the MAO coatings, especially outer layer, may increase the wear rate but on the other hand, porous structure of the MAO coatings could also decrease wear rate in wet condition by acting as a lubricant [3, 23].

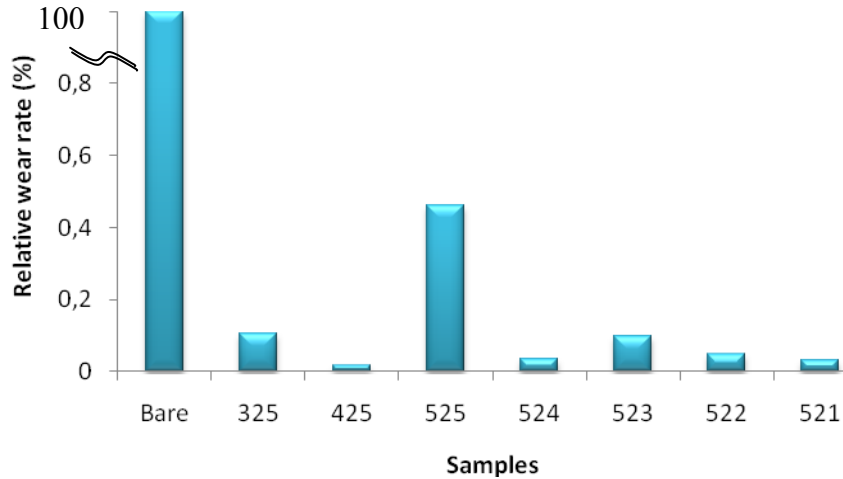


Figure 6.23: Relative wear rates of the bare alloy and MAO samples oxidized for different pulse durations

Specific corrosion loss of the samples as a function of immersion time and the corresponding pH variation are presented in Figure 6.24 and Figure 6.25, respectively. The sample having the thinnest coating exhibited the worst resistance to corrosion even it is worse than the bare alloy. On the other hand, the sample 325 exhibited the best resistance to corrosion even though it does not have the thickest coating. More local defects such as micro cracks and micro fractures attributed to relatively larger stress may present in thicker coating than the thinner one. Those defects act as the passages which facilitate eroding ions to enter to the coating and subsequently may lead the worse corrosion resistance of the ceramic coating. Consequently, thicker coatings may have worse resistance to corrosion because of these defects. On the other hand, pH of corrosion solution seems to be relevant with the specific corrosion loss. As the corrosion resistance decreases, pH of the solution increases possibly because of incorporating corrosion products into the solution.

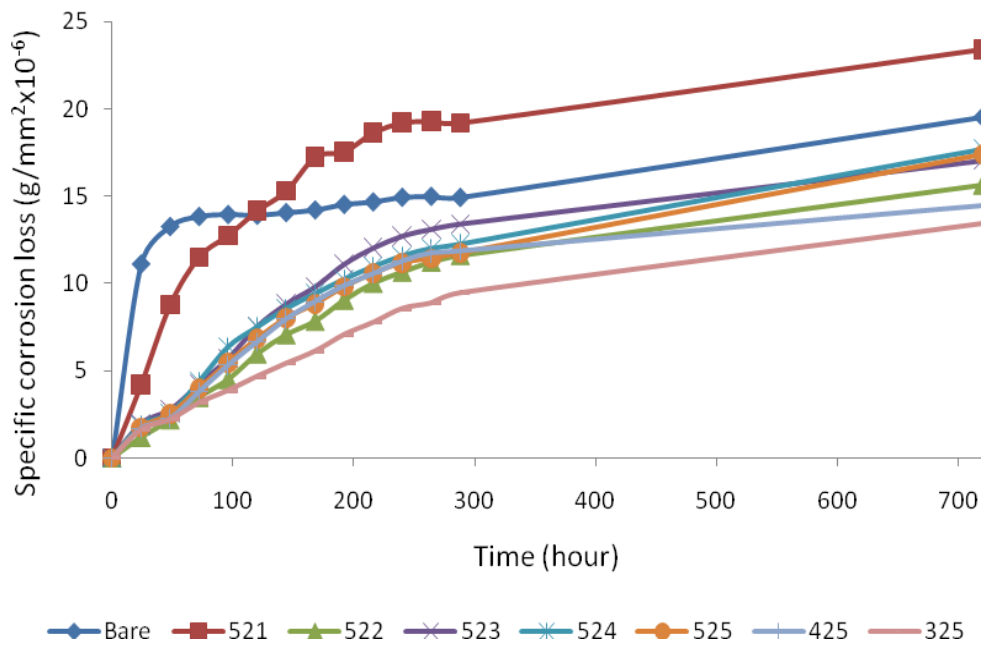


Figure 6.24: Specific corrosion loss of the samples as a function of immersion time.

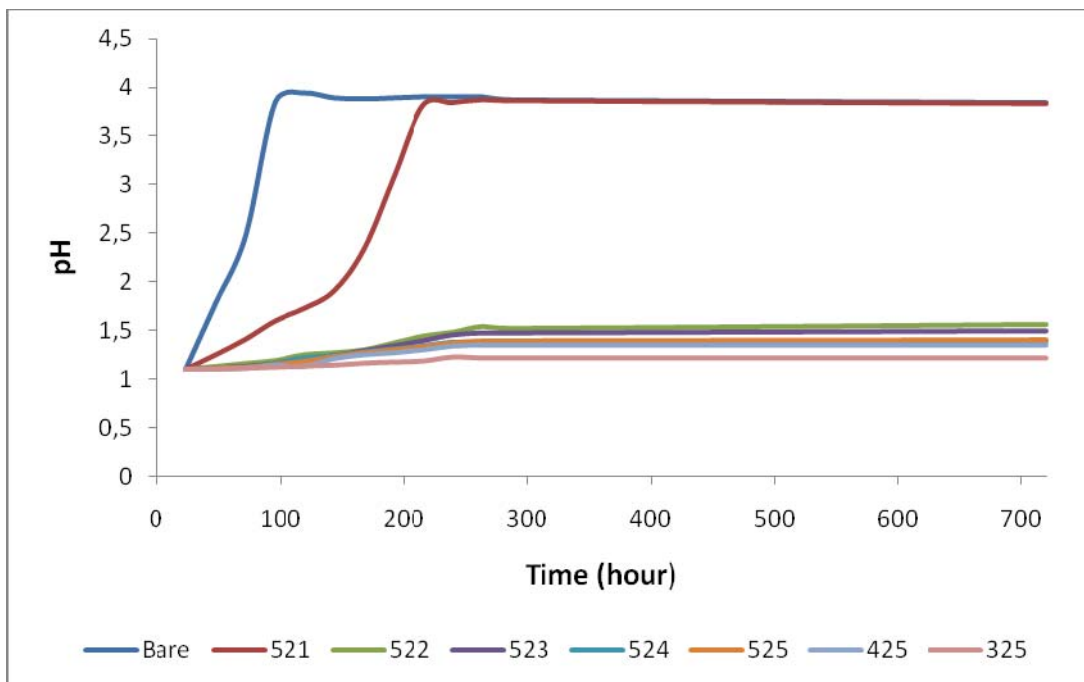


Figure 6.25: pH variation of the solution during immersion corrosion tests.

7. CONCLUSIONS

Based on the results obtained from the present thesis, the following conclusions can be drawn:

1. Micro arc oxidation of 7075 aluminum alloy results in a ceramic coating comprising alpha and gamma form of alumina, and the relative amount of alpha alumina increases as the oxidation time increases.
2. Voltage controlled MAO studies reveal that it is not possible to obtain a uniform coating on 7075 aluminum substrate at positive voltages smaller than 500V.
3. Under a constant positive voltage of 500V, coating thickness increases as the negative voltage increases.
4. Constant voltage controlled MAO process results in a thicker coating when compared to that obtained from the current controlled MAO process.
5. Under a constant positive voltage of 500V, wear resistance of the coating increases as the negative voltage increases. It is also valid for current controlled MAO process. Under a constant positive current of 6A and 10 A, wear resistance of the coating increases as the negative current increases.
6. Hardness of the unoxidized bare alloy can be increased higher than 2000 HV_{0,05} by selecting appropriate processing parameters.
7. In the constant voltage controlled MAO process, coating thickness decreases as the negative pulse durations decrease.
8. There is a close relationship between surface roughness and coating thickness in the MAO process.
9. Cross-sectional micrographs of the oxidized samples reveal that the MAO coatings mostly consist of two different layers, namely loose outer layer and denser inner layer.
10. The thickest coating exhibits the smallest wear rate, however no simple relationship can be established the coating thickness and the wear rate.

11. Corrosion resistance of bare 7075 aluminum alloy can be improved by selecting the appropriate MAO processing parameters.

REFERENCES

- [1] **Wei, T., Yan, F., Tian, J.**, Characterization and wear- and corrosion-resistance of Micro arc oxidation ceramic coatings on aluminum alloy, *Journal of Alloys and Compounds* 389 (2005) 169–176.
- [2] **Krishna, L. R., Purnima, A. S., Sundararajan, G.**, A comparative study of tribological behavior of microarc oxidation and hard-anodized coatings, *Wear*, 261 (2006) 1095–1101.
- [3] **Zhou, F., Wang, Y., Ding, H., Wang, M., Yu, M., Dai, Z.**, Friction characteristic of micro-arc oxidative Al₂O₃ coatings sliding against Si₃N₄ balls in various environments, *Surface & Coatings Technology*, 202 (2008) 3808–3814.
- [4] **Totten, G. E., MacKenzie, D. S.**, *Handbook of Aluminum*, Marcel Dekker, 2003.
- [5] **Kaufman, J. G.**, *Introduction to Aluminum Alloys and Tempers*, ASM International, 2000.
- [6] **Liu, Z., Gao, W.**, A novel process of electroless Ni-P plating with plasma electrolytic oxidation pretreatment, *Applied Surface Science*, 253 (2006) 2988–2991.
- [7] **Baydoğan, M.**, T6 ve RRA ısıtıl işleme uygulanan 2014 ve 7075 kalite alüminyum alaşımlarının mekanik ve korozyon özelliklerinin incelenmesi, PhD thesis, 2003.
- [8] **Xin, S., Song, L., Zhao, R., Hu, X.**, Composition and thermal properties of the coating containing mullite and alumina, *Materials Chemistry and Physics*, 97 (2006) 132–136.
- [9] **Curran, J. J.**, *Thermal and Mechanical Properties of Plasma Electrolytic Oxide Coatings*, thesis of Doctor degree, 2005.
- [10] **Yerokhin, A. L., Nie, X., Leyland, A., Matthews, A., Dowey, S. J.**, Plasma electrolysis for surface engineering, *Surface and Coatings Technology*, 122 (1999) 73–93.
- [11] **Guangliang, Y., Xianyi, L., Yizhen, B., Haifeng, C., Zengsun, J.**, The effects of current density on the phase composition and microstructure properties of micro-arc oxidation coating, *Journal of Alloys and Compounds*, 345 (2002) 196–200.

- [12] **Zheng, H. Y., Wang, Y. K., Li, B. S., Han, G. R.**, The effects of Na₂WO₄ concentration on the properties of microarc oxidation coatings on aluminum alloy, *Materials Letters*, 59 (2005) 139–142.
- [13] **Wang, C., Zhang, D., Jiang, Y.**, Growth process and wear resistance for ceramic coatings formed on Al-Cu-Mg alloy by micro-arc oxidation, *Applied Surface Science*, 253 (2006) 674–678.
- [14] **Xin, S., Song, L., Zhao, R., Hu, X.**, Influence of cathodic current on composition, structure and properties of Al₂O₃ coatings on aluminum alloy prepared by micro-arc oxidation process, *Thin Solid Films*, 515 (2006) 326 – 332.
- [15] **Wu, H., Jin, Z., Long, B., Yu, F., Lu, X.**, Characterization of Microarc Oxidation Process on Aluminium Alloy, *Chin.Phys.Lett.*, Vol. 20, No. 10 (2003) 1815.
- [16] **Guangliang, Y., Xianyi, L., Yizhen, B., Haifeng, C., Zengsun, J.**, The effects of current density on the phase composition and microstructure properties of micro-arc oxidation coating, *Journal of Alloys and Compounds*, 345 (2002) 196–200.
- [17] **Gu, W., Lv, G., Chen, H., Chen, G., Feng, W., Zhang, G., Yang, S.**, Investigation of morphology and composition of plasma electrolytic oxidation coatings in systems of Na₂SiO₃–NaOH and (NaPO₃)₆–NaOH, *Journal of Materials Processing Technology*, 182 (2007) 28–33.
- [18] **Krishna, L. R., Purnima, A. S., Sundararajan, G.**, Mechanisms underlying the formation of thick alumina coatings through the MAO coating technology, *Surface and Coatings Technology*, 167 (2003) 269–277.
- [19] **Butyagin, P. I., Khokhryakov, Y. V., Mamaev, A. I.**, Microplasma systems for creating coatings on aluminium alloys, *Materials Letters*, 57 (2003) 1748–1751.
- [20] **Kuhn, A. T.**, Plasma anodized aluminum-A 2000/2000 ceramic coating, *Aluminum Finishing*.
- [21] **Wei, C. B., Tian, X. B., Yang, S. Q., Wang, X. B., Fu, R. K. Y., Chu, P. K.**, Anode current effects in plasma electrolytic oxidation, *Surface & Coatings Technology*, 201 (2007) 5021–5024.
- [22] **Gnedenkov, S. V., Khrisanfova, O. A., Zavidnaya, A. G., Sinebrukhov, S. I., Gordienko, P. S., Iwatsubo, S., Matsui, A.**, Composition and adhesion of protective coatings on aluminum, *Surface and Coatings Technology* 145, 2001, 146-151.
- [23] **Zhu, M. H., Cai, Z. B., Lin, X. Z., Ren, P. D., Tan, J., Zhou, Z. R.**, Fretting wear behaviour of ceramic coating prepared by micro-arc oxidation on Al–Si alloy, *Wear*, 263 (2007) 472–480.

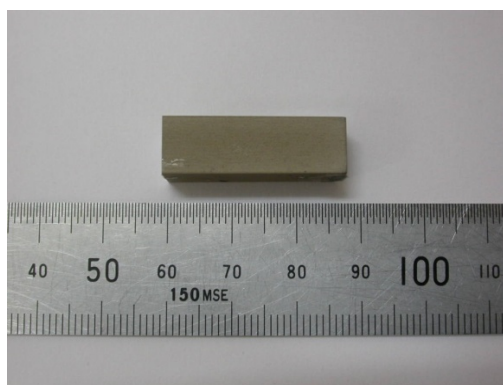
- [24] **Malyshev, V. N., Zorin, K. M.**, Features of microarc oxidation coatings formation technology in slurry electrolytes, *Applied Surface Science*, 254 (2007) 1511–1516.
- [25] **Xue, W., Deng, Z., Chen, R., Zhang, T.**, Growth regularity of ceramic coatings formed by microarc oxidation on Al–Cu–Mg alloy, *Thin Solid Films* 372, 2000, 114–117.
- [26] **Yerokhin, A. L., Voevodin, A. A., Lyubimov, V. V., Zabinski**, Plasma electrolytic fabrication of oxide ceramic surface layers for tribotechnical purposes on aluminium alloys, *Surface and Coatings Technology*, 110 (1998) 140–146.
- [27] **Yerokhin, A. L., Voevodin, A. A., Lyubimov, V. V., Zabinski, J., Donley, M.**, Growth mechanism of black ceramic layers formed by microarc oxidation, *Surface and Coatings Technology*, 110 (1998) 140–146.
- [28] **Snizhko, L. O., Yerokhin, A. L., Pilkington, A., Gurevina, N. L., Misnyankin, D. O., Leyland, A., Matthews, A.**, Anodic processes in plasma electrolytic oxidation of aluminium in alkaline solutions, *Electrochimica Acta*, 49 (2004) 2085–2095.
- [29] **Zheng, H. Y., Wang, Y. K., Li, B. S., Han, G. R.**, The effects of Na₂WO₄ concentration on the properties of microarc oxidation coatings on aluminum alloy, *Materials Letters*, 59 (2005) 139–142.
- [30] **Anita, V., Saito, N., Takai, O.**, Microarc plasma treatment of titanium and aluminum surfaces in electrolytes, *Thin Solid Films*, 506–507 (2006) 364–368.
- [31] **Lv, G., Gu, W., Chen, H., Feng, W., Khosa, M.L., Li, L., Niu, E., Zhang, G., Yang, S.**, Characteristic of ceramic coatings on aluminum by plasma electrolytic oxidation in silicate and phosphate electrolyte, *Applied Surface Science*, 253 (2006) 2947–2952.
- [32] **Yerokhin, A. L., Snizhko, L. O., Gurevina, N. L., Leyland, A., Pilkington, A., Matthews A.**, Spatial characteristics of discharge phenomena in plasma electrolytic oxidation of aluminium alloy, *Surface and Coating Technology*, 177–178 (2004) 779–783.
- [33] **Jaspard-Mécuson, F., Czerwiec, T., Henrion, G., Belmonte, T., Dujardin, L., Viola, A., Beauvir, J.**, Tailored aluminium oxide layers by bipolar current adjustment in the Plasma Electrolytic Oxidation (PEO) process, *Surface and Coatings Technology*, 201 (2007) 8677–8682.
- [34] **Tillous, E.K., Toll-Duchanoy, T., Bauer-Grosse, E.**, Microstructure and 3D microtomographic characterization of porosity of MAO surface layers formed on aluminium and 2214-T6 alloy, *Surface and Coatings Technology*, 203 (2009) 1850–1855.

- [35] **Curran, J.A., Clyne, T.W.**, Porosity in plasma electrolytic oxide coatings, *Acta Materialia*, 54 (2006) 1985-1993.
- [36] **Nie, X., Leyland, A., Song, H.W., Yerokhin, A.L., Dowey, S.J., Matthews, A.**, Thickness effects on the mechanical properties of micro-arc discharge oxide coatings on aluminium alloys, *Surface and Coatings Technology*, 116-119 (1999) 1055-1060.
- [37] **Mécuson, F., Czerwiec, T., Belmonte, T., Dujardin, L., Viola, A., Henrion, G.**, Diagnostics of an electrolytic microarc process for aluminium alloy oxidation, *Surface and Coatings Technology*, 200 (2005) 804-808.
- [38] **Wua, X., Qin, W., Guo, G., Xie, Z.**, Self-lubricative coating grown by micro-plasma oxidation on aluminum alloys in the solution of aluminate-graphite, *Applied Surface Science*, 254 (2008) 6395–6399.
- [39] **Lv, G., Chen, H., Gua, W., Feng, G., Li, L., Niu E., Zhang, X., Yang, S.**, Effects of graphite additives in electrolytes on the microstructure and corrosion resistance of Alumina PEO coatings, *Current Applied Physics*, 9 (2009) 324-328.
- [40] **Rama Krishna, L., Sudha Purnima, A., Sundararajan, G.**, A comparative study of tribological behavior of microarc oxidation and hard-anodized coatings, *Wear*, 261 (2006) 1095-1101.
- [41] **Yang, G.L., Lü X.Y., Bai Y.Z., Jin Z.S.**, Characterization of Microarc Oxidation Discharge Process for Depositing Ceramic Coating, *Chin. Phys. Lett.*, 18 (2001) 1141.
- [42] **Asquith, D.T., Yerokhin, A.L., Yates, J.R., Matthews, A.**, Effect of combined shot-peening and PEO treatment on fatigue life of 2024 Al alloy, *Thin Solid Films*, 515 (2006) 1187-1191.
- [43] **Jin, F., Wang, K., Zhua, M., Shena, L., Li, J., Honga, H., Chub, P.K.**, Infrared reflection by alumina films produced on aluminum alloy by plasma electrolytic oxidation, *Materials Chemistry and Physics* 114 (2009) 398–401.
- [44] ASM Metals HandBook, 9. Ed., Volume 02 - Properties and Selection Nonferrous Alloys and Special-Purpose Materials.
- [45] **Xue, W., Wang, C., Tian, H., Lai, Y.**, Corrosion behaviors and galvanic studies of microarc oxidation films on Al–Zn–Mg–Cu alloy, *Surface & Coatings Technology*, 201 (2007) 8695–8701.
- [46] **Gu, W., Lv, G., Chen, H., Chen, G., Feng, W., Zhang, G., Yang, S.**, Investigation of morphology and composition of plasma electrolytic oxidation coatings in systems of $\text{Na}_2\text{SiO}_3\text{--NaOH}$ and $(\text{NaPO}_3)_6\text{--NaOH}$, *Journal of Materials Processing Technology*, 182 (2007) 28–33.

- [47] **Jin ,F., Chu , P.K., Tong, H., Zhao, J.,** Improvement of surface porosity and properties of alumina films by incorporation of Fe micrograins in micro-arc oxidation, *Applied Surface Science*, 253 (2006) 863-868

APPENDICES

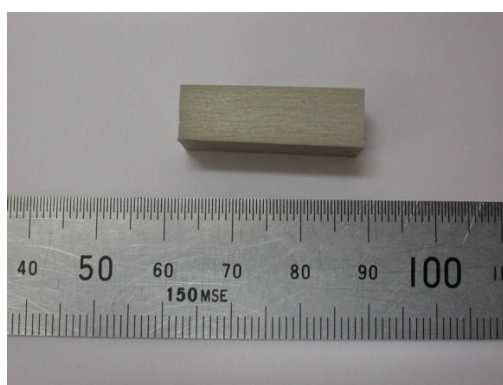
Appendix A



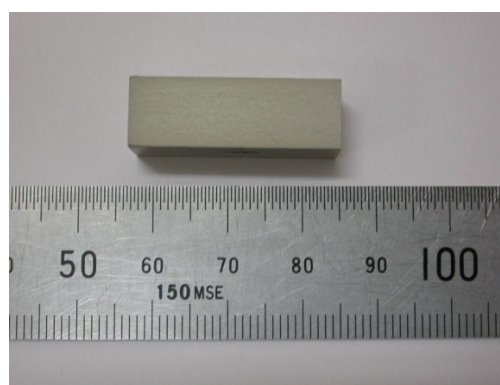
V1



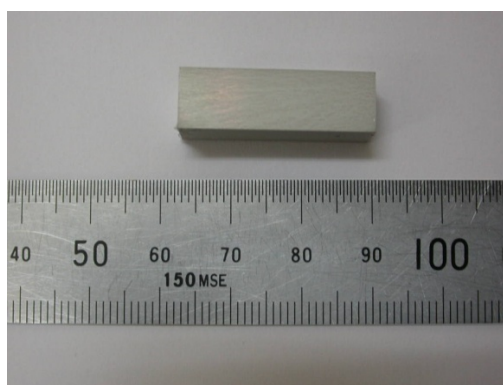
V2



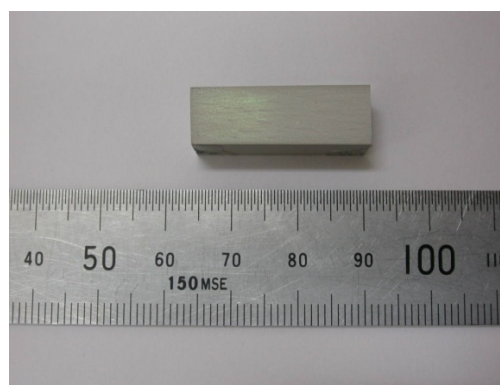
V3



V4

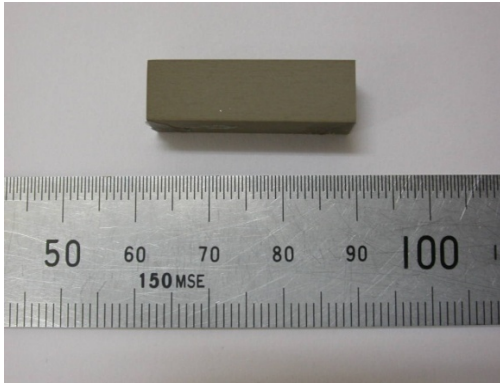


V5

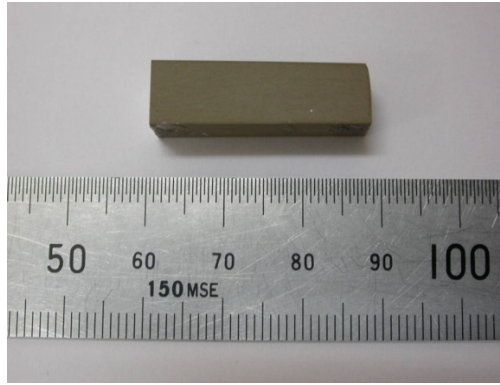


V6

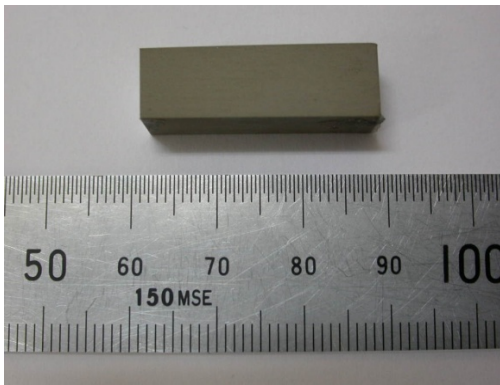
Figure A.1: General view of the samples oxidized under constant voltage mode



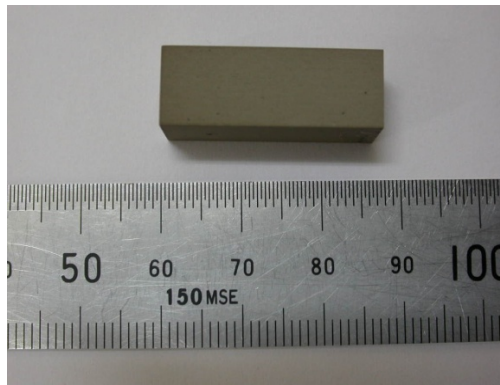
I1



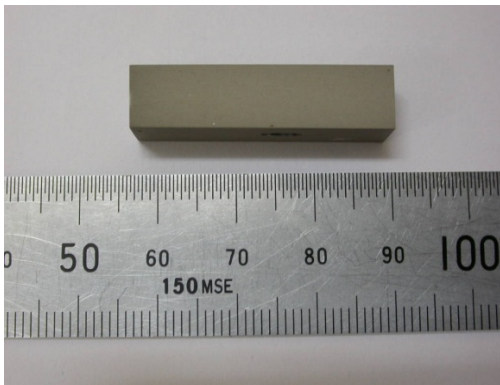
I2



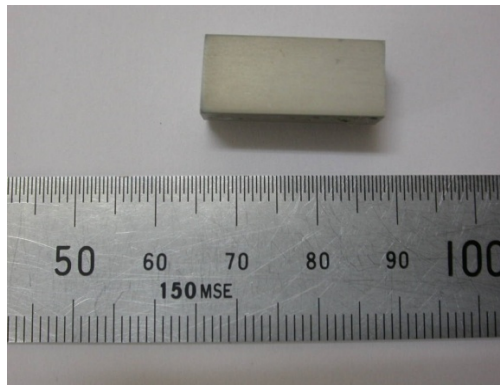
I3



I4

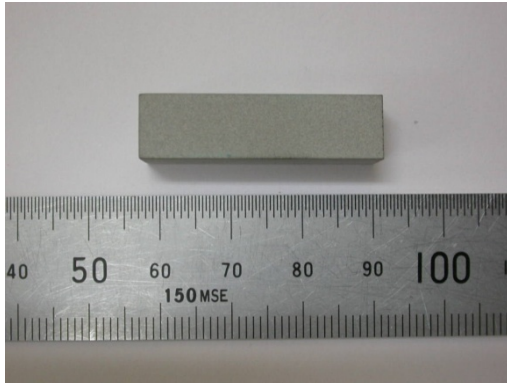


I5

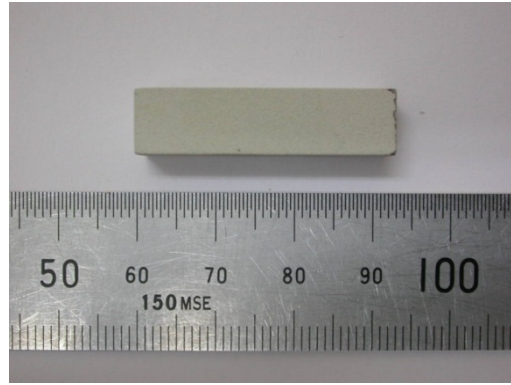


I6

Figure A.2: General view of the samples oxidized under constant current mode



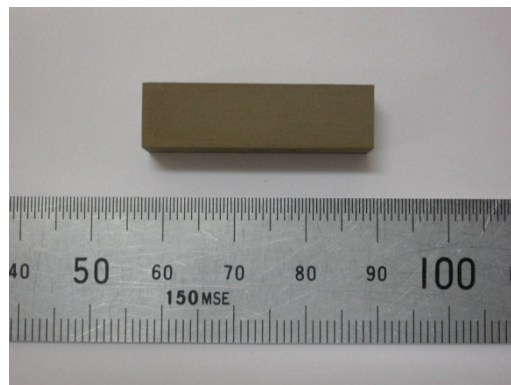
V100



V150

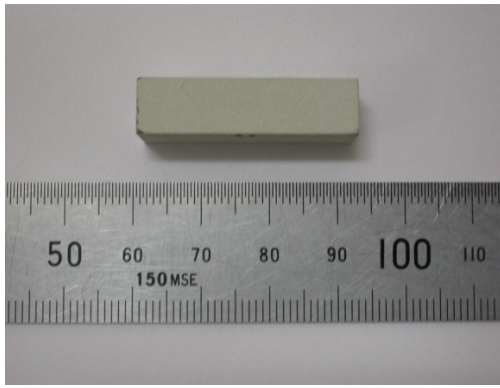


I410

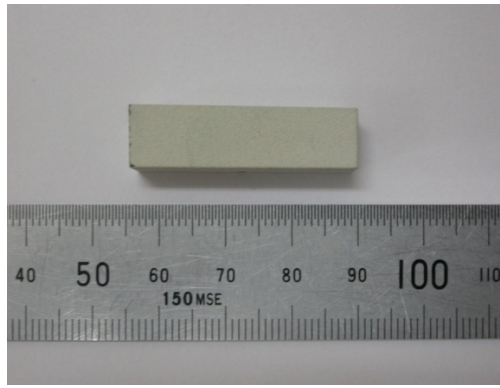


I420

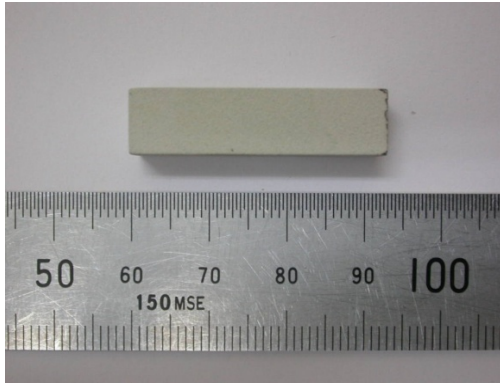
Figure A.3: General view of the samples oxidized to achieve maximum coating thickness



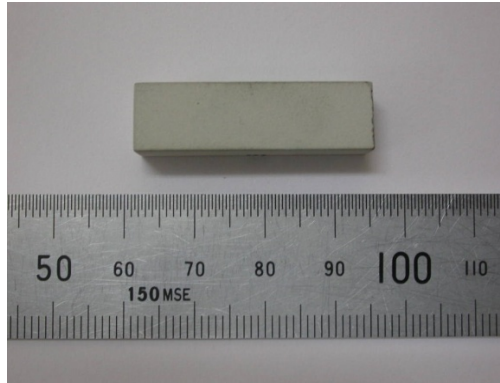
325



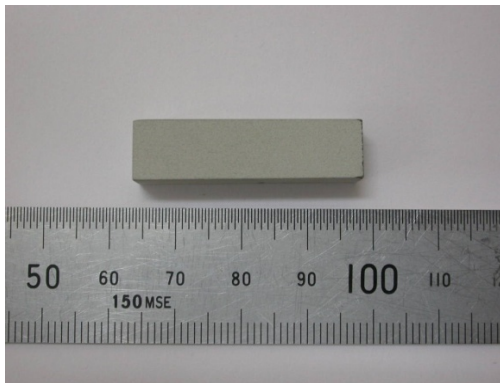
425



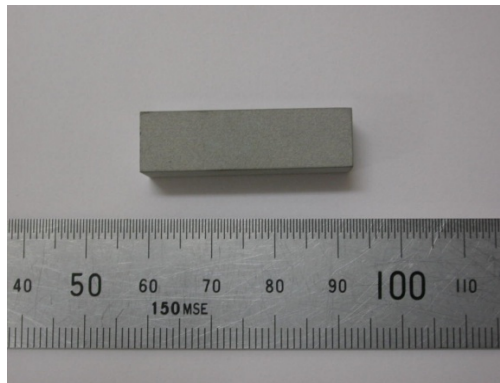
525



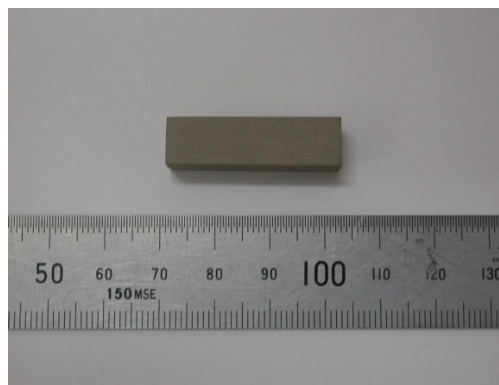
524



523



522



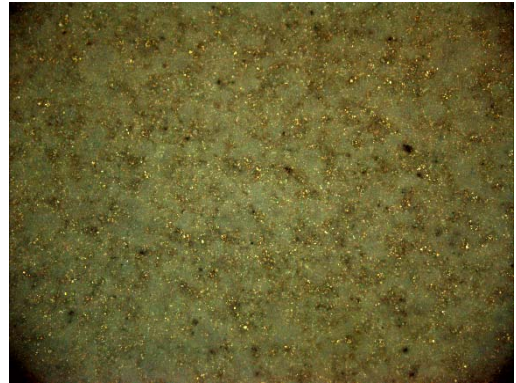
521

Figure A.4: General view of the MAO treated samples after pulse duration studies

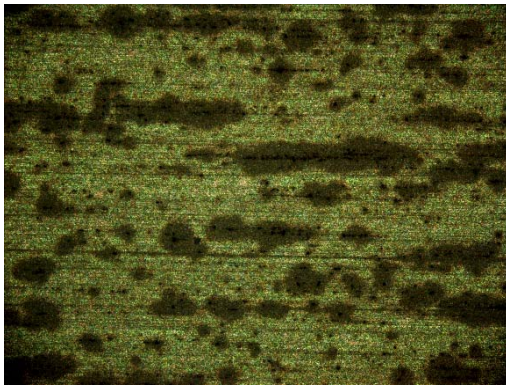
Appendix B



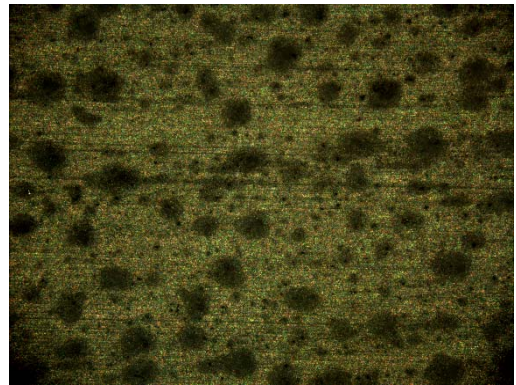
V1



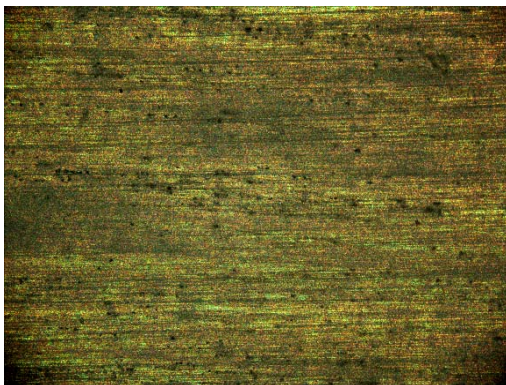
V2



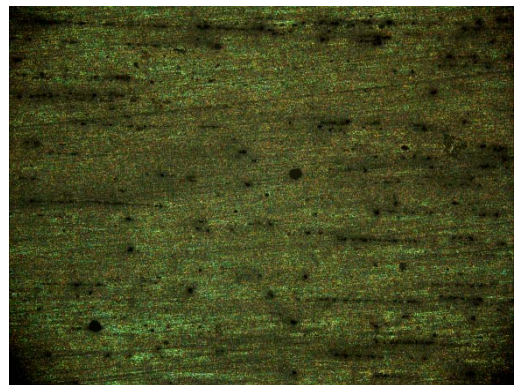
V3



V4



V5



V6

Figure B.1: Surface micrographs of the samples treated under voltage controlled mode, (100x)



11



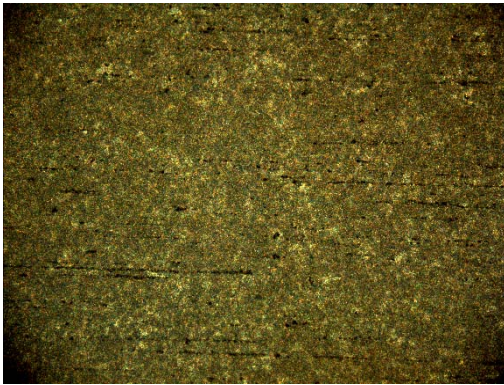
12



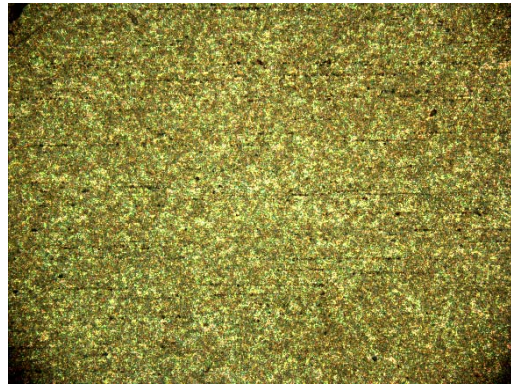
13



14



15

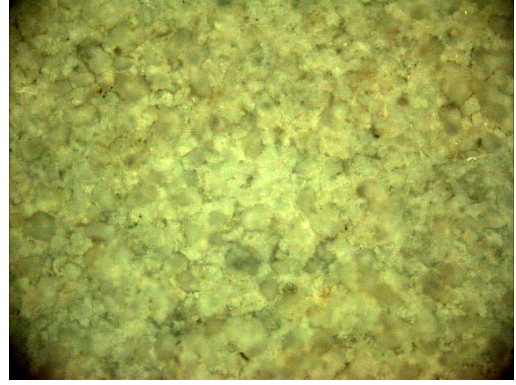


16

Figure B.2: Surface micrographs of the samples treated under current controlled, (100x)



V100



V150

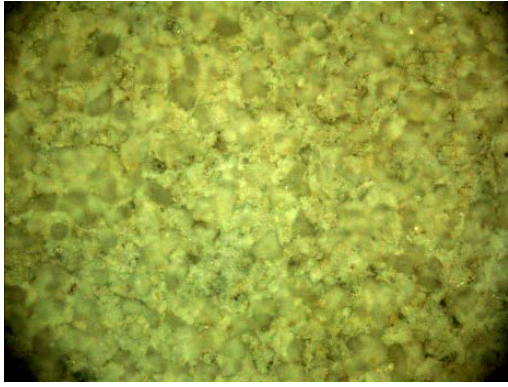


I410

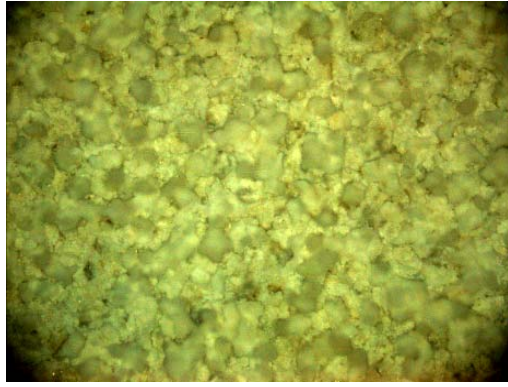


I420

Figure B.3: Surface micrographs of the samples oxidized to achieve maximum coating thickness, (100x)



325



425



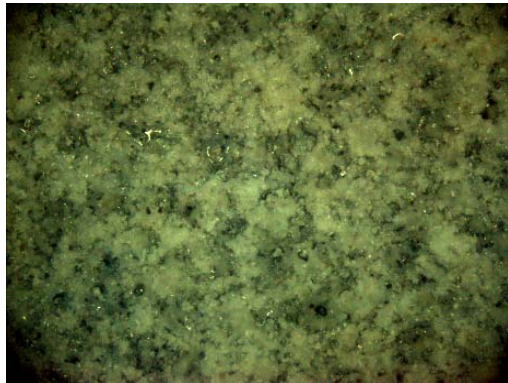
525



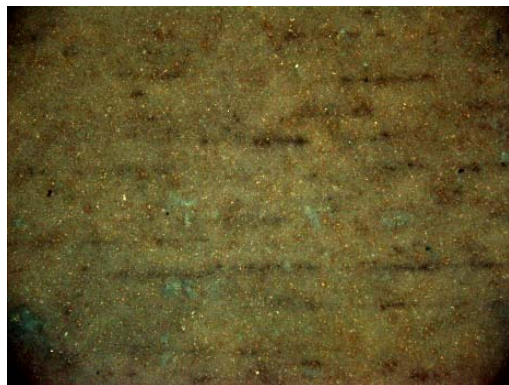
524



523



522



521

Figure B.4: Surface images of MAO treated samples treated with different pulse durations, 100x

Appendix C

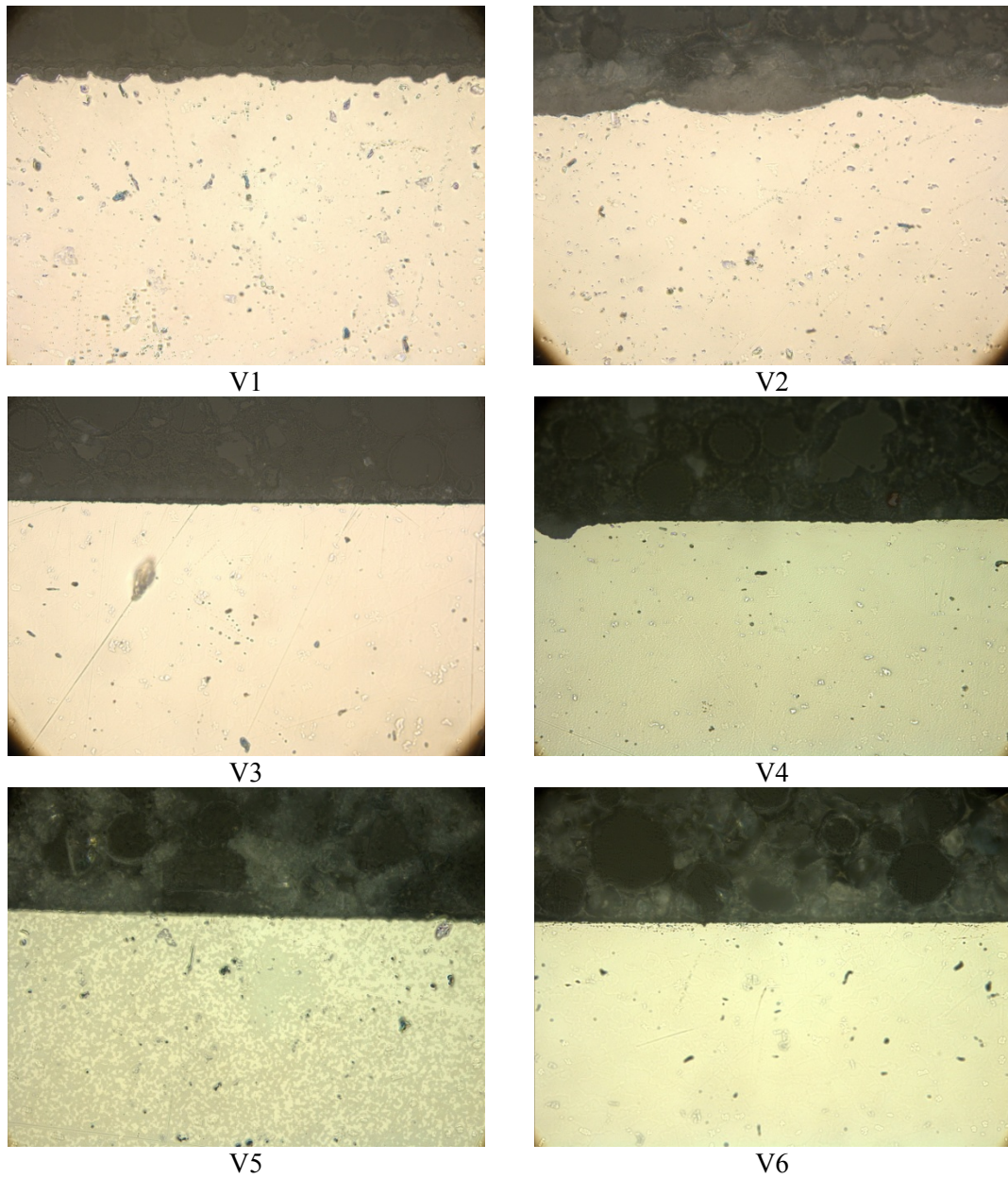
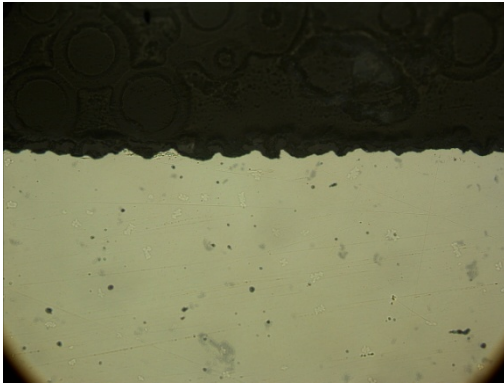
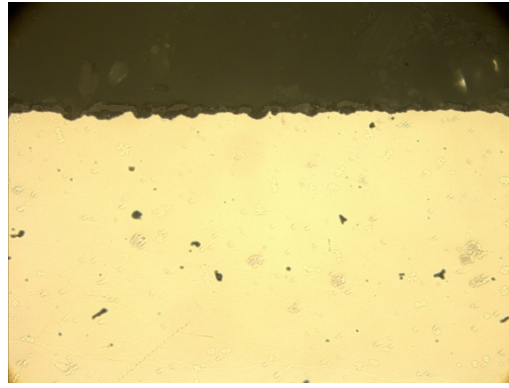


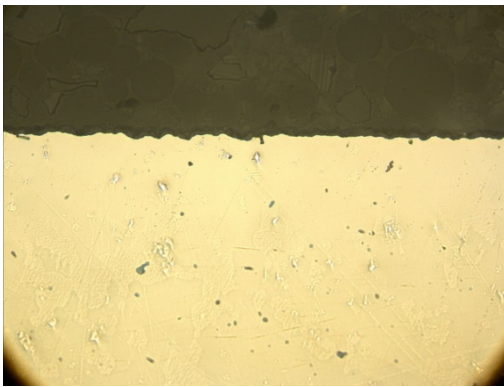
Figure C.1: Cross-sectional optical microscope images of the samples treated with voltage controlled method, 500x



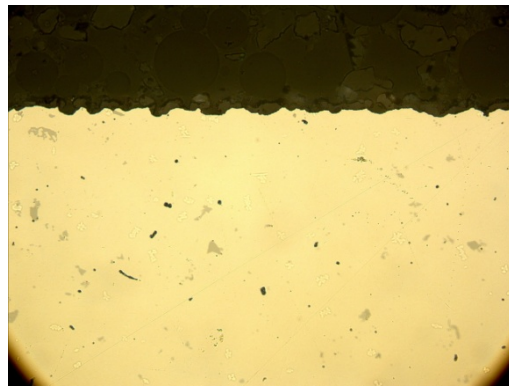
I1



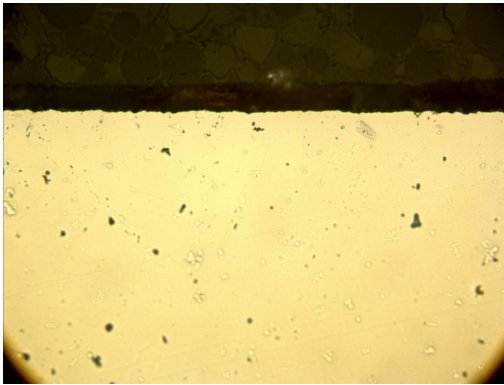
I2



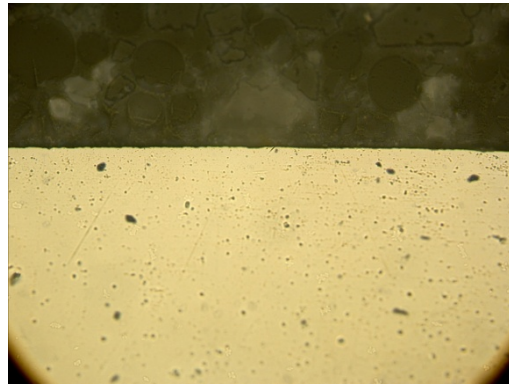
I3



I4



I5



I6

Figure C.2: Cross-sectional optical microscope images of the samples treated with current controlled method, 500x

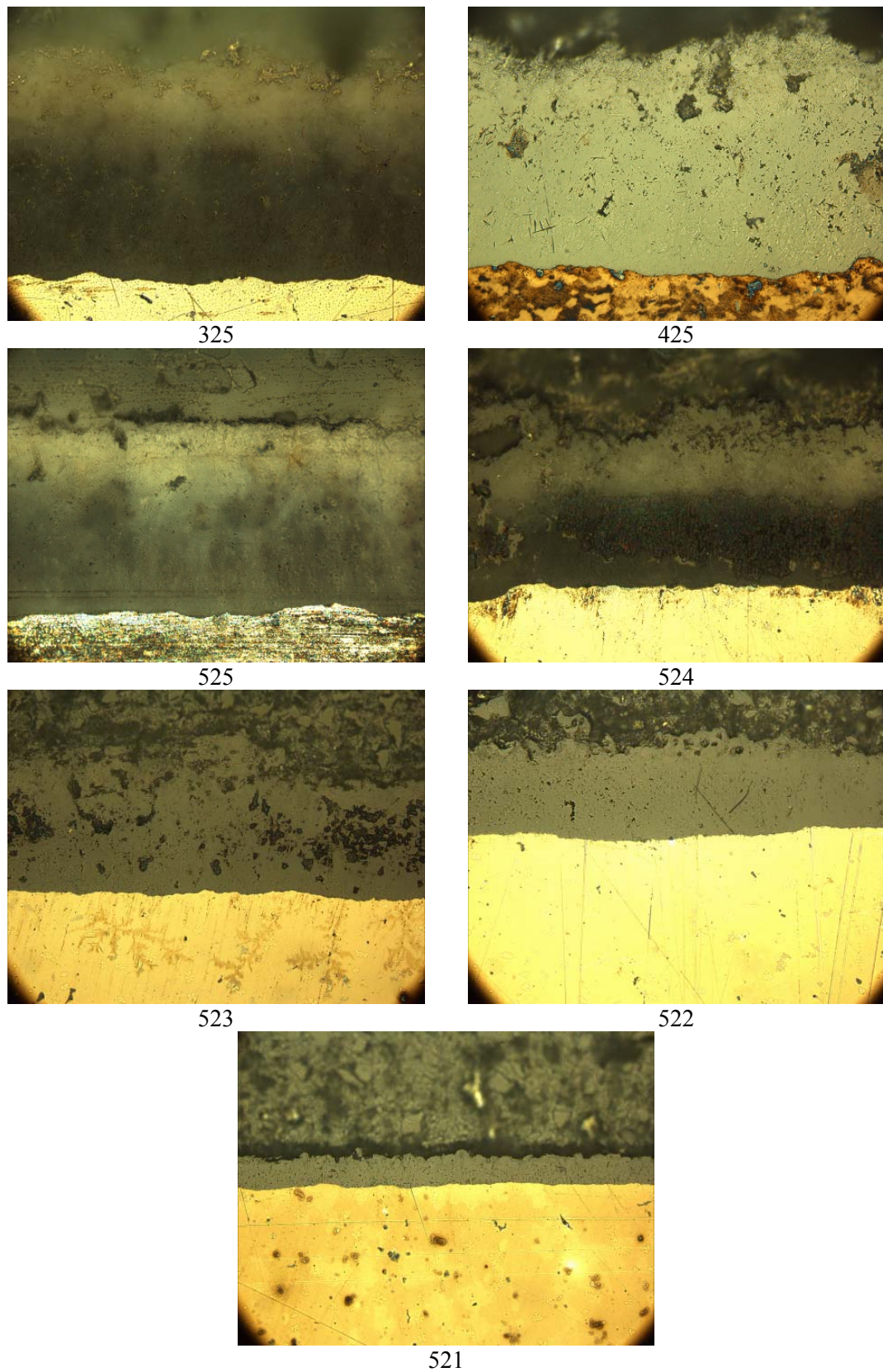
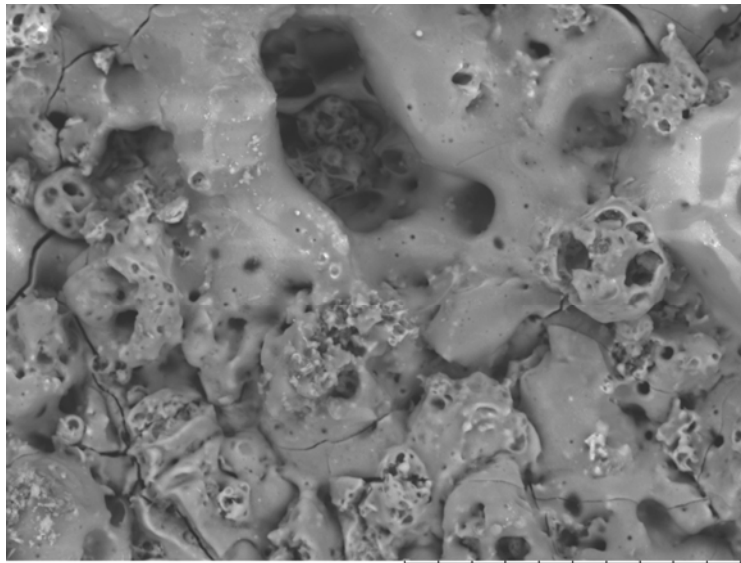
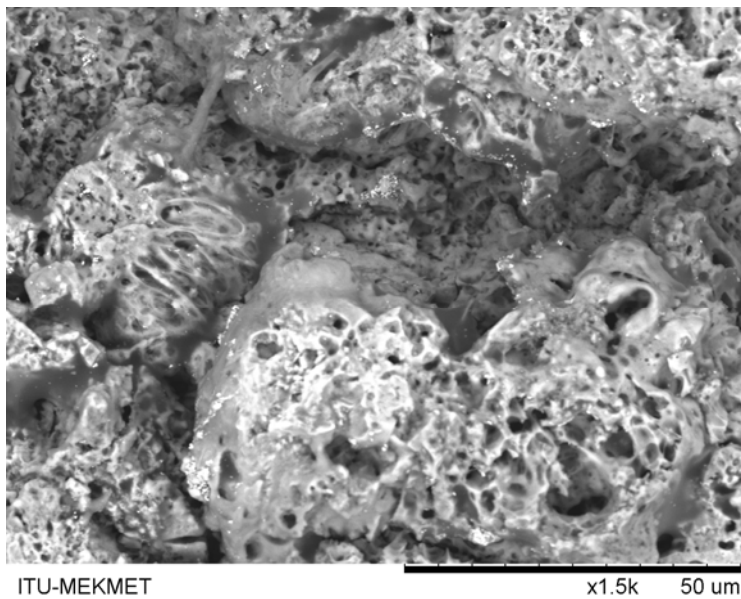


Figure C.3: Cross-sectional optical microscope images of samples treated with different pulse durations; 500x

Appendix D



500/100 V



500/150 V

Figure D.1: SEM surface images of samples treated to achieve maximum coating thickness

Appendix E

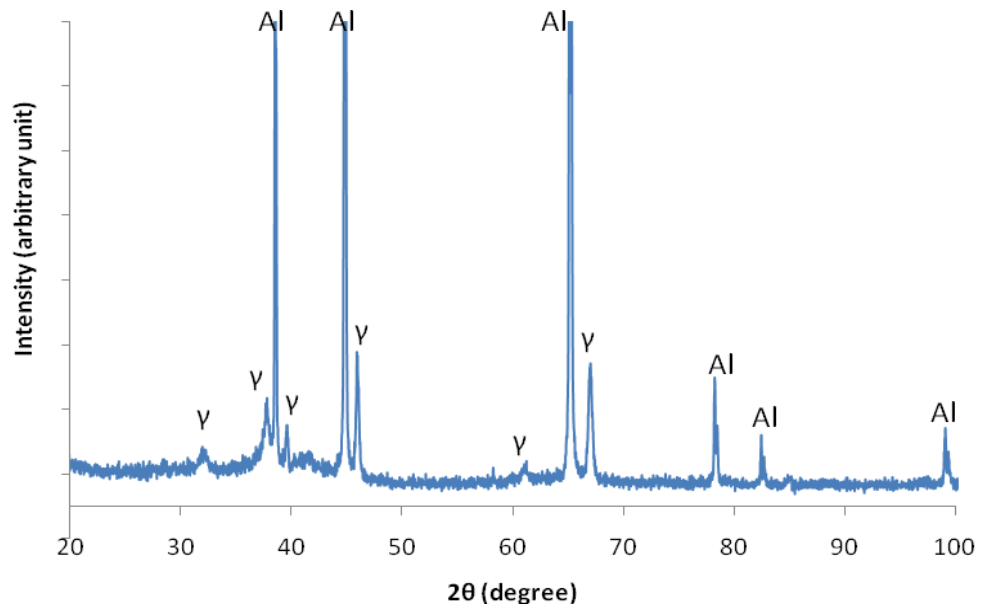


Figure E.1: XRD pattern of the sample treated with the condition of V1

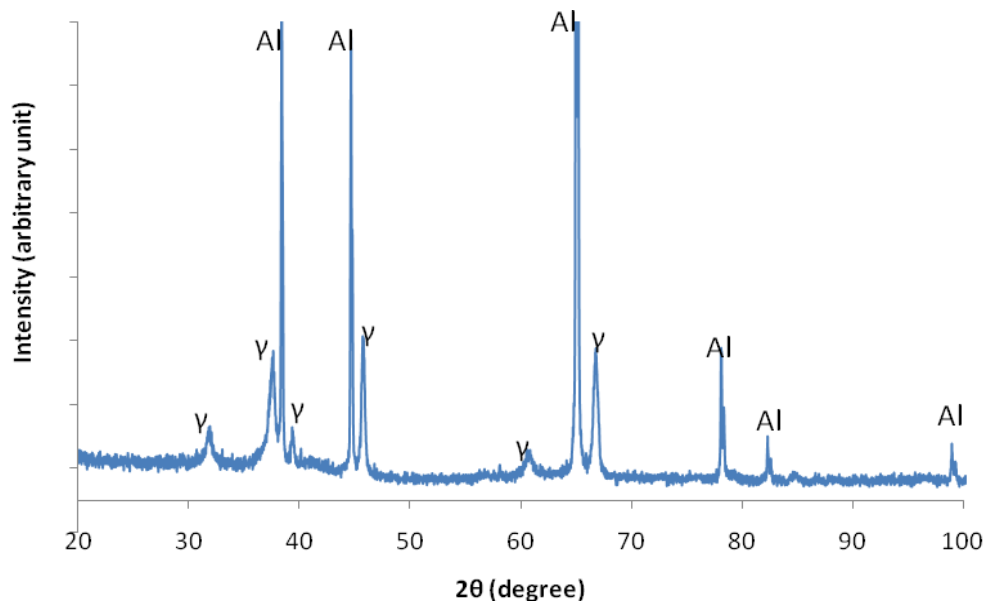


Figure E.2: XRD pattern of the sample treated with the condition of V2

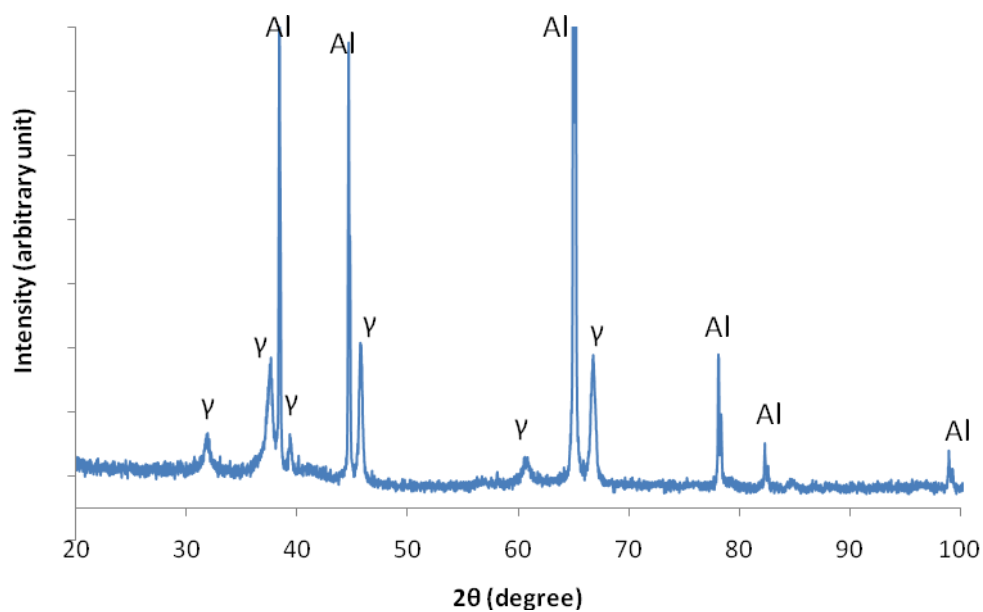


Figure E.3: XRD pattern of the sample treated with the condition of V3

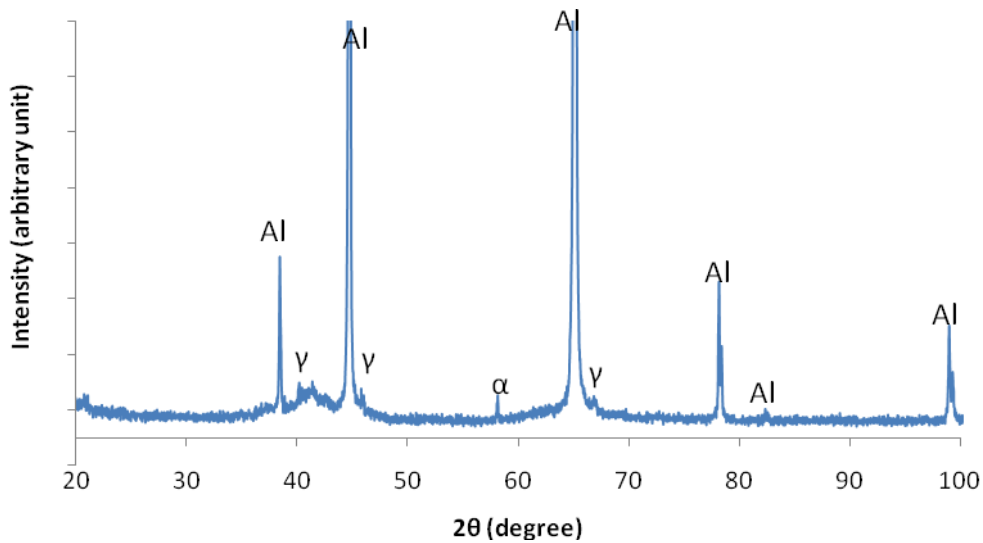


Figure E.4: XRD pattern of the sample treated with the condition of V4

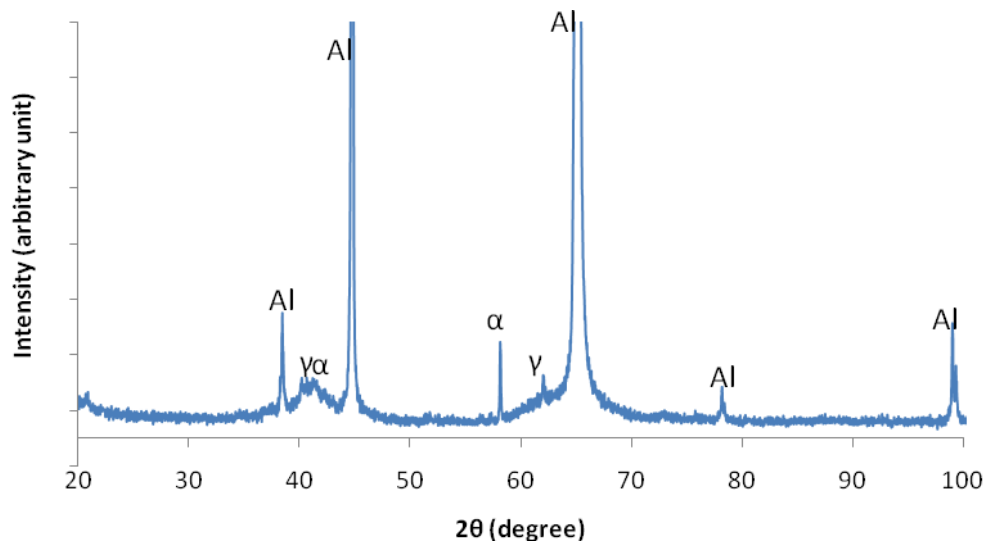


Figure E.5: XRD pattern of the sample treated with the condition of V5

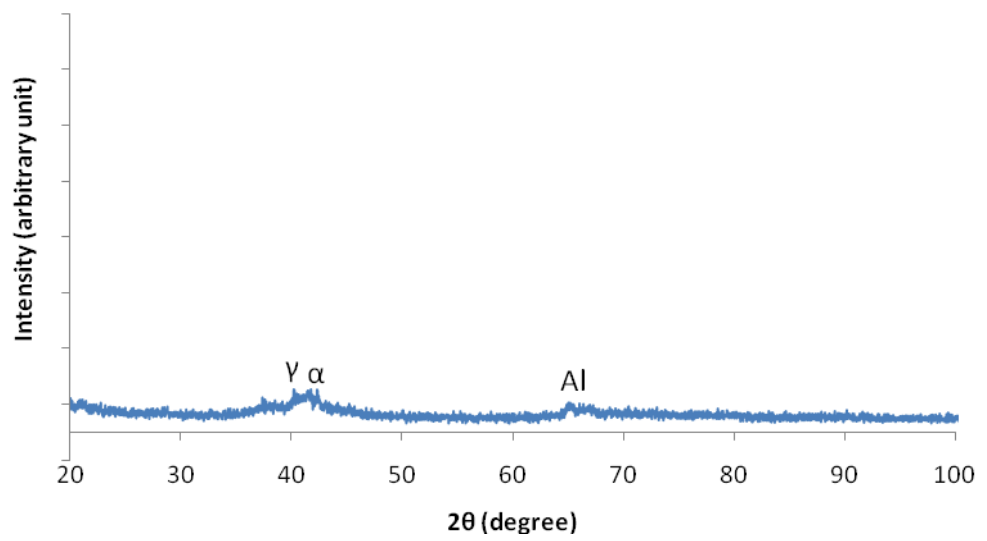


Figure E.6: XRD pattern of the sample treated with the condition of V6

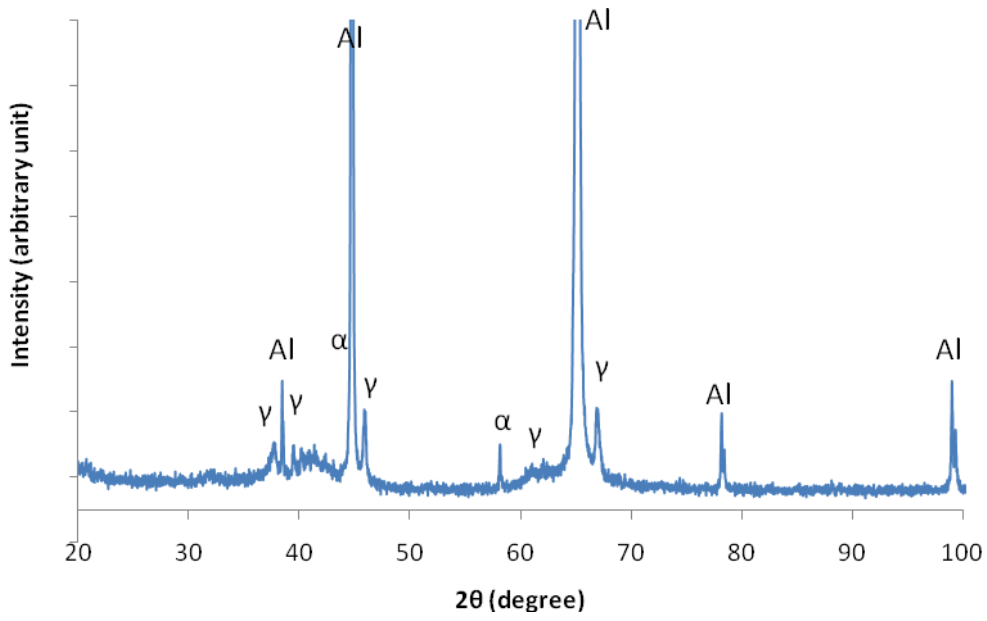


Figure E.7: XRD pattern of the sample treated with the condition of I1

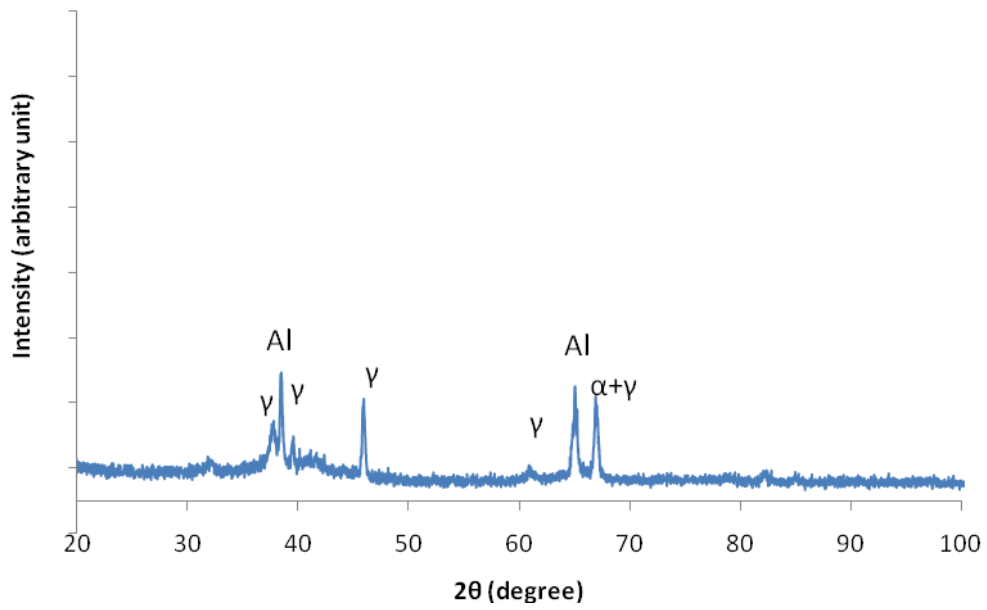


Figure E.8: XRD pattern of the sample treated with the condition of I2

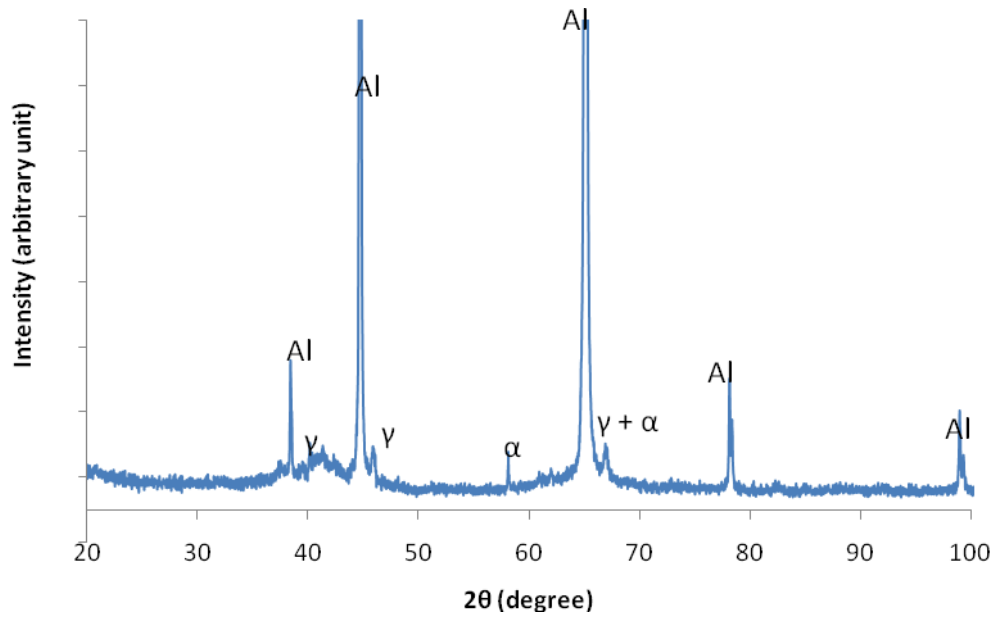


Figure E.9: XRD pattern of the sample treated with the condition of I3

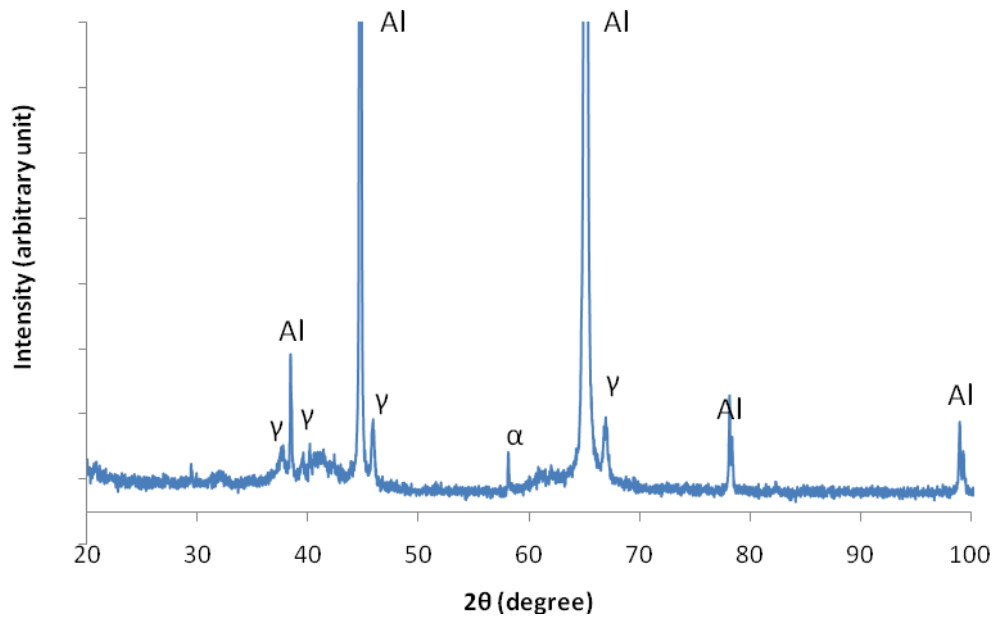


Figure E.10: XRD pattern of the sample treated with the condition of I4

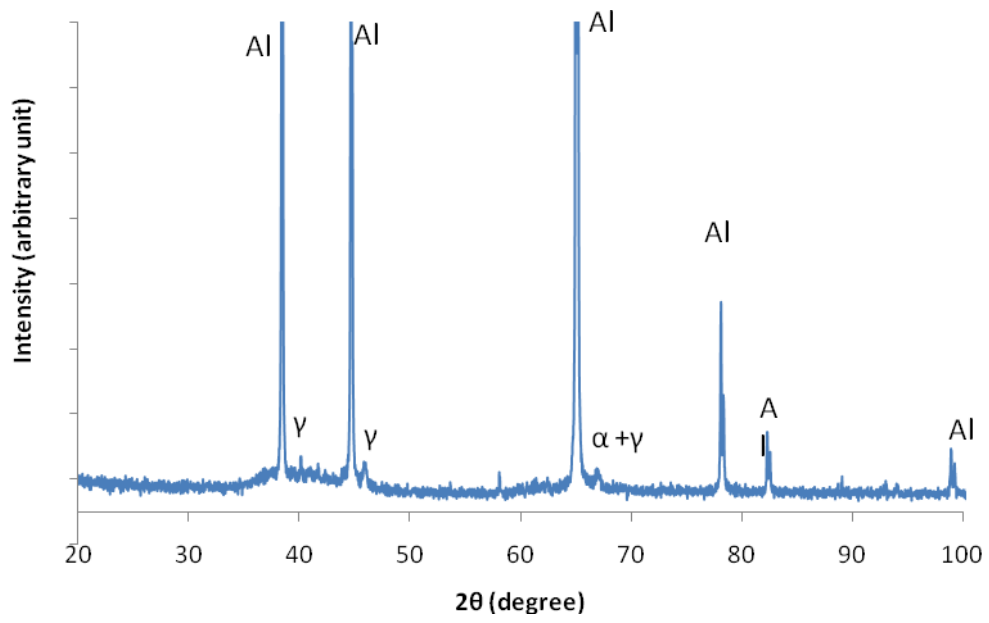


Figure E.11: XRD pattern of the sample treated with the condition of I5

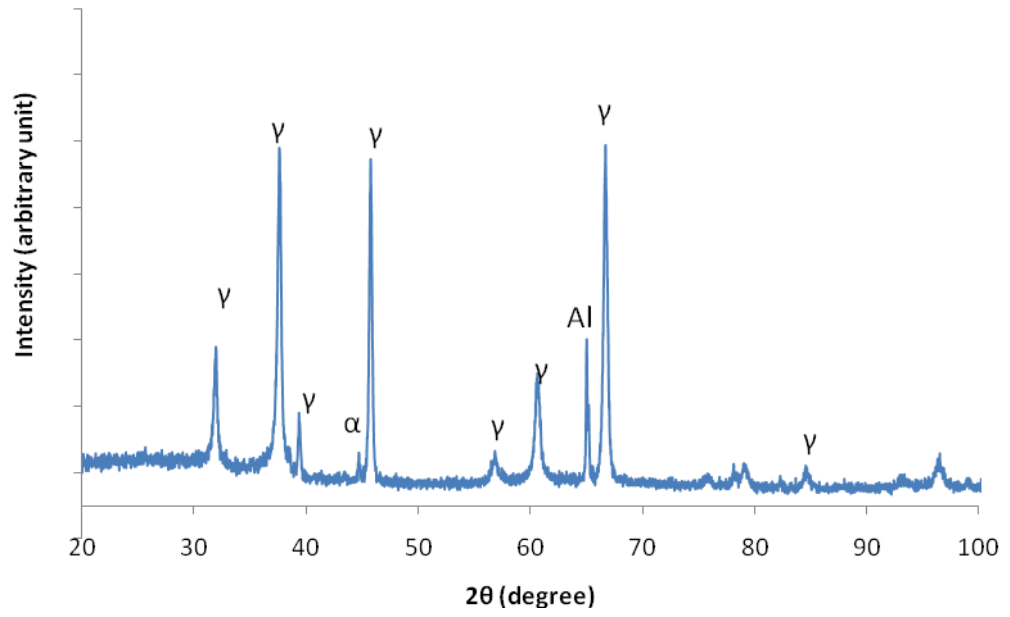


Figure E.13: XRD pattern of the sample treated with the condition of V100

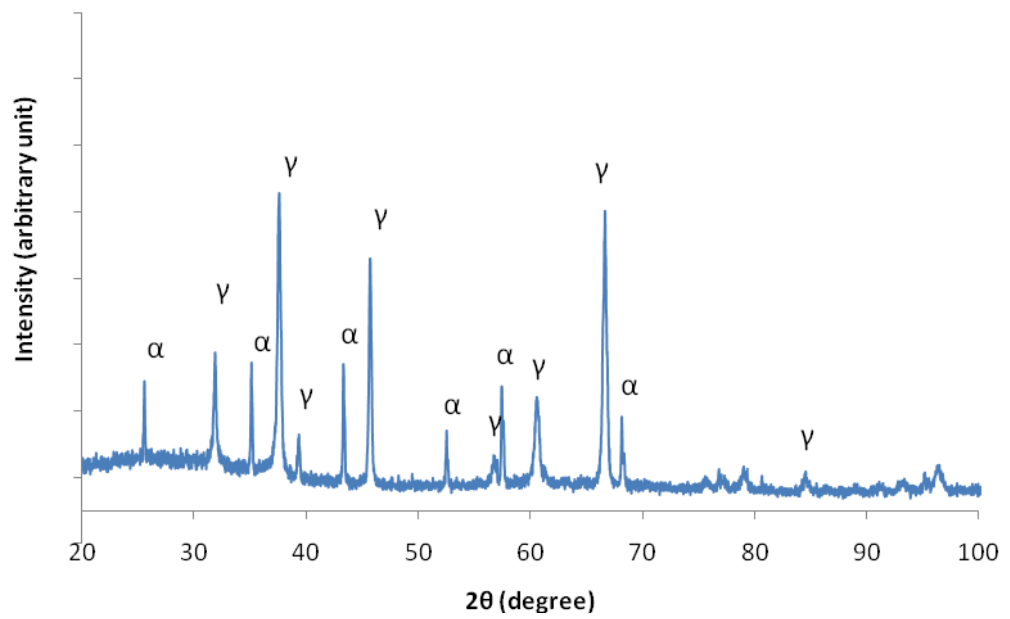


Figure E.14: XRD pattern of the sample treated with the condition of V150

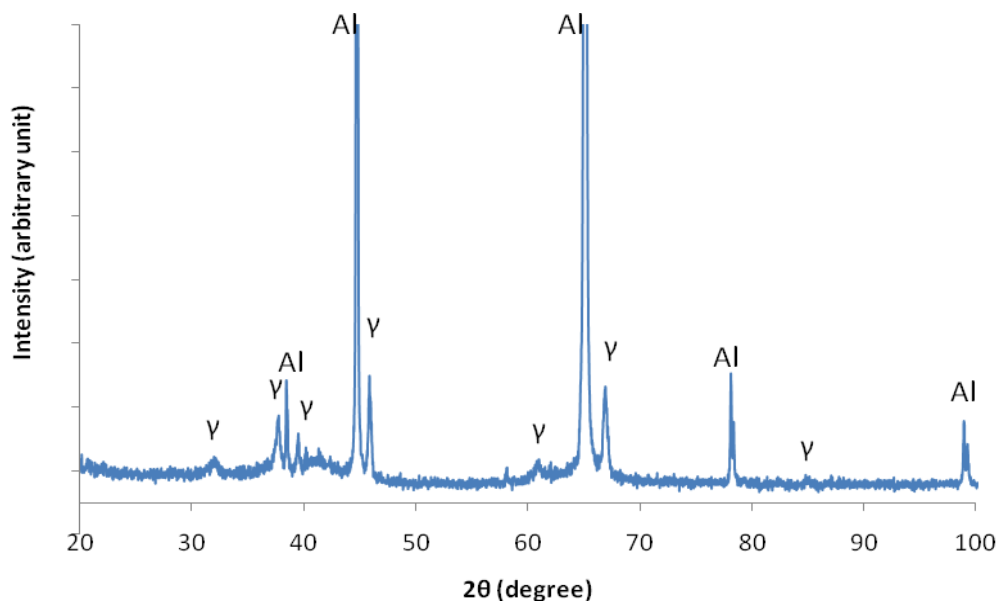


Figure E.15: XRD pattern of the sample treated with the condition of I410

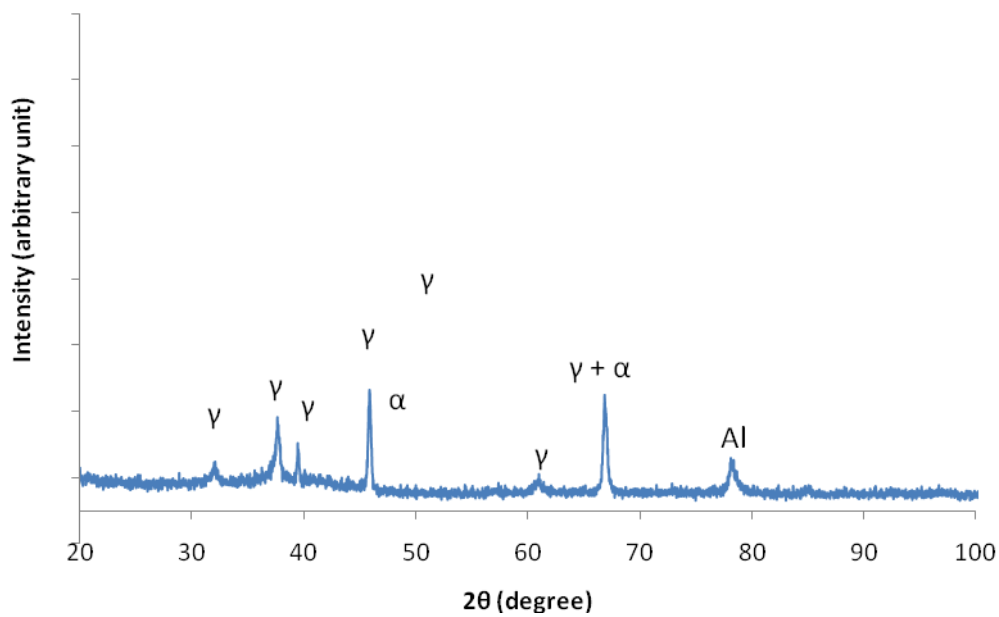


Figure E.16: XRD pattern of the sample treated with the condition of I420

Appendix F

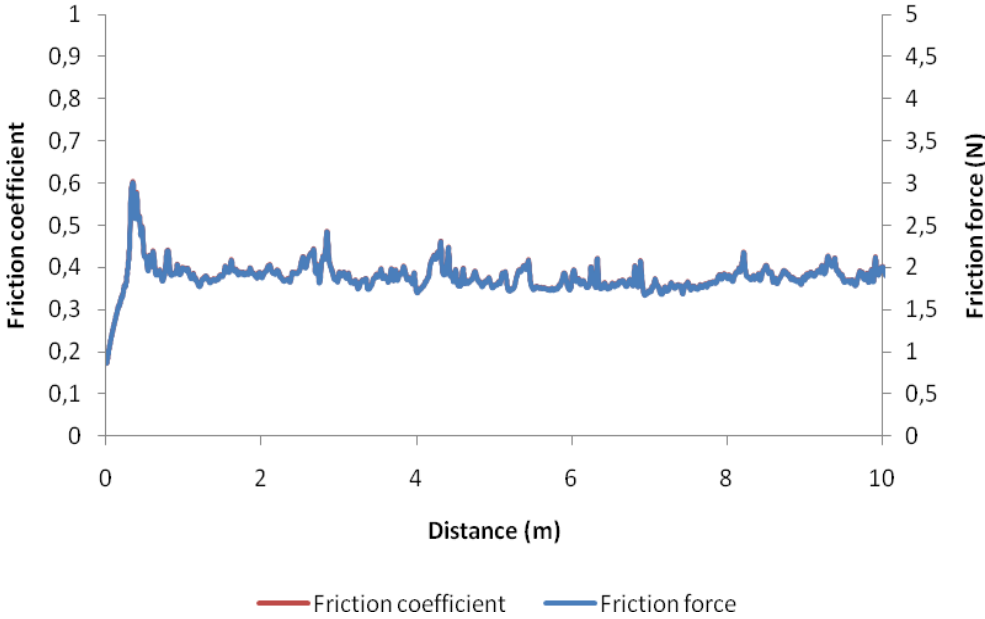


Figure F.1: Wear pattern of the sample treated with the condition of V1

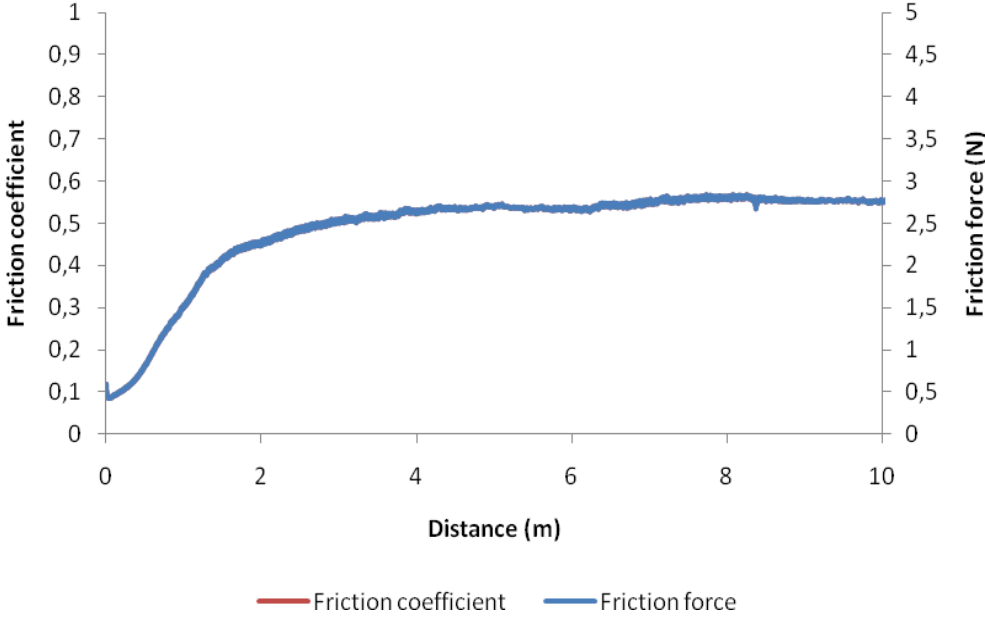


Figure F.2: Wear pattern of the sample treated with the condition of V2

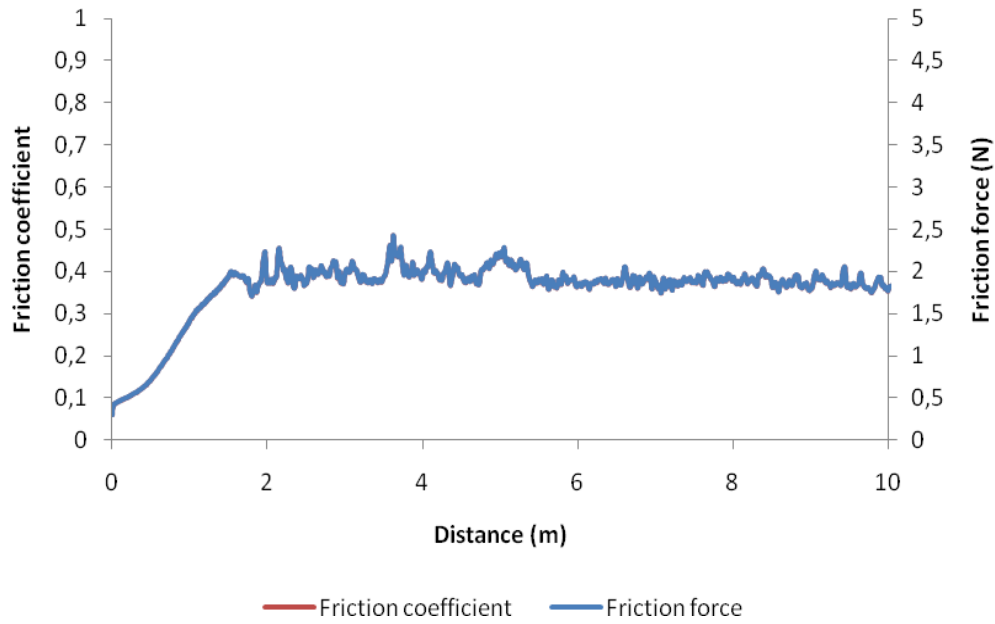


Figure F.3: Wear pattern of the sample treated with the condition of V3

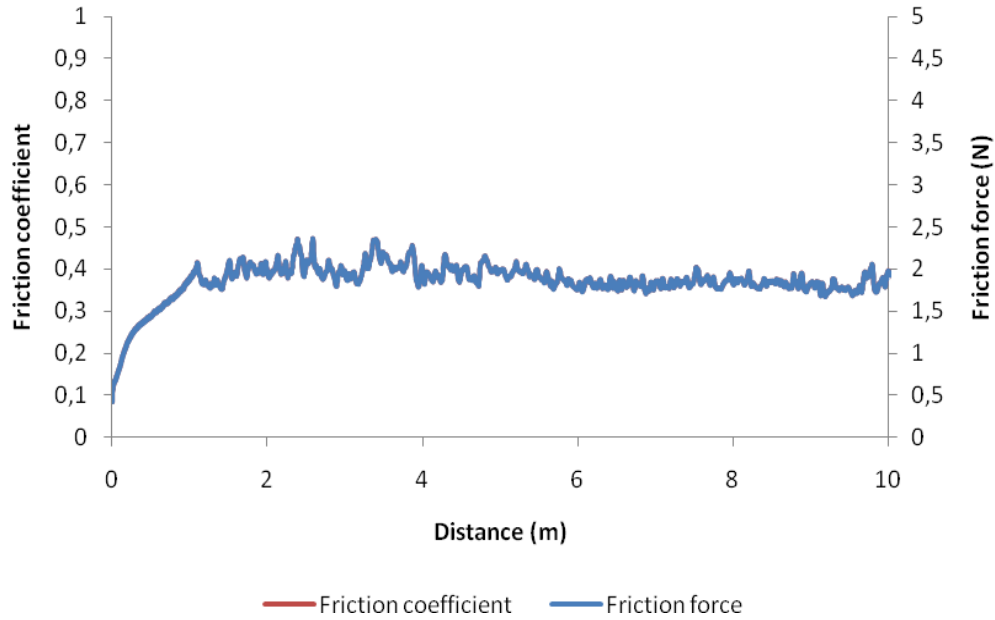


Figure F.4: Wear pattern of the sample treated with the condition of V4

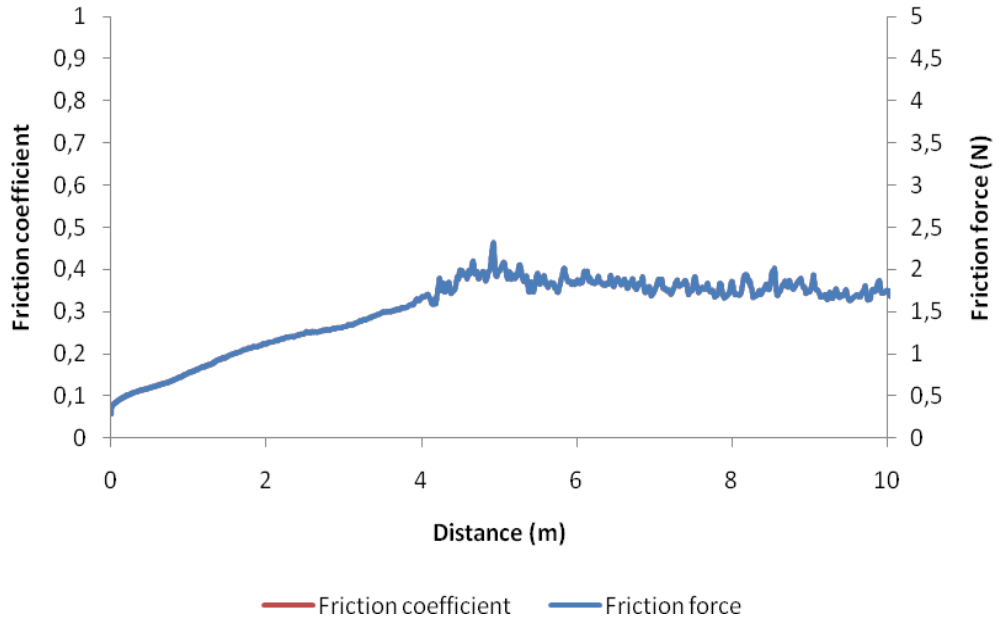


Figure F.5: Wear pattern of the sample treated with the condition of V5

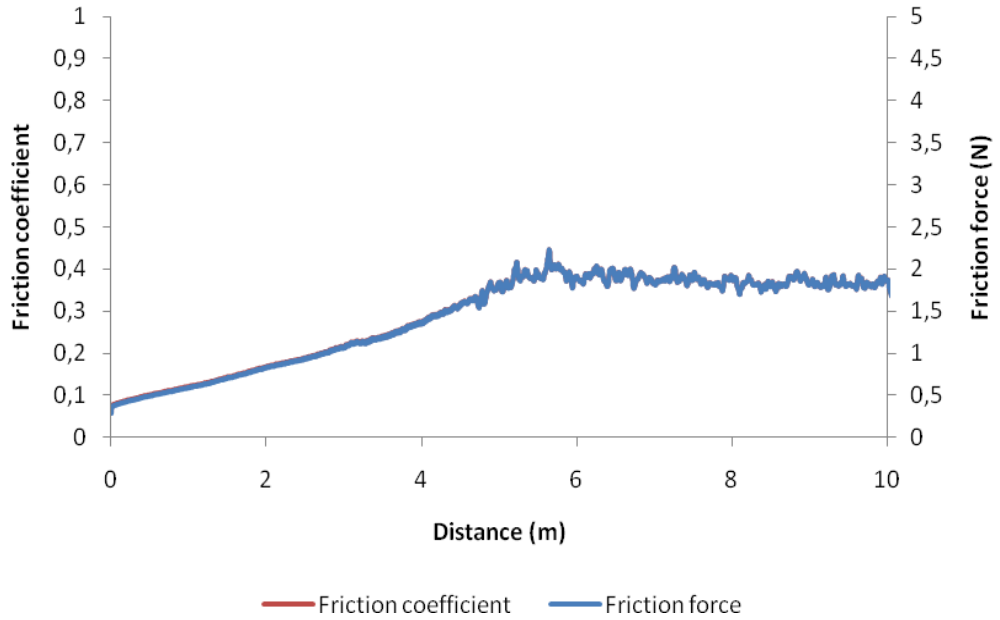


Figure F.6: Wear pattern of the sample treated with the condition of V6

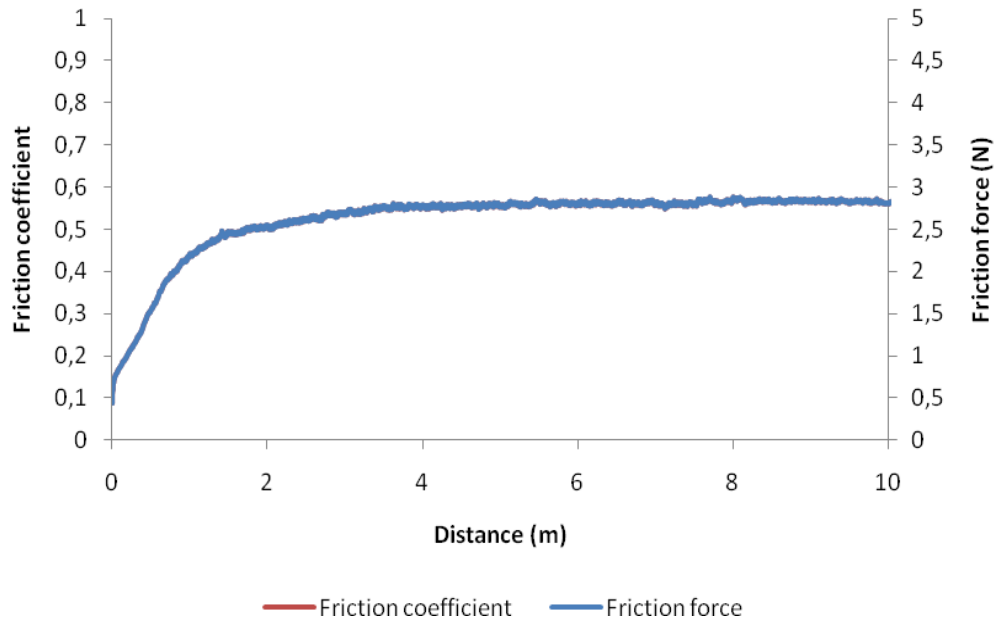


Figure F.7: Wear pattern of the sample treated with the condition of I1

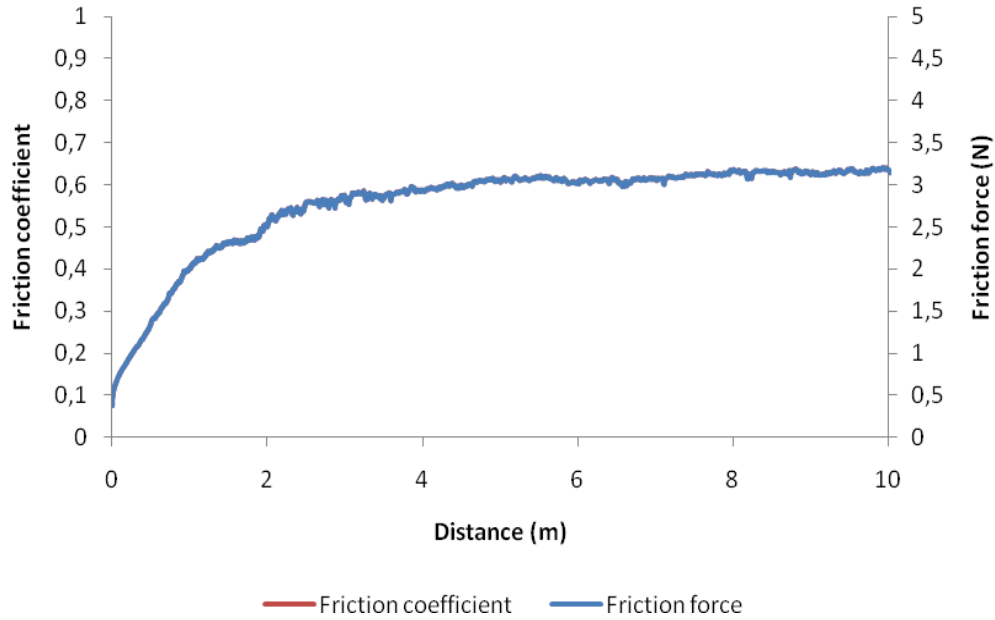


Figure F.8: Wear pattern of the sample treated with the condition of I2

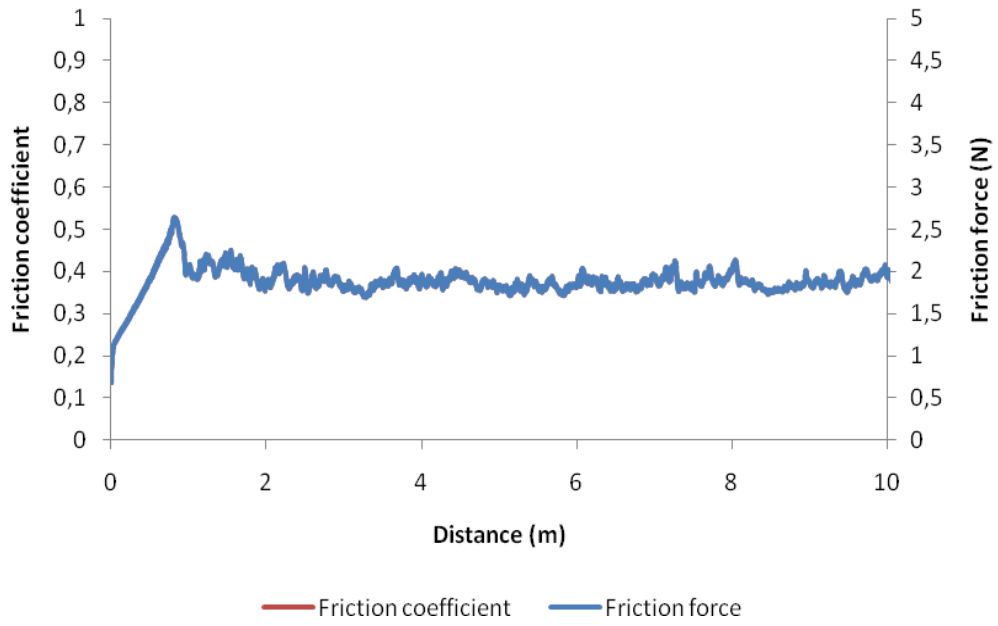


Figure F.9: Wear pattern of the sample treated with the condition of I3

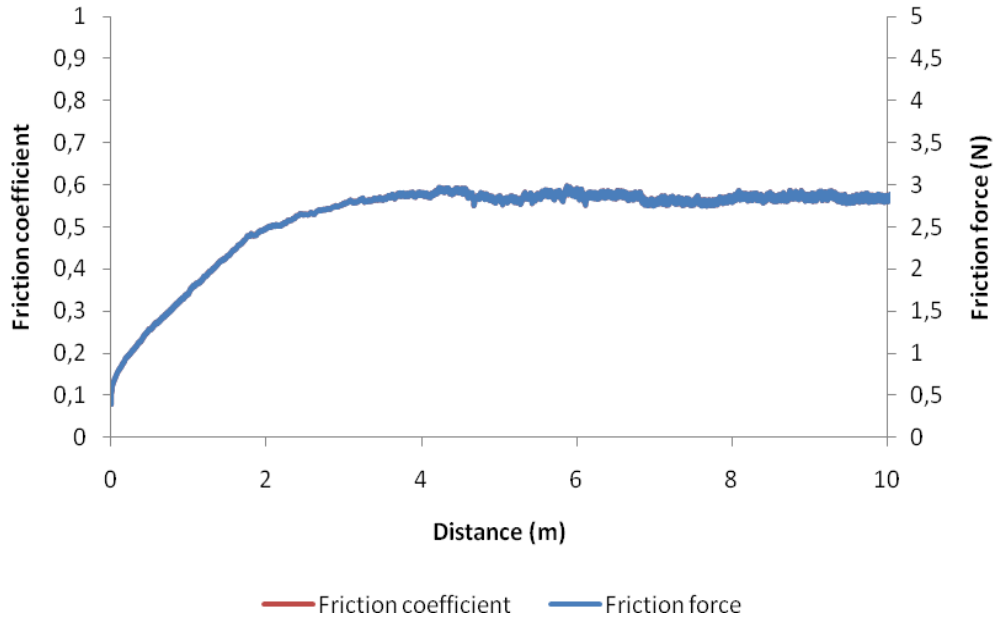


Figure F.10: Wear pattern of the sample treated with the condition of I4

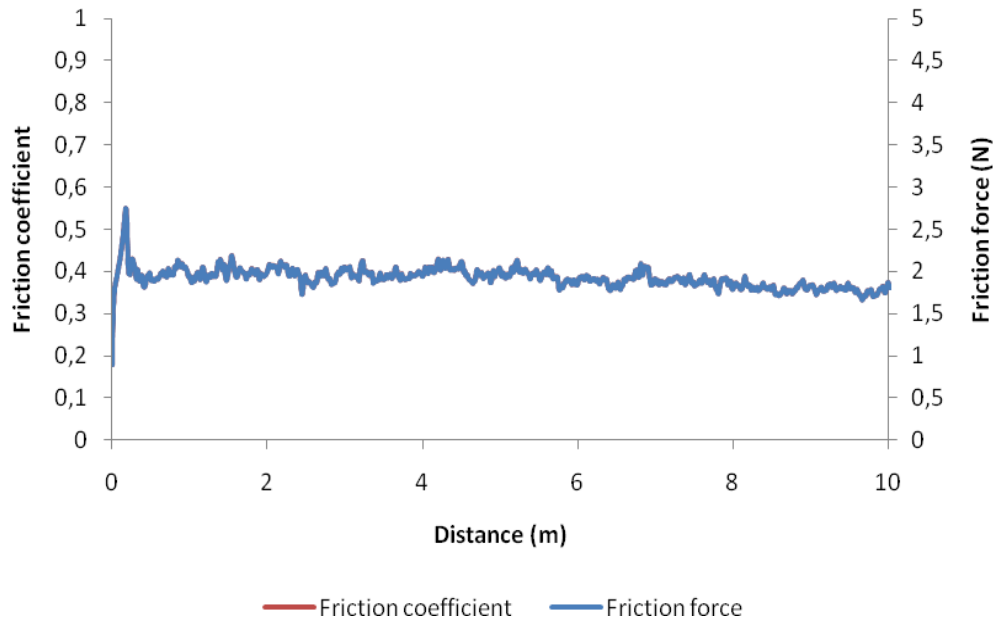


Figure F.11: Wear pattern of the sample treated with the condition of I5

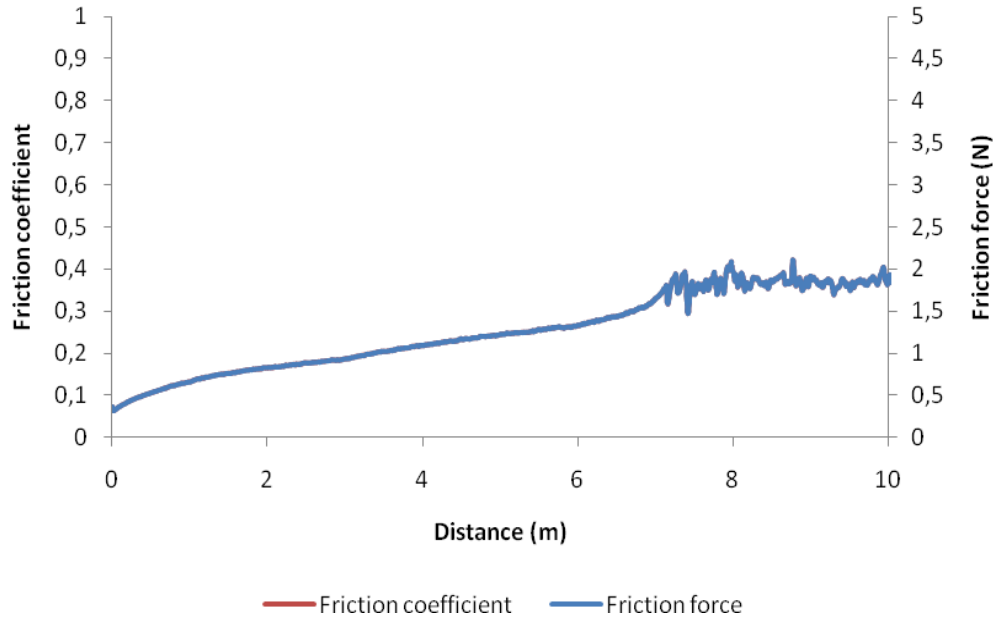


Figure F.12: Wear pattern of the sample treated with the condition of I6

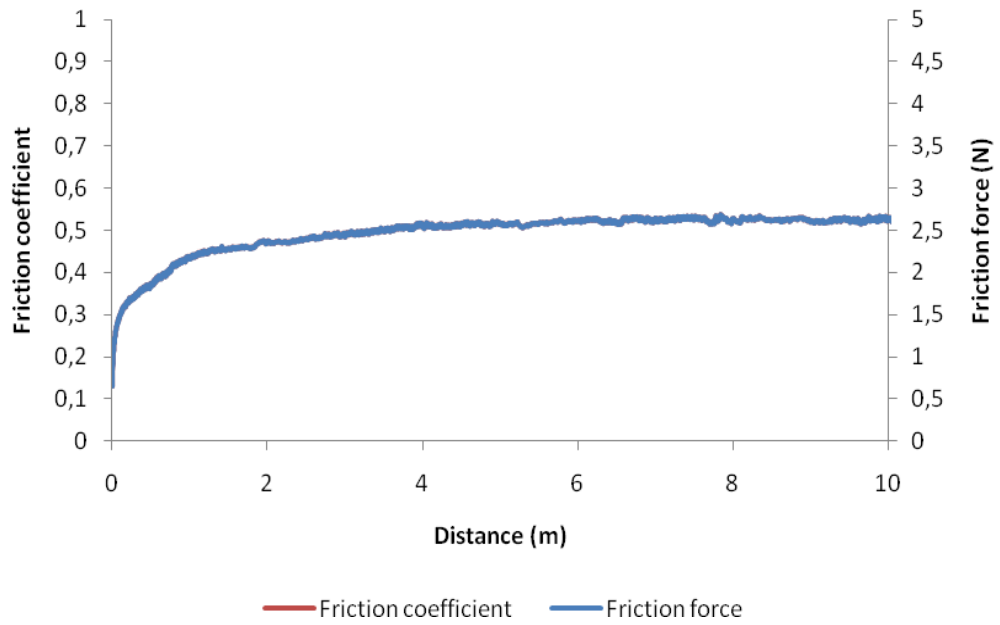


Figure F.13: Wear pattern of the sample treated with the condition of V100

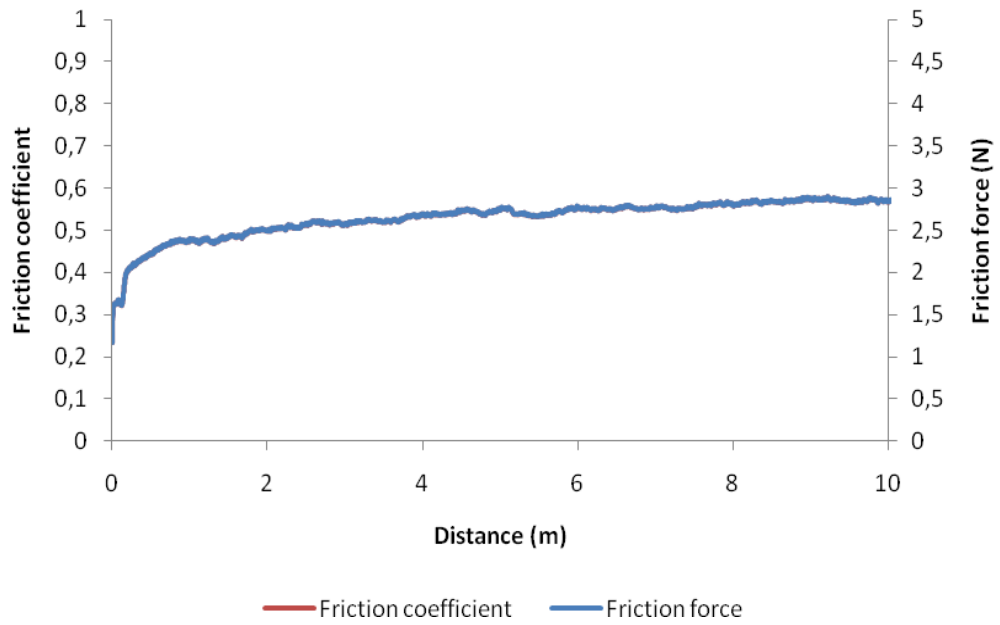


Figure F.14: Wear pattern of the sample treated with the condition of V150

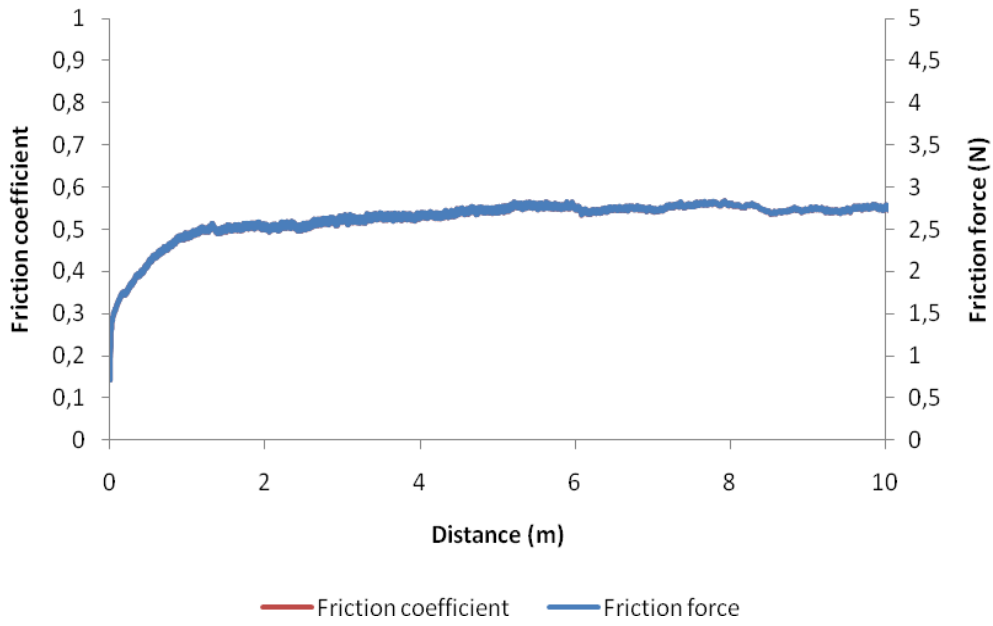


Figure F.15: Wear pattern of the sample treated with the condition of I410

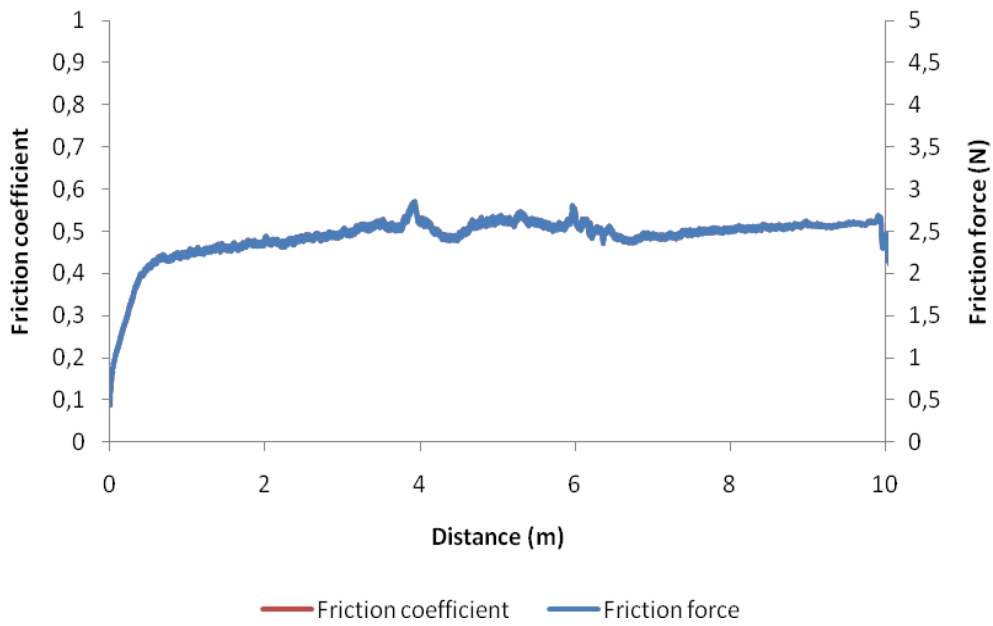


Figure F.16: Wear pattern of the sample treated with the condition of I420

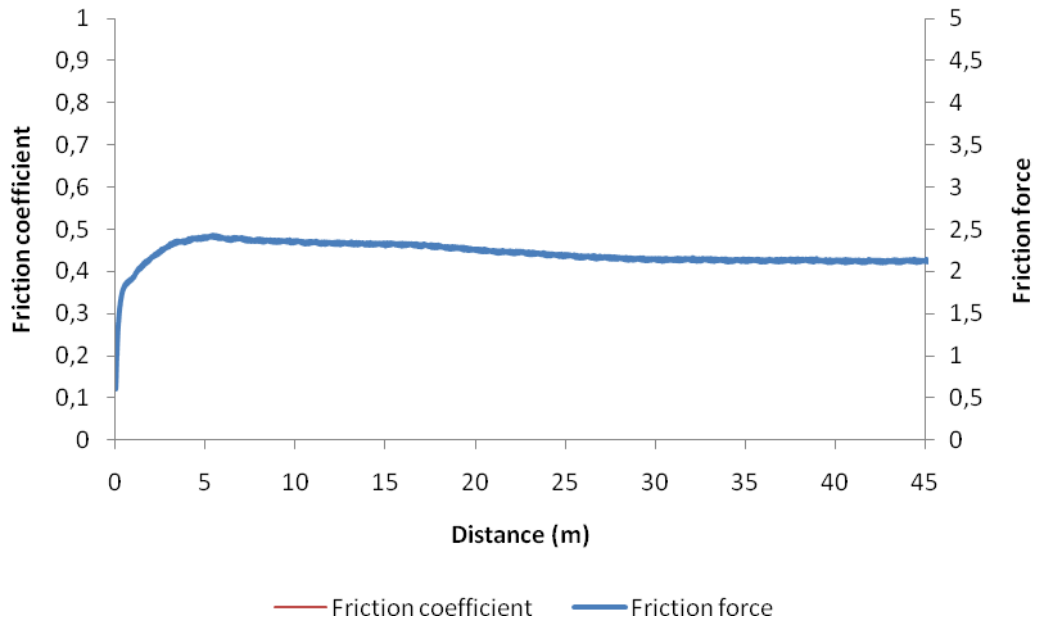


Figure F.17: Wear pattern of the sample treated with the condition of 521

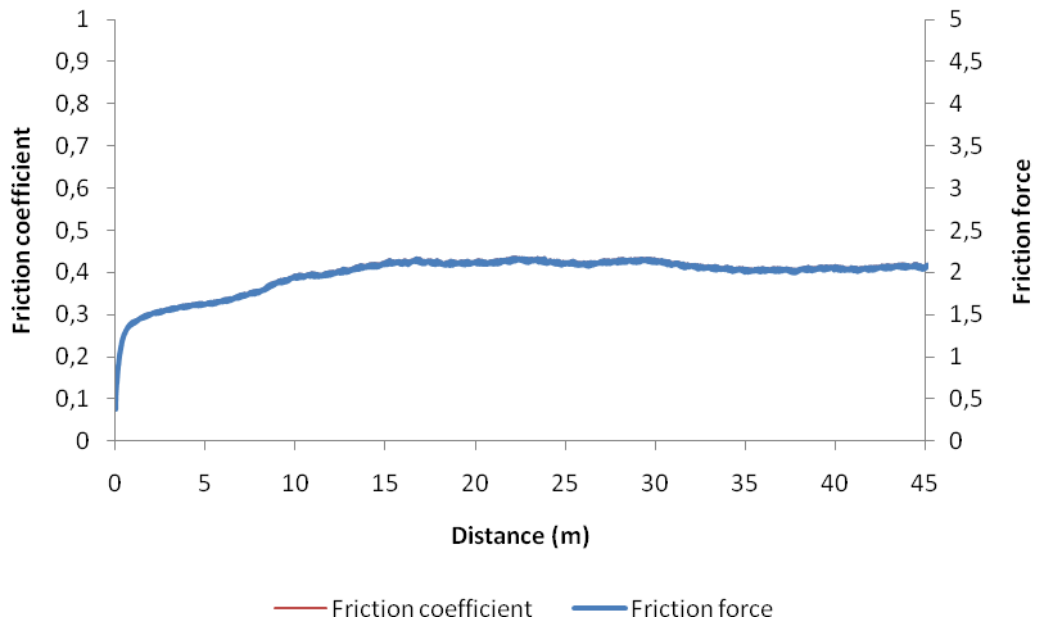


Figure F.18: Wear pattern of the sample treated with the condition of 522

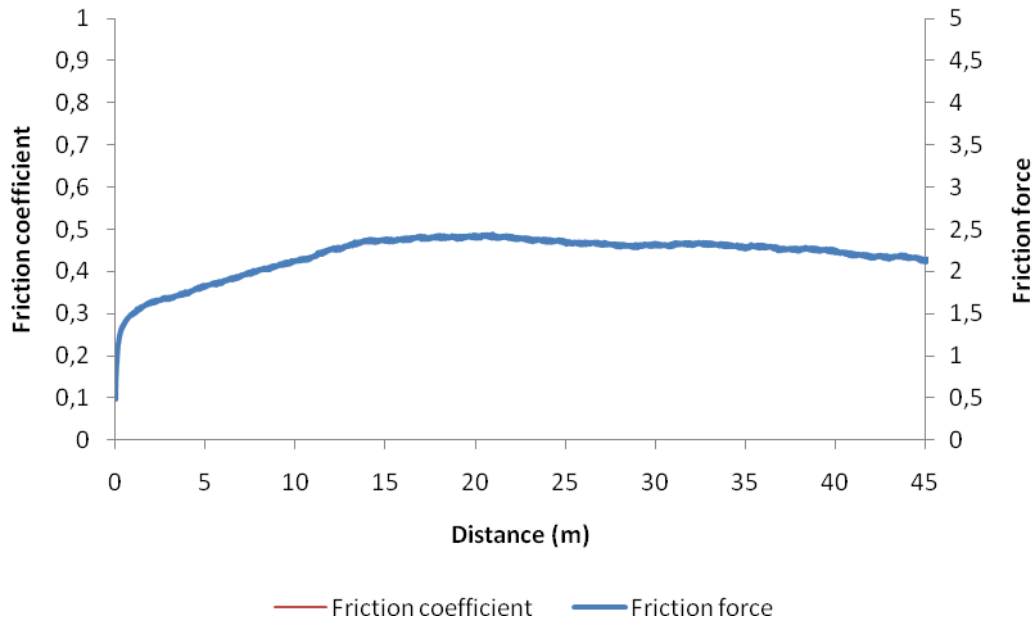


Figure F.19: Wear pattern of the sample treated with the condition of 523

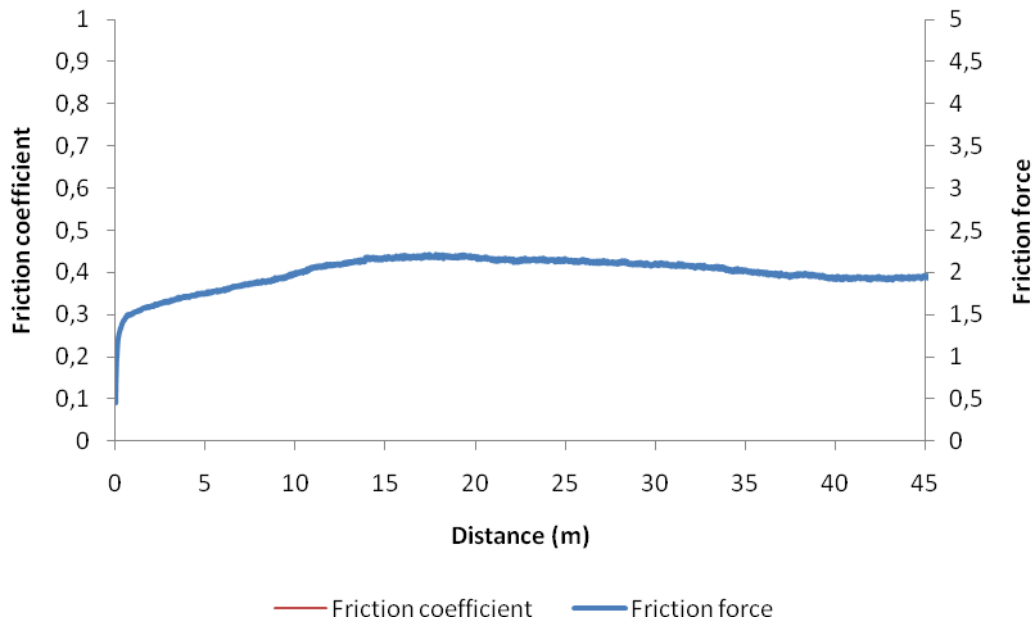


Figure F.20: Wear pattern of the sample treated with the condition of 524 μs

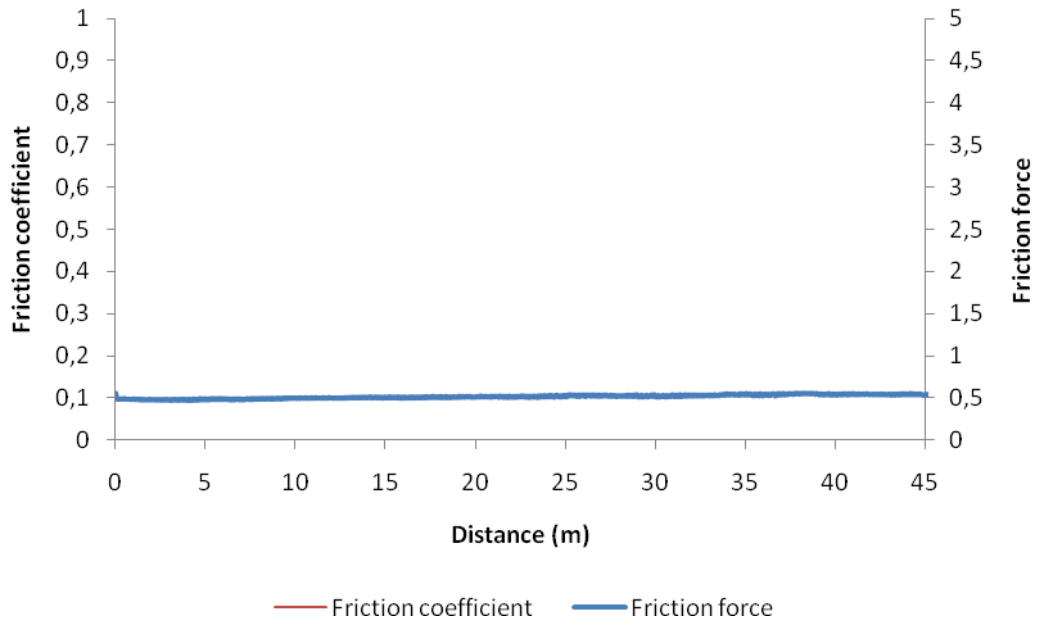


Figure F.21: Wear pattern of the sample treated with the condition of 525

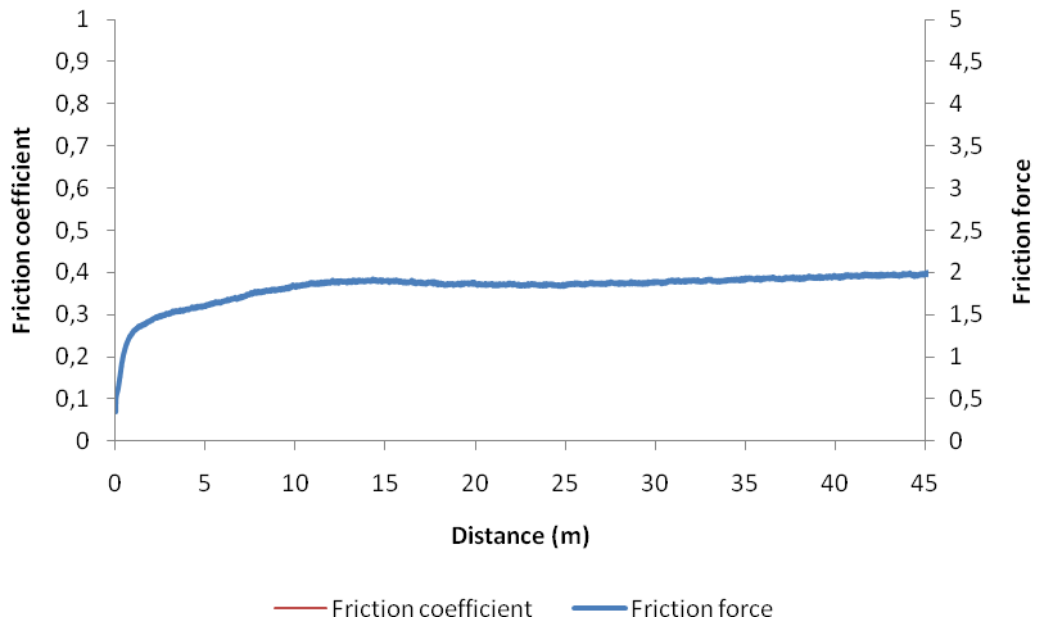


Figure F.22: Wear pattern of the sample treated with the condition of 425

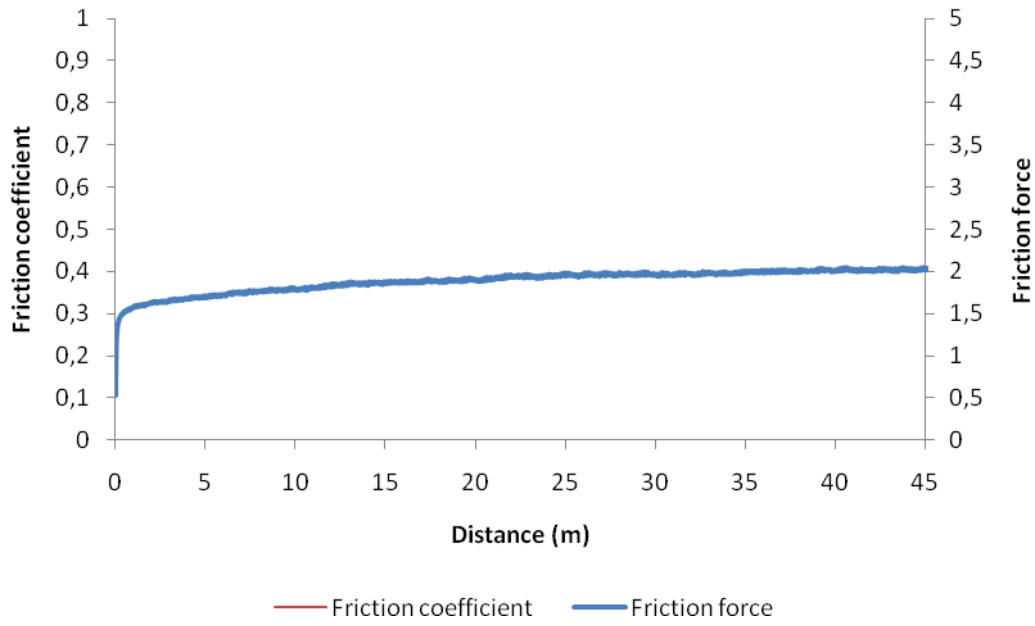


Figure F.23: Wear pattern of the sample treated with the condition of 325

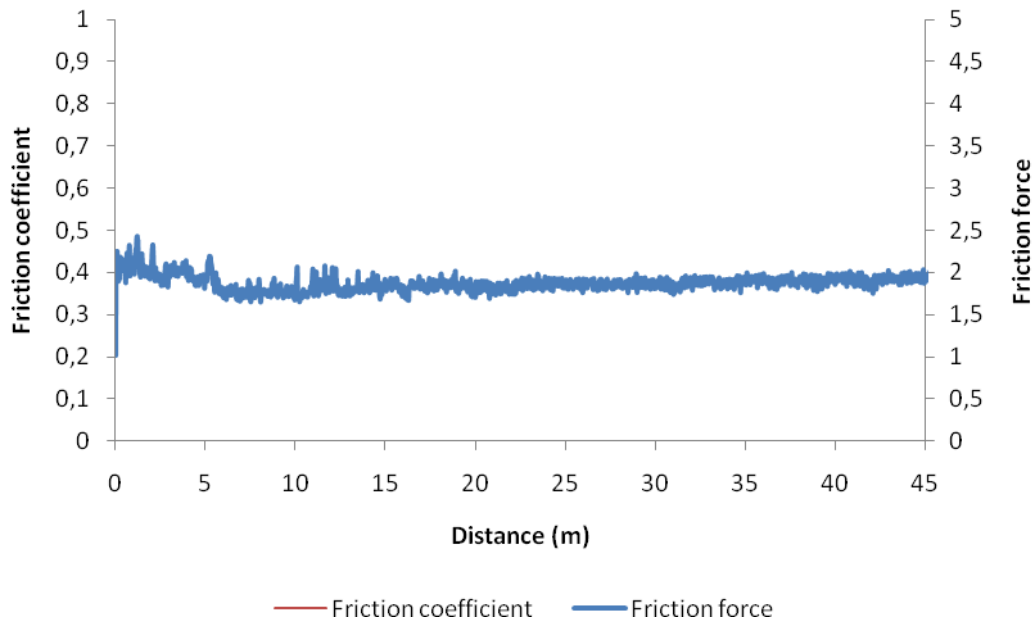
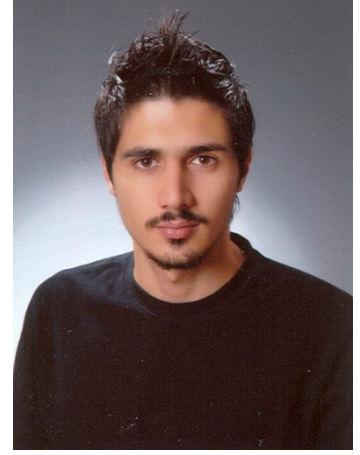


Figure F.24: Wear pattern of 7075 bare aluminum sample

CIRRICULUM VITAE

Samet Serkan BOZKUŞ was born on January, 04 1983 and grown up in Istanbul. He had completed his high school education in Bahçeşehir Atatürk High School. He graduated from Eskişehir Osmangazi University,



Metallurgy and Materials Engineering department in 2007. He started his graduate education in Materials Engineering Department of Istanbul Technical University in 2008. Since then, he has been studying for his M.Sc. degree at Institute of Science and Technology in ITU.

Publications:

1. **Bozkuş, S. S., Baydoğan, M., Çimenoğlu, H., Kayalı, E. S.**, The Effect of Frequency of Microarc Oxidation on Surface Properties of 7075 Aluminum Alloys, In TMS Conference, The Minerals, Metals & Society, Seattle, Washington, USA, February 14-18 2010
2. **Bozkuş, S. S., Fabrizi, Mehtedi, M. E., Spigarelli, S., Gabrielli, F., Salvia, A. D., Haidopoulos M.**, Formability Studies On Thin Films Coated Sheets, In ECNF, European Conference on Nano Films, Liege, Belgium, March 22-25 2010